CHERN-SIMONS THEORY OF MAGNETIZATION PLATEAUS ON THE KAGOME LATTICE

BY

PONNURAJ KRISHNAKUMAR

DISSERTATION

Submitted in partial fulfillment of the requirements
for the degree of Doctor of Philosophy in Physics
in the Graduate College of the
University of Illinois at Urbana-Champaign, 2016

Urbana, Illinois

Doctoral Committee:

Professor Mike Stone, Chair
Professor Eduardo Fradkin, Director of Research
Assistant Professor Gregory MacDougall
Professor John Stack

Abstract

Frustrated spin systems on Kagome lattices have long been considered to be a promising candidate for realizing exotic spin liquid phases. Recently, there has been a lot of renewed interest in these systems with the discovery of experimental materials such as Volborthite and Herbertsmithite that have Kagome like structures. In this thesis I will focus on studying frustrated spin systems on the Kagome lattice using a spin-1/2 antiferromagnetic XXZ Heisenberg model in the presence of an external magnetic field as well as other perturbations. Such a system is expected to give rise to magnetization platueaus which can exhibit topological characteristics in certain regimes.

We will first develop a flux-attachment transformation that maps the Heisenberg spins (hard-core bosons) onto a problem of fermions coupled to a Chern-Simons gauge field. This mapping relies on being able to define a consistent Chern-Simons term on the lattice. Using this newly developed mapping we analyse the phases/magnetization plateaus that arise at the mean-field level and also consider the effects of adding fluctuations to various mean-field states. Along the way, we show how to discretize an abelian Chern-Simons gauge theory on generic 2D planar lattices that satisfy certain conditions. We find that as long as there exists a one-to-one correspondence between the vertices and plaquettes defined on the graph, one can write down a discretized lattice version of the abelian Chern-Simons gauge theory.

Using the newly developed flux attachment transformation, we show the existence of chiral spin liquid states for various magnetization plateaus for certain range of parameters in the XXZ Heisenberg model in the presence of an external magnetic field. Specifically, in the regime of XY anisotropy the ground states at the 1/3 and 2/3 plateau are equivalent to a bosonic fractional quantum Hall Laughlin state with filling fraction 1/2 and that the 5/9 plateau is equivalent to the first bosonic Jain daughter state at filling fraction 2/3.

Next, we also consider the effects of several perturbations: a) a chirality term, b) a Dzyaloshinskii-Moriya term, and c) a ring-exchange type term on the bowties of the kagome lattice, and inquire if they can also support chiral spin liquids as ground states. We find that the chirality term leads to a chiral spin liquid even in the absence of an uniform magnetic field, with an effective spin Hall conductance of $\sigma^s_{xy} = \frac{1}{2}$ in the regime

of XY anisotropy. The Dzyaloshinkii-Moriya term also leads a similar chiral spin liquid but only when this term is not too strong. An external magnetic field when combined with some of the above perturbations also has the possibility of giving rise to additional plateaus which also behave like chiral spin liquids in the XY regime. Under the influence of a ring-exchange term we find that provided its coupling constant is large enough, it may trigger a phase transition into a chiral spin liquid by the spontaneous breaking of time-reversal invariance.

Finally, we also present some numerical results based on some exact diagonalization studies. Here, we specifically focus on the 2/3-magnetization plateau which we previously argued should be a chiral spin liquid with a spin hall conductance of $\sigma^s_{xy} = \frac{1}{2}$. Such a topological state has a non-trivial ground state degeneracy and it excitations are described by semionic quasiparticles. In the numerical analysis, we analyse the ground state degeneracy structure on various Kagome clusters of different sizes. We compute modular matrices from the resultant minimally entangled states as well as the Chern numbers of various eigenstates all of which provide strong evidence that the 2/3-magnetization plateau very closely resembles a chiral spin liquid state with the expected characteristics.

Acknowledgments

I would first like to thank my advisor Eduardo Fradkin for giving me the chance to work with him and for his guidance during my time in graduate school. I learned a lot under his supervision and enjoyed the opportunity to work on some really interesting physics problems.

Next I would like to acknowledge my main collaborators, Kai Sun and Hitesh Changlani, who have made major contributions to the projects that I have worked on. Kai Sun has been actively involved in this work since the very beginning and his contributions were crucial to the development and understanding of the discretized version of the Abelian Chern-Simons gauge theories. Hitesh has been actively involved in the numerical part of my project and has helped me immensely in developing all the numerical tools that were needed to analyze the chiral spin liquid states.

I also want to thank the Physics department, ICMT and its various professors that have helped and guided me through the course of my graduate school. I especially want to thank Professor Lance Cooper for all his advice, support and all the career related events he has organized over the years as the head of graduate programs.

Next I would like to thank my parents who have always been supportive and understanding of all my goals and dreams in life. I really appreciate their unwavering belief in me and for being a constant source of encouragement throughout my time in graduate school. I would also like to thank my sister, Kirthi, who has been a major source of inspiration and motivation during some of the difficult times in life. I also want to thank my girlfriend, Archana, for enduring and putting up with me through all the ups and downs of graduate school. She has always been there to listen to any of my problems and provide advice and moral support.

Finally, I would like to thank all my friends and fellow graduate students (Mayukh, Greg, Rodrigo, Oat, Anshul, Bode, Anuj and many others not mentioned here) for all their help, support and fun times over the years.

Table of Contents

List of Tables

List of Figures

Chapter 1

Introduction

1.1 Geometric frustration and spin liquids

Frustration generally refers to spin systems where all the spin interactions cannot simultaneously be satisfied. Geometric frustration arises when the particular structure of the lattice leads to the above mentioned scenario. A classic example of geometrical frustration is the triangular lattice with nearest neighbour antiferromagnetic (AFM) Ising spins. Ising spins can point in only two directions, either up or down. The spins in such a system prefer to align in opposite directions but on a triangle this cannot be done simultaneously for all three spins as shown in Fig 1.1(a). As a result the third "frustrated" spin is free to point either up or down giving rise to a ground state degeneracy. This degeneracy grows with the size of the system leading to a large ground state manifold. If the same problem where considered on a square lattice with nearest neighbour interactions there would not be any frustration and the ground state would consist of up spins on one sub-lattice and down spins on the other sub-lattice. The example presented in Fig 1.1(a) for Ising spins can also be generalized to Heisenberg spins (spins that can point in any direction) which will be focus of this thesis.

Under certain circumstances, it is believed that these spins can fluctuate all the way down to $T = 0$. This would give rise to a highly correlated state of spins without any particular ordering. Such a disordered state is called a spin liquid. Spin liquids do not break any symmetries and cannot as such be described by any local order parameters. It is also believed that spin liquid states can exhibit fractional excitations and may also have some topological characteristics.

Another lattice that also gives rise to geometric frustration is the Kagome lattice. The Kagome lattice consists of a network of corner sharing triangles (Fig 1.1(b)) and has an even larger ground state degeneracy than the triangular lattice. This higher level of frustration makes it an ideal candidate to look for these exotic spin liquid type states. From now on, we will only discuss the case of the Kagome lattice.

Another non-trivial state that can appear in frustrated systems are magnetization plateaus. In high fields, certain spin configurations may be stabilized to give rise to new states on a frustrated lattice. These

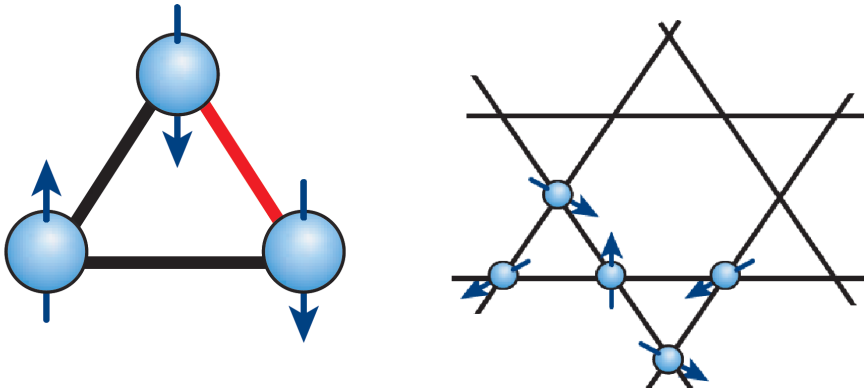

(a) Triangular Lattice (b) Kagome Lattice

Figure 1.1: Geometrically frustrated lattices [4]

states manifest themselves as plateaus in the magnetization vs. magnetic field plots. For a simple example of this situation, one can go back to the Ising spins on the triangular lattice in Fig 1.1(a) which is frustrated and highly degenerate. But in the presence of a strong magnetic field a configuration with two up and one down spin is favored in each triangle for a certain range of external magnetic fields. This would be the $\frac{1}{3}$ plateau. Most of the work presented in this thesis will focus primarily on studying magnetization plateaus and searching for spin liquids states that might exist in such plateaus.

Further, since we are concerned in the low temperature regime ($T \to 0$) where quantum effects should play an important role, we will consider primarily the case of the $S = \frac{1}{2}$ Heisenberg spins on the Kagome lattice. Bigger spins tend to behave more classically and may not be ideal for observing quantum spin liquid type states.

Next we will discuss some experimental materials that possess Kagome like structures. The discovery of such materials has lead to a lot of renewed interest in analysing and characterizing the possible spin liquid states that can arise in such materials lattices.

1.2 Experimental Materials

There are materials such as herbertsmithite and volborthite that possess Kagome like structures. M. Norman has a recent review of the many such experimental materials. [60] The more promising candidate for observing spin liquids appears to be herbertsmithite ($Zn\ Cu_3(OH)_6\ Cl_2$) which has layers of $S = 1/2\ Cu^{2+}$ moments arranged in a structurally perfect kagome lattice and has nonmagnetic Zn^{2+} ions in between the layers as shown in Fig 1.2. The low spin of the copper ions ($S = \frac{1}{2}$) also makes them ideal candidates for observing quantum spin liquids. [60]

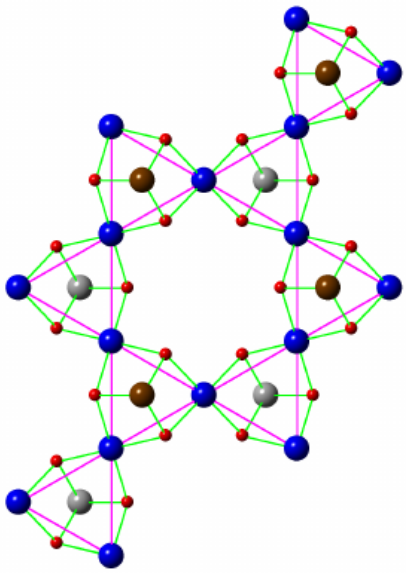

Figure 1.2: Herbersmithite: The magnetic Cu^{2+} ions are shown in blue. The red atoms are Oxygen. The Zinc ions are non-magnetic and lie in between the Cu ion planes. In the figure they are shown in gray (if they sit below the plane) and brown (if they sit above the plane). [60, 69]

T. Han et. al. performed inelastic neutron scattering experiments on single crystals of herbertsmithite at low temperatures [31]. They observed an extremely diffusive pattern for different energies down to very low temperatures of $T = 1.6$ K which is in strong contrast to observations in unfrustrated magnets. This along with the observation of a broad continuous band (characteristic of fractionalized excitations) seem to indicate that the ground state of Herbertsmithite is possibly a quantum spin liquid.

As we are more interested in the case of magnetization plateaus, we would like to consider the effects of magnetic fields on such materials. However, the value of J in Herbertsmithite is approximately 170 K. Hence, one would require fields close to 200 T to be able to observe the $\frac{1}{3}$ plateau in this material. As a result, Y. Okamoto et. al. looked for magnetization plateaus in other Kagome materials, namely in volborthite and vesignieite [61]. Both these materials also have Cu^{2+} ions carrying spin-$\frac{1}{2}$ on kagome planes but have smaller values of J (77 K for volborthite and 55 K for vesignieite) compared with that of Herbertsmithite ($J \approx 170$ K). They measured the magnetization of these materials in fields of up to 68 T at temperatures of 1.3 K and found a plateau at $\lesssim 0.4$ of the fully saturated magnetization. This value is a little larger than the theoretically expected plateau at $\frac{1}{3}$. The authors attribute this to possible magnetization steps (vertical jumps in magnetization) that is seen in Fig 1.3(a). This may be an indication of some other transitions specific to the material properties of volborthite and vesignieite.

Y. Narumi et. al. observed the $m = \frac{1}{3}$ plateau in another Kagome compound with an even lower $J \approx 19$

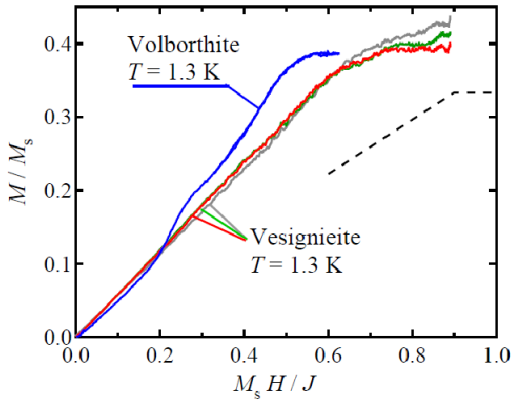

(a) Magnetization Plateaus in volborthite and vesignieite [61]. The data has been normalized using the different values of J for the two materials.

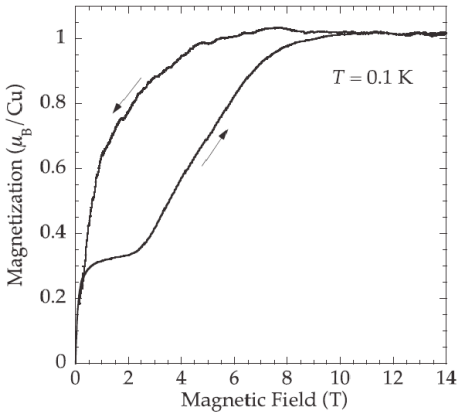

(b) Manetization plateau in Cu-titmb [58]

Figure 1.3: Evidence of magnetization plateaus in experiment.

K[58]. The plot in Fig 1.3(b) shows two curves, one for increasing magnetic field and another for decreasing magnetic field. They observe a plateau only for increasing field. Further, the appearance of the plateau is also sensitive to the sweep rate. The authors argue that the plateau in this material might be metastable as the second neighbor interactions are significant $J_2 \approx 6$ K and may play an important role.

1.3 Heisenberg Model

The above experimental materials can be thought of as strong Mott insulators (half-filled systems that are insulating due to strong interaction effects). These materials tend to have a Mott charge gap of the order of a few eV and a much smaller exchange coupling. The spins in such materials can be modeled as Heisenberg spins with an anti-ferromagnetic (AFM) exchange coupling. The Hamiltonian for the more generic XXZ Heisenberg (AFM) model ($J > 0$) is

$$H = J \sum_{<i,j>} \left[S_i^x S_j^x + S_i^y S_j^y + \lambda S_i^z S_j^z \right] - h \sum_i S_i^z \tag{1.1}$$

where $\vec{S}_i$ are Heisenberg spins that live on some site i of the lattice, λ is an anisotropy parameter in the z-direction and h is an external magnetic field.

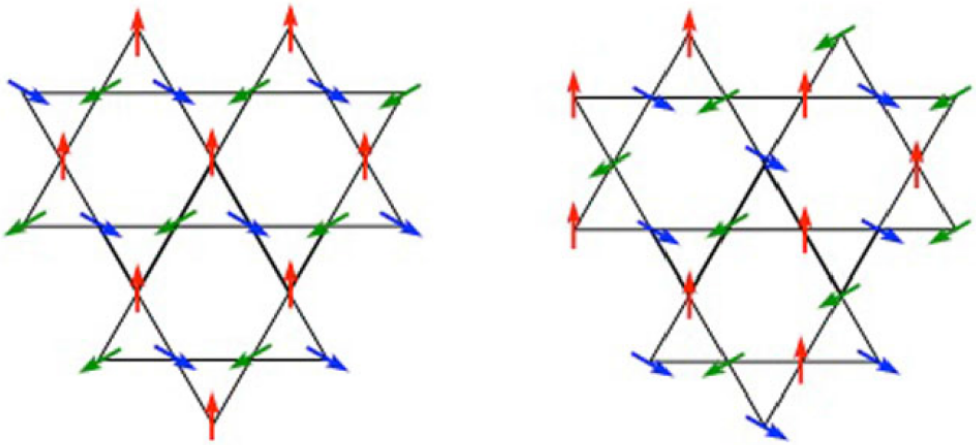

(a) $q = 0$ state. Classically favored for $J' < 0$.

(b) $\sqrt{3} \times \sqrt{3}$ state. Quantum fluctuations select this to be the large-S ground state [11]

Figure 1.4: Two possible ground states for nearest neighbor Heisenberg AFM.

1.3.1 $h = 0$, $\lambda = 1$ case

This is the isotropic model without any magnetic field and is probably the most commonly studied model.

$$H = J \sum_{\langle i,j \rangle} \vec{S}_i \cdot \vec{S}_j \tag{1.2}$$

Semiclassical Analysis (Large S)

This system is again highly degenerate and classically the only requirement for a particular spin configuration to be a ground state is that the total spin on any elementary triangle add to zero. As a result given a particular ground state configuration, one can still rotate certain spins giving rise to an extensive ground state degeneracy. One way to break this degeneracy is to introduce a next nearest neighbor interaction term (J') and treat this term as a perturbation. Such a term would break the degeneracy by an order by disorder mechanism. The effects of quantum fluctuations can be included in a perturbative manner by performing a semi-classical $\frac{1}{S}$ expansion (in powers of $\frac{1}{S}$) around the classical solution. Within this expansion, it has been shown that the quantum fluctuations select the $\sqrt{3} \times \sqrt{3}$ state (Fig 1.4(b)) as the large-S ground state regardless of the sign of J' [12] [33]. The other classical $q = 0$ ground state is also shown in Fig 1.4(a).

Spin $\frac{1}{2}$ case

The above analysis only holds true for large S. The case of $S = \frac{1}{2}$ (extreme quantum case) still remains inconclusive. Different works seem to favor different types of states, a few of which are listed below.

Resonating valence bond states: One of the first attempts to create a non-magnetic state in spin systems was by writing down a wavefunction comprised of singlets. Each singlet has no magnetization and the entire lattice can be tiled in such a manner giving what is called a valence bond state as shown in Fig 1.5(a). The singlet wave function on the two sites i and j forming the singlet is written as

$$|\psi_{ij}\rangle = \frac{1}{\sqrt{2}} \left(|\uparrow_i \downarrow_j\rangle - |\uparrow_j \downarrow_i\rangle \right) \tag{1.3}$$

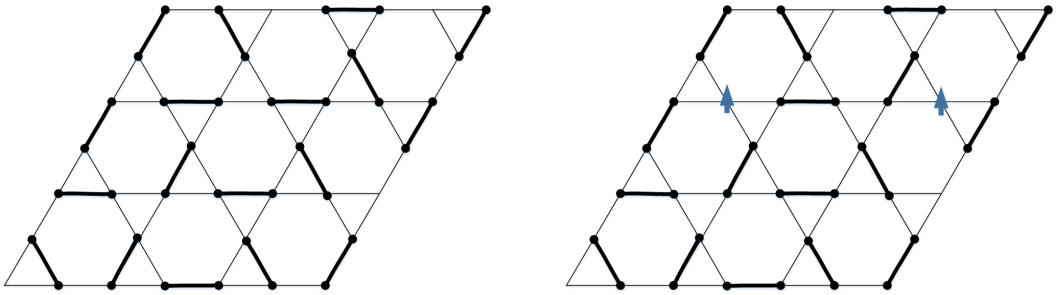

(a) Valence bond solid constructed by tiling the entire lattice with a particular singlet configuration.

(b) A spinon excitation arising from breaking a singlet and flipping a spin.

Figure 1.5: A particular nearest neighbour or short range valence bond crystal (VBC) configuration and spinon excitations. Singlets are represented by the dark bonds in the figure.

In Fig 1.5 all the valence bonds (or singlets) are amongst nearest neighbours. In such a case the resulting VBC is referred to as a short-range VBC. Once can also construct a configuration that leads to a long-range VBC by having singlets between sites at any arbitrary location.

Though the above VBC is disordered and has no magnetization, it breaks the symmetries of the lattice and by itself cannot be a good candidate for a spin liquid. However, one can restore this symmetry by considering all possible configurations of VBC's on the lattice. Such an equal amplitude superposition of all possible configurations is called a resonating valence bond state or RVB for short and is a good candidate for realizing a quantum spin liquid. The excitations in such a system would correspond to spin flips. Fig 1.5 shows an example of such an excitation. If these excitations can be pulled further apart, this leads to a deconfined state with spinon excitations. A spinon is essentially a particle with no charge (neutral) and with a spin of $\frac{1}{2}$.

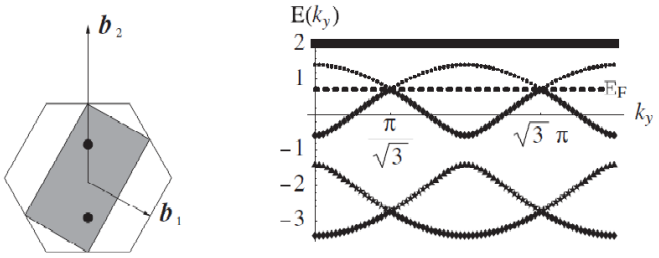

Figure 1.6: $U(1)$ Dirac spin liquid spectrum [64]. The figure on the left shows the reduced B.Z. The figure on the right shows the spectrum along a particular line in the B.Z. The dotted line indicates the Fermi level.

$\mathbb{Z}_2$ spin liquid: The most promising ground state candidate for the $S = \frac{1}{2}$ quantum Heisenberg model appears to be the $\mathbb{Z}_2$ spin liquid. The $\mathbb{Z}_2$ spin liquid is gapped and is a topological state with non-trivial ground state degeneracy. Such a state is time reversal invariant and is some times referred to as the double-semion model. The $\mathbb{Z}_2$ spin liquid can also be thought of as an RVB state with long range singlets.

A recent numerical DMRG (density-matrix renormalization group) study suggested that the ground state resembles a gapped $\mathbb{Z}_2$ type spin liquid state [85]. Another theoretical study [63] seems to indicate that a $\mathbb{Z}_2$ spin liquid state agrees well with the experimental data obtained for Herbertsmithite [31]. A $\mathbb{Z}_2$ spin liquid has also been proposed by Wang and Vishwanath[73] (using slave boson methods), and by Fisher, Balents and Girvin[3, 35], in generalized ferromagnetic XY model with ring-exchange interactions. Similarly, a $\mathbb{Z}_2$ spin liquid was shown to be the ground state for the Kagome antiferromagnet in the quantum dimer approximation.[54]

$U(1)$ dirac spin liquid: Another candidate is the $U(1)$ Dirac spin liquid which is a gapless spin liquid state. [64] [34]. This state has a doubled unit cell with Dirac points as shown in Fig 1.6. There is also some numerical work that indicates that the energy of the $U(1)$-Dirac spin liquid is comparable and quite competitive to the $\mathbb{Z}_2$ spin liquid. [34]

We would also like to point out that in our analysis of the $S = \frac{1}{2}$ Heisenberg model in Ch 5, we obtain a very similar looking spectrum at the mean-field level.

Valence bond crystal: Another state that has been observed using more advanced (but biased) numerical techniques is the valence bond crystal state.[22] These results seem to indicate that there is no spin liquid present in such a system. The numerical method used is an entanglement renormalization group calculation (MERA) and the exact state it favours is a complex 36 site VBC similar to the one proposed by Marston and Zheng. [51]

There are also other studies that indicate the possibility of other symmetry breaking states [14] or even

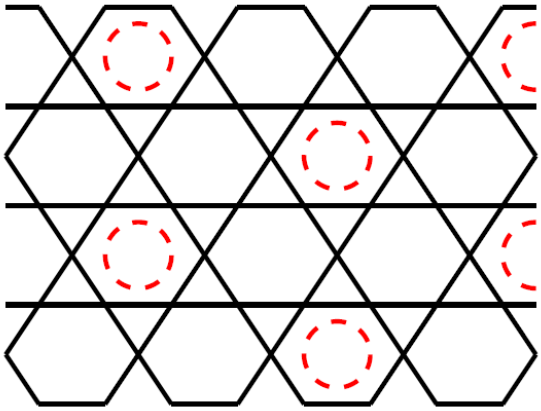

Figure 1.7: VBC for $m = \frac{1}{3}$ plateau in Ising regime [10]. The red circles indicate local resonances on those particular hexagons.

a chiral spin liquid state [86] [52]. The numerical energies obtained for a lot of these states are comparable and it is not yet clear which state truly represents the ground state of such a system.

1.3.2 $h \neq 0$ case (Magnetization plateaus)

As discussed earlier, under the influence of an external magnetic field, these systems can give rise to magnetization plateaus. Various magnetization plateaus have been predicted at different values of magnetization of which the one at $m = \frac{1}{3}$ plateau is the most prominent.

Valence bond crystal: Again there has been a lot of work trying to characterize the nature and properties of these plateaus. Numerical works focusing primarily on the Ising regime ($\lambda \gg 1$) of the Kagome Heisenberg AFM in an external magnetic field favor a valence bond crystal (VBC) type state with an enlarged unit cell (based on the $\sqrt{3} \times \sqrt{3}$ structure in Fig 1.4(b)) [9, 10, 59] as shown in Fig 1.7. In Fig 1.7, the hexagons with circles correspond to resonating valence bonds and all the remaining sites have spins (presumably polarized along the direction of the magnetic field).

Chiral spin liquid: A chiral spin liquid state is one that breaks time-reversal symmetry and has topological characteristics analogous to quantum Hall states. Previous works focusing on XY regime ($\lambda \ll 1$) in other frustrated lattices (triangular and Shastry-Sutherland) argued that these magnetization plateaus might possess characteristics similar to a quantum hall type states at least at the mean-field level [53, 86]. Though these results are quite promising they neglect the effects of fluctuations which is expected to play an important role in these strongly interacting systems. What we present in this thesis is a more rigorous treatment of the same model by systematically accounting for fluctuatations and showing that such chiral

spin liquid states are indeed possible on the Kagome lattice. This was in fact one of the primary motivations of this thesis and for constructing the necessary lattice Chern-Simons theory required to study these states.

1.4 Other interactions

Next I discuss some other interaction terms on the Kagome lattice, primarily motivated by numerous numerical works, that can also give rise to spin liquid states.

1.4.1 Chirality terms

In a recent and insightful work Bauer and coworkers[6] considered a Kagome antiferromagnet with a term proportional to the chiral operator on each of the triangles of the Kagome lattice. The chiral Hamiltonian can be written as

$$H_{chiral} = h \sum_{\triangle} \vec{S_i} \cdot (\vec{S_j} \times \vec{S_k}) \tag{1.4}$$

where the sum runs over all the triangles of the lattice and i, j and k refer to the three sites on any given triangle with orientation fixed.

In this model time-reversal invariance is broken explicitly. These authors used a combination of DMRG numerical methods and analytic arguments to show that, at least if the time-reversal symmetry breaking term is strong enough, the ground state is a chiral spin liquid state in the same topological class as the Laughlin state for bosons at filling fraction 1/2. A similar state was also found by us [43] in the 1/3 and 2/3 magnetization plateaus and a portion of this thesis will consist of a discussion on this topic in Ch 5.

1.4.2 Dzyaloshinskii-Moriya term

Another term that will be considered is the Dzyaloshinskii-Moriya interaction which is an antisymmetric exchange interaction between two neighbouring spins and is written as

$$H_{DM} = \sum_{\langle i,j \rangle} \vec{D}_{ij} \cdot (\vec{S_i} \times \vec{S_j}) \tag{1.5}$$

where the sum is defined so that it is always clock-wise around any elementary triangle on the Kagome lattice.

It has also been shown that these interactions are present in Kagome lattices and can give rise to or favour certain magnetic phases. [18] Moriya also presented some rules that can be used to determine the direction of the $\vec{D}_{ij}$ vector based on some symmetry rules. [57] When this is applied to a perfect Kagome lattice, the

$\vec{D}_{ij}$ vector can only be perpendicular to the Kagome plane (which has mirror symmetry associated with it). [18] When the Kagome lattice has imperfections as in the cases of some experimental material the above condition might not hold true. Nevertheless, for the rest of this paper and primarily in Ch 5, we will take $\vec{D}_{ij} = \hat{z}$ i.e. to point in the direction perpendicular to the plane. (There are also other restrictions due to our theoretical model which prevent us from analysing a more general $\vec{D}_{ij}$ vector and will become clear in later chapters.) The below model was also analysed by B.Bauer and coworkers [6]. Hence, the resultant Hamiltonian that we will focus on in Ch 5 is

$$H_{DM} = \sum_{\langle i,j \rangle} \hat{z} \cdot (\vec{S}_i \times \vec{S}_j) \tag{1.6}$$

where again the nearest neighbour sum is defined so that it is always clockwise around any triangle on the Kagome lattice.

1.4.3 Second and third neighbour interactions

There are now numerous works that have shown that the inclusion of second neighbor and third neighbor interactions can lead to spin liquid states. S. Gong et. al. showed that the inclusion of second and third neighbor Heisenberg terms to the model leads to a chiral spin liquid with $\nu = \frac{1}{2}$. [29] A similar work showed that having further neighbor interactions of an Ising form in addition to the nearest neighbor Heisenberg model can also give rise to a chiral spin liquid state. [32] In both these cases the second and third nearest neighbor interactions are comparable and in some cases stronger than the nearest neighbor interactions. A more complex phase diagram was recently found in a model that also included second and third neighbor exchange interactions.[81] Another recent exact diagonalization and DMRG study found evidence of a chiral spin liquid at one-third bosonic filling when second and third neighbor interactions were included. [89]

All of the above works seem to strongly indicate that these further neighbor interactions seem to stabilize a spin liquid state. Unfortunately, as will be shown in Ch 2, our theoretical model suffers from the drawback of only being applicable to the nearest neighbor Heisenberg model. We can, however, include Ising terms of this form and we will comment on this aspect in the following chapters.

1.5 Theoretical tools

The Heisenberg AFM is a strongly interacting problem and as such is difficult to solve directly. Below I list a couple of popular theoretical tools that are commonly used in literature to study such systems. Then I will introduce the flux attachment transformation which will be the primary method used in the rest of this

thesis.

1.5.1 Spin wave theory

Probably one of the first methods used to study such systems involves the spin wave theory or semi-classical calculations. Here one assumes that the quantum fluctuations are small and performs an expansion in powers of $\frac{1}{S}$. In order to do this one generally uses the Holstein-Primakoff representation for each of the spin operators (This mapping essentially maps the spin operators to bosons.)

$$\begin{aligned} S_i^z &= S - a_i^\dagger a_i \\ S_i^+ &= \sqrt{2S - a_i^\dagger a_i}\, a_i \\ S_i^- &= a_i^\dagger \sqrt{2S - a_i^\dagger a_i} \end{aligned} \tag{1.7}$$

where the sub-script i refers to the site label, S refers to the total spin and a_i are bosons. One then performs an expansion in powers of $\frac{1}{S}$. This is followed by first considering and diagonalizing just the quadratic terms in the expansion. Then a perturbative analysis is performed on the higher order terms to account for the interactions. The results summarized in Sec 1.3.1 essentially utilize the above method.

1.5.2 Slave methods

One of the most common tools used to study the $S = \frac{1}{2}$ frustrated Heisenberg AFM involve either representing the spin operators as slave fermions [5, 76] or slave bosons [2, 66]. The slave fermion construction proceeds by expressing the spin operators in terms of fermionic operators f_α.

$$\begin{aligned} \vec{S}_i &= \frac{1}{2} f_{i\alpha}^\dagger \vec{\sigma}_{\alpha\beta} f_{i\beta} \\ f_{i\alpha}^\dagger f_{i\alpha} &= 1 \end{aligned} \tag{1.8}$$

where $\vec{\sigma}$ are the Pauli matrices. The above construction enlarges the original Hilbert space and a constraint is needed to restrict the space of possible fermionic states. The slave boson method uses a similar approach but in terms of Schwinger bosonic operators a as shown below (a similar constraint is required here)

$$\begin{aligned} \vec{S}_i &= \frac{1}{2} a_{i\alpha}^\dagger \vec{\sigma}_{\alpha\beta} a_{i\beta} \\ a_{i\alpha}^\dagger a_{i\alpha} &= 1 \end{aligned} \tag{1.9}$$

These constructions help study different spin liquid states in terms of fermionic or bosonic models. Both these approaches have been used extensively in theoretical and numerical works and many of the results stated in the previous section tend to rely on either one of these methods. Both these approaches work well at the mean-field level but suffer from the limitation that there is no small parameter about which the fluctuations can be treated in a consistent manner. Controlled calculations have been performed by generalizing the $SU(2)$ quantum Heisenberg antiferromagnetic model to an $SU(N)$ or $Sp(N)$ spin model on the Kagome lattice[66, 74] but it is not clear if the results obtained in the large-N limit remain valid for the experimentally relevant case of $N = 2$.

1.5.3 Flux attachment transformation

In this work we will analyze Heisenberg model using an alternative approach based on a newly generalized version of the two dimensional **flux attachment transformation** [24]. This flux attachment transformation maps the spins, which are hard-core bosons, onto spinless fermions but the fermions are now coupled to a Chern-Simons gauge field in order to change the statistics of the spins to fermions. As a result this mapping depends on being able to define a consistent Chern-Simons term on the Kagome lattice. At the mean-field level, the details of this lattice Chern-Simons term can be ignored and this approach was used to look at magnetization plateaus in frustrated systems like the triangular lattice and the Shastry-Sutherland lattice [53]. Similarly, the above method was also used to predict the existence of a chiral spin liquid in triangular and Kagome lattices [86].

Chern-Simons theories have been very successful in studying and explaining fractional quantum Hall (FQH) type states. These theories yield reliable results in gapped systems and thus may present some new insight into the problem of frustrated quantum systems. For these reasons they have been used for quite some time to study quantum antiferromagnets on frustrated lattices (triangular, Kagome, Shastry-Sutherland, and others) yielding intriguing results of possible spin liquid phases.[86, 53] In these works the systems were treated only at the level of the average field approximation, and the role of the quantum fluctuations of the Chern-Simons gauge field were ignored. However, these fluctuations are crucial to the physics of this systems. This is a well known issue from analogous theories of FQH fluids where these fluctuations play a key role in the physics of the excitations, and in particular their fractional statistics (for a detailed recent discussion of this problem in the FQH fluids see Ref. [[26]].)

However the existing lattice Chern-Simons theory[24] (and its more refined and consistent version by Eliezer and Semenoff[21]) can only be used for systems on a square lattice and, in particular, it cannot be used for frustrated systems on non-bipartite lattices. The Chern-Simons action encodes two key features: 1)

the local constraint requiring the states to be locally gauge invariant (in the form of a Gauss-type law) and 2) a definition of the canonical pairs of fields. The first condition, which for a Chern-Simons theory is a relation between the charge on a site and the gauge flux in an adjacent "plaquette", must be obeyed at all sites of the lattice and not just on average. This condition requires that the gauge fluxes on different "plaquettes" must commute with each other since otherwise the constraints do not commute with each other (even through while they may still commute locally with the Hamiltonian). This consistency condition sets a restriction on the commutation relations of the gauge fields. Eliezer and Semenoff[21] showed how to impose these conditions consistently for the case of square lattice, at the expense of making the Chern-Simons action less local than would have naively expected.[24] It is easy to see that these constraints, even in a non-bipartite lattice, can only be imposed consistently provided that there is a one-to-one correspondence between sites and "plaquettes" of the lattice. In this work we will show that this procedure can also be done for the (non-bipartite) Kagome lattice that also exhibits this local one-to-one correspondence between the sites and plaquettes of the lattice. However, this approach does not work for the triangular lattice, for which there are two different adjacent triangles ("plaquettes") for each site of the lattice. Similarly, this procedure does not work for the (bipartite) hexagonal lattice for which two sites are associated with each hexagon.

1.6 Overview of thesis and key results

In this work we study the nearest-neighbor XXZ frustrated quantum Heisenberg antiferromagnet on the Kagome lattice using a generalization of the construction of the Chern-Simons gauge theory of Eliezer and Semenoff to the non-bipartite Kagome lattice which we present here. In this picture the flipped-spins are represented by hard-core bosons which in turn are described as a problem of fermions coupled to a Chern-Simons gauge field on the same lattice. This construction is one of the main results of this paper. First, we will begin by setting up the problem on the Kagome lattice in Ch 2 discussing some of the subtle issues that arise when performing the flux attachment transformation. Then we will derive the discretized version of the Chern-Simons term for the case of the Kagome lattice in the same chapter. The resultant fermionic theory coupled to the discretized Chern-Simons term will be the main theory that will be used for obtaining and characterizing the different magnetization plateau type states in Ch 4 and 5. Further, the effect of an external magnetic field can also be easily mimicked by adjusting the density of fermions in the equivalent problem. In addition to a magnetic field, we will also be able to explore the effects of adding a chirality term and a Dzyaloshinskii-Moriya term to the XXZ Heisenberg model. More importantly, this approach will allow us to go beyond the mean-field theory and analyze the effect of fluctuations in a consistent manner. It is

here, when we consider fluctuations, that the effects of the consistent constriction of the lattice Chern-Simons term are crucial.

In addition to discretizing the Chern-Simons term for the case of the Kagome lattice, we provide a generalization of this construction for a large class of generic 2D lattices in Ch 3.[70] We show that as long as there exists a local one-to-one correspondence between the sites and plaquettes of the lattice, one can write down a consistent version of the Chern-Simons gauge theory on the lattice that is gauge invariant and reproduces many of the topological characteristics of its continuum version. We find that the square, Kagome and dice lattices are examples of situations that satisfy the above criterion and a corresponding lattice version of the Chern-Simons term can be written down. However, other lattices such as the triangular and honeycomb lattices do not satisfy the local one-to-one correspondence condition and our method cannot directly be used for these lattices.

Next in Ch 4 we utilize the construction on the Kagome lattice presented in Ch 2 to analyse the magnetization plateaus that can arise in the nearest neighbor XXZ Heisenberg model. Within our approximations we find that, in the XY limit and for a wide range of the anisotropy parameter λ, the ground state of the $\frac{1}{3}$ magnetization plateau of the XXZ model on the Kagome lattice is equivalent to a Laughlin fractional quantum Hall state of hard-core bosons with filling fraction $1/2$. This fully gapped state is a topological fluid with a broken time reversal invariance. This is a state with spin currents in the ground state and with a fractional Hall spin conductance. It has a two-fold ground state degeneracy on the torus and has a single chiral gapless edge state on a disk geometry and the excitations of this state are semions. We also found two other plateaus states, one at magnetization $2/3$ and another one at $5/9$. The resultant phase of the $2/3$ plateau is equivalent to the $1/3$ plateau. The plateau at $5/9$ magnetization is also a topological fluid and is equivalent to the first Jain daughter state of the Laughlin FQH state for bosons at filling fraction $2/3$. In this case the state has two chiral edge states, has a three-fold ground state degeneracy on the torus and the excitations are anyons with statistical angle $\pi/3$. We also showed that, as expected, the spin-spin correlation functions decay exponentially as a function of distance while exhibiting an oscillatory behavior which reflects the breaking of time-reversal symmetry. For large enough anisotropy we find a quantum phase transition to time-reversal invariant states which extend all the way to the Ising limit, where it has been shown[9] that the ground state is governed by a quantum order-by-disorder mechanism and that it equivalent to a complex valence-bond solid. A possible time-reversal invariant $\mathbb{Z}_2$ spin liquid has been conjectured to exist at intermediate values of the anisotropy.

In Ch 5, using the same flux attachment transformation, we also investigated the occurrence of chiral spin liquid states in three extensions of the quantum Heisenberg antiferromagnet on the kagome lattice: a)

by adding the chiral operator acting on the triangles of the Kagome lattice, b) by considering the effects of a Dzyaloshiskii-Moriya interaction, and c) by adding a ring-exchange term on the bowties of the kagome lattice. Both the chirality term and the Dzyaloshinskii-Moriya interaction break the time reversal invariance explicitly. This final ring-exchange term is equivalent to the product of two chiral operators of the two triangles on the bowtie and does not break time-reversal invariance explicitly. Such a term allows us to investigate the possibility of a spontaneous breaking of time-reversal symmetry.

We again find chiral spin liquid phases in the same topological class as the Laughlin state for bosons at filling fraction 1/2 occur for both the models with the chiral operator on the triangles and for the Dzyaloshinskii-Moriya interaction. We find that the chirality term opens up a gap in the spectrum and leads to a chiral spin liquid state with an effective spin Hall conductivity of $\sigma^s_{xy} = \frac{1}{2}$ in the XY regime. This is equivalent to a Laughlin fractional quantum Hall state for bosons similar to the $m = \frac{1}{3}$ magnetization plateau found in our earlier work.[43] We also show that this chiral state survives for small values of the Dzyaloshinskii-Moriya term. We also consider the effects of adding the chirality term and Dzyaloshinskii-Moriya terms in the presence of an external magnetic field at the mean-field level. Once again, this is expected to give rise to magnetization plateaus. In the XY regime, we again find some of the same plateaus that was already obtained for just the case of the Heisenberg model.[43] In addition, we also find an additional plateau at $m = \frac{1}{9}$ which has an effective spin Hall conductivity of $\sigma^s_{xy} = \frac{2}{3}$. Finally, we also observed that the ring-exchange term on the bowties of the kagome lattice, provided that the coupling constant of this ring-exchange term is large enough, triggers a spontaneous breaking of time-reversal symmetry and leads to a similar chiral spin liquid state with $\sigma^s_{xy} = \frac{1}{2}$. All of these results are presented in detail in Ch 5.

In the final Ch 6 we present some numerical results based on exact diagonalization studies on the $\frac{2}{3}$ plateau on the original XXZ nearest neighbor Heisenberg model studied in Ch 4. The higher value of magnetization allows us to study bigger sized clusters (up to 48 sites) from an exact diagonalization perspective. This state was found to be a chiral spin liquid with a spin Hall conductance of $\sigma^s_{xy} = \frac{1}{2}$ and whose effective excitations behave like semions. In this chapter we present some evidence of this statement by analysing the degeneracy of the spectrum and by computing modular matrices on various clusters. The modular matrices encode information about the mutual and self statistics of the quasi particles in the system and can be used to determine the existence of semions in such a lattice. We also compute the Chern numbers of the candidate topological states and show that it has the right chern number of $\frac{1}{2}$ as expected for a chiral spin liquid with spin Hall conductance of $\sigma^s_{xy} = \frac{1}{2}$. [7] More recently a chiral spin liquid with the right characteristics, as predicted by our theory, was also found for the case of the 1/3 magnetization plateau but in the presence of additional next and next-next nearest neighbor interactions. [89]

Chapter 2

Flux attachment transformation on Kagome lattice

In this chapter we briefly review the flux attachment transformation that maps the Heisenberg spins (which are hard-care bosons) to fermions coupled to a Chern-Simons gauge field on the Kagome lattice in this chapter. This mapping involves writing down a lattice or discretized version of the Chern-Simons term which we will explicitly derive for the case of the Kagome lattice. Such a transformation was first discussed in Ref. [[24]] and so far has only been applied to the case of the square lattice. What is presented here is essentially an extension of this procedure outlined in Ref [[19]] for the Kagome lattice. In the next chapter a more elaborate discussion on writing down a discretized Abelian Chern-Simons theory on certain classes of generic lattices will be presented.

I begin this chapter by first writing down the spin-$\frac{1}{2}$ XXZ Heisenberg model (which will be the main focus in Ch 4 and Ch 5) in Sec 2.2. Then I will describe the flux attachment transformation and derive the discretized version of the Chern-Simons theory for the case of the Kagome lattice in Sec 2.3.

2.1 Spin-$\frac{1}{2}$ XXZ Heisenberg model

The model that we will study is the nearest-neighbor XXZ Heisenberg model on the Kagome lattice in the presence of an external magnetic field h

$$H = J \sum_{\langle i,j \rangle} \left[S_i^x S_j^x + S_i^y S_j^y + \lambda S_i^z S_j^z \right] - h \sum_i S_i^z \tag{2.1}$$

where $J > 0$ for antiferromagnetic interactions, S_i^a (with $a = x, y, z$) are the three spin-1/2 operators at lattice site i, $\langle i, j \rangle$ stands for nearest neighboring sites, and λ is the magnetic anisotropy parameter along the z-direction. Later in Ch 5, we will consider further perturbations to the above Hamiltonian that can still be analysed using the flux attachment transformation developed in Sec 2.2.

2.2 Flux attachment transformation

Under the flux attachment transformation, the resultant action with fermions and the Chern-Simons gauge field becomes

$$S = S_F(\psi, \psi^*, A_\mu) + S_{\rm int}(A_\mu) + \theta S_{CS}(A_\mu) \tag{2.2}$$

where the fermionic and interacting parts are

$$\begin{aligned} S_F(\psi, \psi^*, A_\mu) =& \int_t \left[\sum_x \psi^*(x,t) \left(iD_0 + \mu \right) \psi(x,t) - \frac{J}{2} \sum_{\langle x,x' \rangle} \left(\psi^*(x,t) e^{iA_j(x,t)} \psi(x',t) + h.c \right) \right] \\ S_{\rm int}(\psi, \psi^*) =& \lambda J \int_t \sum_{\langle x,x' \rangle} \left(\frac{1}{2} - n(x,t) \right) \left(\frac{1}{2} - n(x',t) \right) \end{aligned} \tag{2.3}$$

where $D_0 = \partial_0 + iA_0$ is the covariant time derivative, $n(x,t) = \psi^*(x,t)\psi(x,t)$ is the fermion density operator (i.e. the site occupancy), and $\langle x, x' \rangle$ stands for nearest neighboring sites x and x' on the Kagome lattice. Under the transformation the z component of the spin operator, S^z, is mapped to the local fermion occupation number

$$S^z(x,t) = \frac{1}{2} - n(x,t) \tag{2.4}$$

We can then absorb the external magnetic field term in the Hamiltonian, $h \sum_i S^i_z$, in the definition of the chemical potential μ in Eq.(2.3). *Hence, the effect of the external magnetic field can easily be mimicked by adjusting the fermionic filling.*

In the flux attachment transformation the parameter θ is selected so that the statistics of the spins (which are hard-core bosons) are changed in to fermions. This can be done by choosing $\theta = \frac{1}{2\pi(2k+1)}$ for any $k \epsilon \mathbb{Z}$. Although the hard-core boson to fermion mapping holds for all integer (positive and negative) values of k, we will see below that for two special values, $k = 0, -1$ (or, equivalently, $\theta = \pm\frac{1}{2\pi}$), there is a mean field approximation with a fully gapped spectrum. The resulting states for these two choices of θ are related to each other by time reversal and hence by a reversal of the sign of the magnetization.

In order to complete the flux attachment transformation, the Chern-Simons term in Eq (2.2) needs to be specified. If one naively, extends the continuum version of the Chern-Simons term to a lattice, the flux attachment constraints cannot be imposed consistently as $[B(x), B(y)] \neq 0$ for any two sites x and y on the lattice.[26] Eliezer and Semenoff [21] developed a form of the Chern-Simons theory for a square lattice that can be consistently defined on a square lattice. This lattice Chern-Simons theory was subsequently used to successfully study the (unfrustrated) spin-$\frac{1}{2}$ quantum Heisenberg antiferromagnet on the square lattice.[49]

By generalizing the procedure outlined by Eliezer and Semenoff, we were able to develop a Chern-Simons

theory that can be consistently defined on the non-bipartite Kagome lattice. This will now allow us to use the flux attachment mapping to study the nearest-neighbor spin-$\frac{1}{2}$ quantum Heisenberg antiferromagnet on the Kagome lattice. The next section will briefly outline this procedure. A construction of the lattice Chern-Simons term for a general class of lattices is presented in Chapter 3.

2.3 Chern-Simons theory on the Kagome lattice

We begin by writing down the below generic form for the lattice Chern-Simons term

$$\begin{aligned} S_{CS} &= S_{CS}^{(1)} + S_{CS}^{(2)} \\ S_{CS}^{(1)} &= \int dt \sum_{x,y} A_0(x,t) J_i(x-y) A_i(y,t) \\ S_{CS}^{(2)} &= -\frac{1}{2} \int dt \sum_{x,y} A_i(x,t) K_{ij}(x-y) \dot{A}_j(y,t) \end{aligned} \tag{2.5}$$

where the A_0 fields are defined on the sites of the lattice and the A_i fields are defined on the links of the lattice. See Fig.2.1 for our definitions of these gauge fields on the unit cell of the Kagome lattice. Note that in Eq.(2.5) we have omitted the factor of θ.

The first term in Eq.(2.5) is the Gauss law term that imposes the constraint between local density and flux through the plaquettes of the Kagome lattice. The vector kernel $J_i(x-y)$ enforces the condition that relates the charge (i.e. the site occupancy by a fermions) to the gauge flux in the adjacent plaquette. Once a Gauss law has been fixed, the first term in Eq.(2.5) is completely determined. A key feature of the Kagome lattice (shared with the square lattice) is that there is a one-to-one correspondence between sites of the lattice and plaquettes of the same lattice. This condition is not satisfied in other planar lattices, e.g. honeycomb and triangular, which leads to flux attachment prescriptions which are ambiguous and break the symmetries of the lattice (see Ch 3).

The structure of the matrix kernel, denoted by $K_{ij}(x-y)$ in the second term in Eq.(2.5), determines the commutation relations between the different (spatial) gauge fields as follows

$$[A_i(x), A_j(x)] = -iK_{ij}^{-1}(x-y) \tag{2.6}$$

It is the structure of the matrix kernel $K_{ij}(x-y)$ in the second term of Eq.(2.5) that will allow us to consistently impose the Gauss law constraints on the lattice. This K matrix also satisfies the condition $K_{ij}(x-y) = -K_{ji}(y-x)$. Since there are six spatial links in the unit cell, this is a 6×6 matrix. *The*

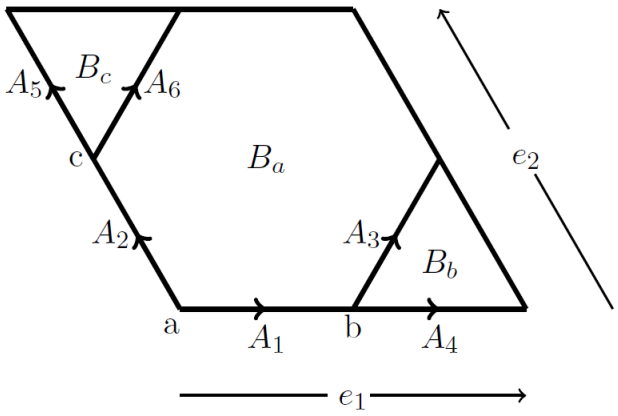

Figure 2.1: Kagome lattice unit cell with three sites attached to the fluxes in their corresponding plaquettes

key point is that a lattice Chern-Simons term can be uniquely determined by fixing a Gauss Law, imposing gauge invariance and demanding that the commutation relations between the A_j fields are "local". The last condition is primarily included to obtain the simplest form of the lattice Chern-Simons term. Now, we will proceed by establishing these conditions on the Kagome lattice and obtaining the Chern-Simons term. We should note that the matrix K_{ij} of Eq.(2.5) is unrelated to the so-called K-matrix that appears in the classification of abelian FQH states.[77]

2.3.1 Gauss' Law

The first step in writing down the Chern-Simons term is to determine how to impose the Gauss law (flux attachment) on the Kagome lattice. The unit cell of the Kagome lattice has three inequivalent sites (denoted by a, b and c in Fig.2.1) and three plaquettes (two triangles, denoted by b and c in Fig.2.1, and one hexagon, denoted by a in Fig.2.1). Thus, there is a natural correspondence between sites and plaquettes (just as in the case of a square lattice). It turns out that this is the crucial condition that needs to be satisfied in order to write down a Chern-Simons lattice term on a generic lattice.[70]

On the Kagome lattice, whose unit cell is shown in Fig.2.1, we define the flux through each plaquette (defined by the associated sites a, b and c) to be

$$\begin{aligned} B_a(x) =& A_1(x) + A_3(x) + A_5(x+e_1) - A_4(x+e_2) - A_6(x) - A_2(x) \\ B_b(x) =& A_4(x) + A_2(x+e_1) - A_3(x) \\ B_c(x) =& A_6(x) - A_1(x+e_2) - A_5(x) \end{aligned} \tag{2.7}$$

where e_1 and e_2 are vectors along the two directions of the lattice as shown in Fig.2.1. These equations attach the flux at sub-lattice a to that of the hexagon (B_a) and the fluxes of sub-lattices b and c to each of the two corresponding triangles (B_b and B_c respectively).

2.3.2 Gauge Invariance

The second step in writing down the Chern-Simons term is to demand that Eq.(2.5) is gauge invariant under the gauge transformations $A_0(x) \mapsto A_0(x) + \partial_0\Lambda(x)$ for time component of the gauge fields and $A_j(x) \mapsto A_j(x) + \Delta_j\Lambda(x)$ for the space components of the gauge fields (where Δ_j is the difference operator on the Kagome lattice). As an example, the field $A_1(x)$ gets transformed as $A_1(x) \mapsto A_1(x) + \Lambda^b(x) - \Lambda^a(x)$ under a gauge transformation where the labels b and a again refer to the sub-lattices and the field $\Lambda(x)$ lives on the sites of the lattice.

The gauge invariance condition is imposed on each of the sub-lattices and is written as

$$J_j^\alpha(x-y) + d_i^\alpha K_{ij}(x-y) = 0 \tag{2.8}$$

where $\alpha = a, b, c$ for each of the sub-lattices. The vectors J_j^α (introduced in Eq.(2.5)) and d_j^α are most easily written in Fourier space (for the Kagome lattice in Fig.2.1) as

$$\begin{aligned} J^a(k) &= (1, -1, 1, -e^{-ik_2}, e^{-ik_1}, 1) \\ J^b(k) &= (0, e^{-ik_1}, -1, 1, 0, 0) \\ J^c(k) &= (-e^{-ik_2}, 0, 0, 0, -1, 1) \end{aligned} \tag{2.9}$$

and

$$\begin{aligned} d^a(k) &= (-1, -1, 0, e^{ik_1}, e^{ik_2}, 0) \\ d^b(k) &= (1, 0, -1, -1, 0, e^{ik_2}) \\ d^c(k) &= (0, 1, e^{ik_1}, 0, -1, -1) \end{aligned} \tag{2.10}$$

2.3.3 Local Commutation Relations

So far we have established the Gauss Law and imposed gauge invariance. The final step is to look for a form of the matrix K_{ij} that is "local" i.e. only links (spatial gauge fields A_j) that touch one another have non-trivial commutation relations as given by Eq.(2.6). This is most easily seen in Fig.2.2 where the link A_1

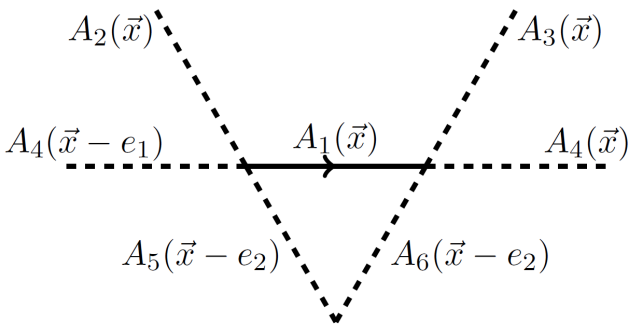

Figure 2.2: The field A_1 has non-trivial commutation relations with only these six links. This is the "locality" condition that is imposed.

is shown as an example. The link $A_1(x)$ has non-trivial commutation relations with just the six links that it touches and it commutes with all the other links on the lattice.

Using the above conditions one can obtain the below unique form of the matrix K

$$K_{ij} = \frac{1}{2}\begin{pmatrix} 0 & -1 & 1 & -S_2 & S_1+S_2^{-1} & -1+S_2^{-1} \\ 1 & 0 & 1-S_1^{-1} & -S_2-S_1^{-1} & S_1 & -1 \\ -1 & S_1-1 & 0 & 1-S_2 & S_1 & -1 \\ S_2^{-1} & S_1+S_2^{-1} & S_2^{-1}-1 & 0 & S_1S_2^{-1} & S_2^{-1} \\ -S_2-S_1^{-1} & -S_1^{-1} & -S_1^{-1} & -S_2S_1^{-1} & 0 & 1-S_1^{-1} \\ 1-S_2 & 1 & 1 & -S_2 & S_1-1 & 0 \end{pmatrix} \tag{2.11}$$

where S_j are shift operators along the two different directions (e_1 and e_2) on the lattice i.e. $S_j f(x) = f(x+e_j)$. Also since $\mathrm{Det}[K_{ij}] = 1$, the matrix K is invertible.

The above form of the matrix K in Eq.(2.11) ensures that the fluxes commute with each other for any pair of sites x and y on the Kagome lattice (i.e. $[B(x), B(y)] = 0$ for any x and y). This will allow us to impose the Gauss Law constraint consistently on each and every site of the Kagome lattice. More precisely, any two Wilson loops on the lattice commute, and Wilson lines on the lattice obey a signed intersection rule analogous to what happens in the continuum case of a Chern-Simons theory.

This completes the flux attachment transformation in Eq.(2.2) for the nearest-neighbor XXZ Heisenberg antiferromagnet on the Kagome lattice. Next, in Ch 3, we will elaborate on this method and provide a more rigorous description for writing down discretized Abelian Chern-Simons theories for a large class of generic lattices.

Chapter 3

Generic Lattices

In this chapter, we show how to discretize the abelian Chern-Simons gauge theory on generic planar lattices/graphs (with or without translational symmetries) embedded in arbitrary 2D closed orientable manifolds. We find that, as long as there exists a one-to-one correspondence between the sites (or vertices) and plaquettes (or faces) on the lattice (or graph), a discretized abelian Chern-Simons theory can be constructed consistently. We also verify that all the other essential properties of the Chern-Simons gauge theory are preserved in the discretized setup and that the discretized theory is nonsingular and preserves some of the key properties of a topological field theory. Most of this chapter is a summary of the results published in Ref [70].

3.1 Chern-Simons theory

In the continuum the (abelian) Chern-Simons Lagrangian of a gauge field $\mathcal{A}_\mu$ in 2+1 dimensions is (coupled to a matter current J_μ)

$$\mathcal{L}_{CS}[\mathcal{A}] = \frac{k}{4\pi}\epsilon^{\mu\nu\lambda}\mathcal{A}_\mu\partial_\nu\mathcal{A}_\lambda - J_\mu\mathcal{A}^\mu \tag{3.1}$$

The Chern-Simons (CS) gauge theory is a topological field theory.[84] At the classical level the CS action is independent on the metric of the manifold on which it is defined. The content of this Lagrangian, Eq(3.1), is seen in Cartesian components

$$\mathcal{L}_{CS}[\mathcal{A}] = \frac{k}{2\pi}\mathcal{A}_0\mathcal{B} - J_0\mathcal{A}_0 - \frac{k}{4\pi}\epsilon_{ij}\mathcal{A}_i\partial_t\mathcal{A}_j - \vec{J}\cdot\vec{\mathcal{A}} \tag{3.2}$$

At the quantum level, the first term of the r.h.s. becomes the requirement that the states in the physical Hilbert space, $\{|\text{Phys}\rangle\}$, obey the "Gauss law" as a local constraint. Thus, the physical states are gauge-invariant and are annihilated by the generator of local gauge transformations,

$$\Big[\frac{k}{2\pi}\mathcal{B}(\boldsymbol{x}) - J_0(\boldsymbol{x})\Big]|\text{Phys}\rangle = 0 \tag{3.3}$$

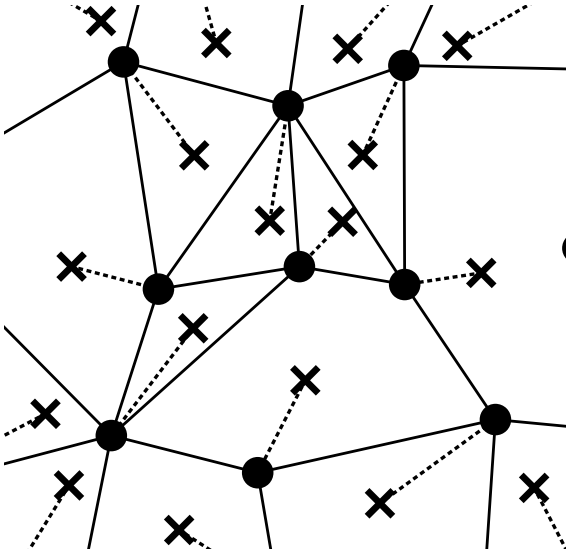

Figure 3.1: Part of a planar graph, on which a local vertex-face correspondence is defined. The disks and solid lines represent vertices and edges of the graph respectively. Each face is marked by a cross. The local vertex-face correspondence is indicated by dotted lines, that pair up each face with one (and only one) adjacent vertex.

Hence, the physical states are those in which the local charge density J_0 to the local magnetic flux $\mathcal{B} = \epsilon_{ij}\partial_i \mathcal{A}_j$ are precisely related, i.e. flux attachment. The second term of the r.h.s. of Eq.(3.2) implies that the components of the gauge field obey the equal-time commutation relations,

$$[\mathcal{A}_i(\boldsymbol{x}), \mathcal{A}_j(\boldsymbol{y})] = i\frac{2\pi}{k}\epsilon_{ij}\delta(\boldsymbol{x}-\boldsymbol{y}) \tag{3.4}$$

Further, the Hamiltonian of this system is zero unless sources are present, i.e.

$$\mathcal{H} = \vec{J}\cdot\vec{\mathcal{A}} \tag{3.5}$$

which is a consequence that a topological field theory does not have any excited states with finite energy.

As with any lattice gauge theory, in a discretized Chern-Simons gauge theory the gauge fields (which are connections and hence are 1-forms) are naturally defined on the links of the lattice while the matter fields are defined on the sites of the lattice.[82, 42] The field strength is a 2-form and it is defined on the elementary plaquettes of the lattice. While in a conventional lattice gauge theory the lattice is generally hypercubic (i.e. square in 2D), here we will consider more general (and translationally invariant) planar lattices. For instance, in Ref.[[24]] (and in Refs. [[19, 20]]) the Chern-Simons theory was defined on a square lattice and in Ch 2 (Ref.[[44]]) the theory was defined on a Kagome lattice. In both cases the Gauss law of

Eq.(3.3) is naturally implemented as a constraint that relates the occupation number of a site (or vertex) to the gauge flux through a (uniquely defined) adjoint plaquette (or face). While in the case of the square lattice all plaquettes are identical (squares), the case of the Kagome lattice has three inequivalent sites in its unit cell and, correspondingly, three faces (two triangles and a hexagon) in its unit cell. Nevertheless, the correspondence of vertices to faces is one-to-one in both lattices.

We will see here that this correspondence is a key feature which will allow us to impose the constraint (and hence gauge invariance) in a unique way which, in addition, does not break the point group (or space group) symmetries of the lattice. In Fig. 3.3, we show some examples of lattices that support such a correspondence (i.e. a discretized Chern-Simons gauge theory can be constructed on these lattices). These examples include some of the lattices used in the study of chiral spin liquids and the lattice fractional quantum Hall effect (e.g. the Kagome lattice).

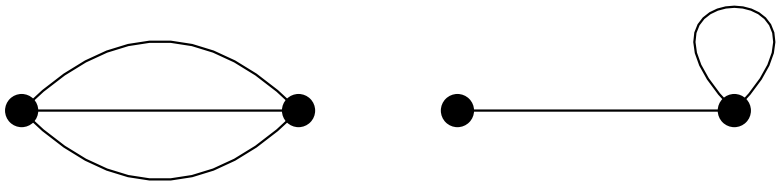

(a) (b)

Figure 3.2: Examples of graphs that are not simple. The figures demonstrate situations that are not allowed for a simple graph. Figure (a), shows a pair of sites connected by three different edges. In Fig. (b), one of the edges connects a site with itself (i.e. the two ends of a edge coincide).

In addition to those geometric considerations, a key consistency requirement of the gauge theory is that the lattice version of the local constraints of Eq.(3.3) must commute with each other and hence act as superselection rules on the Hilbert space [19, 20] (otherwise, these constraints cannot be simultaneously satisfied). This consistency condition places restrictions on the commutation relations satisfied by the gauge fields defined on the links. For the square lattice this problem was solved by Eliezer and Semenoff,[19, 20] and was more recently generalized by us to the case of the Kagome lattice.[44] In this paper we will show that the commutation relations can be defined consistently on any lattice (and graph) which obeys the one-to-one correspondence between vertices and faces. We will show that this restriction is implemented in terms of a suitably defined non-singular (and hence invertible) matrix. Therefore, the lattice Chern-Simons theory can be defined as a consistent gauge theory at the quantum level on these planar lattices and graphs.

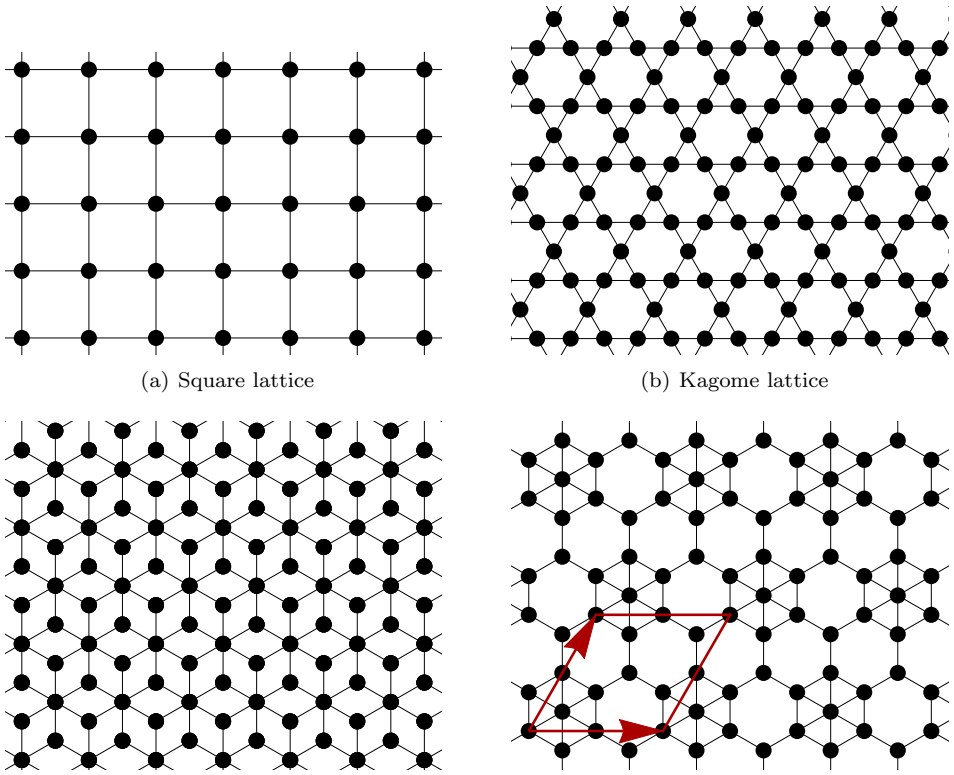

(a) Square lattice

(b) Kagome lattice

(c) Dice lattice

(d) Modified honeycomb lattice

Figure 3.3: (Color online) Examples of lattices and graphs that support local vertex-face correspondences. (a) a square lattice with 1 vertex and 1 face per unit cell, (b) a Kagome lattice with 3 vertices and 3 faces per unit cell, (c) a dice lattice with 3 vertices and 3 faces per unit cell and (d) a lattice that contains 9 vertices 18 edges and 9 faces per unit cell. The (red) parallelogram marks a unit cell with lattice vectors indicated by the two (red) arrows. It is easy to verify that for all these lattices $N_v = N_f$ and for any subgraphs the number of faces never exceeds the number of vertices, which is a sufficient and necessary condition for the existence of (at least) one local vertex-face correspondence.

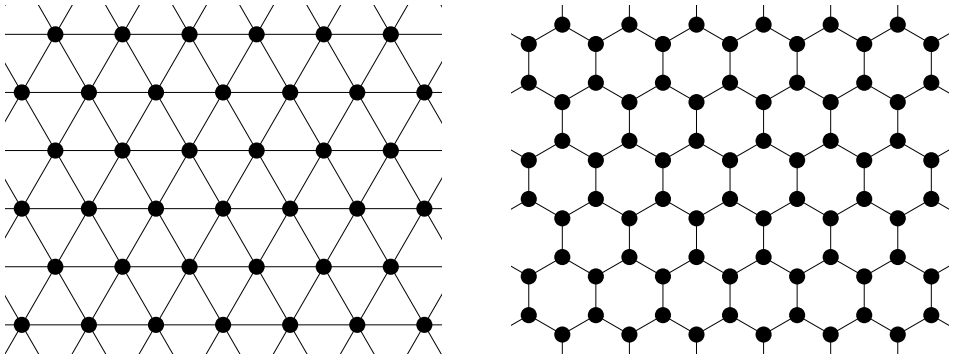

(a) Triangular lattice ($N_v < N_f$) (b) Honeycomb lattice ($N_v > N_f$)

Figure 3.4: (Color online) Examples of lattices/graphs that do not support a local vertex-face correspondence. (a) a triangular lattice, which has 1 vertex and 2 faces per unit cell ($N_v < N_f$), (b) a honeycomb lattice, which has 2 vertices and 1 face per unit cell ($N_v > N_f$).

3.2 Local vertex-face correspondence

We will only study generic *planar simple* graphs embedded on arbitrary closed and orientable 2D manifolds. Here, "planar" indicates that the graph can be drawn on a 2D manifold without any crossing bonds, while "simple" means no multiple bonds connecting the same pair of sites and no bond connecting a site to itself (See Fig. 3.2 for an explicit example). The "simple" condition is automatically implied for most (if not all) lattices studied in physics, while the "planar" condition holds for many (but not all) of them.

For a planar graph G, we can construct the dual graph G^* by mapping vertices to faces, and vice versa. It turns out that in order to write down a consistent gauge theory on G, one must also be able to write down a corresponding gauge theory on the dual graph G^* (as they can be shown to be related to one another), so we will also require the dual graph G^* to also be *simple*. For the original graph G, this condition implies that G cannot contain any dangling bonds, and that two faces in G can share at most one common edge.

From now on, we will focus our study on graphs, on which a local vertex-face correspondence can be defined. Below, in Sec. 3.9, we will prove that this constrain is necessary in order to preserve certain key defining properties of the Chern-Simons gauge theory.

To determine whether a graph can support such a local vertex-face correspondence, we will use the following criterion: A local vertex-face correspondence can be defined on a 2D planar graph G, if and only if the graph has the same number of vertices and faces (i.e. $N_v = N_f$), and that for any subgraph of G the number of faces never exceeds the number of vertices (i.e. $N_v' \geq N_f'$).

Using this criterion it is straightforward to determine whether or not a graph or lattice can support a local vertex-face correspondence. In Fig. 3.3 (Fig. 3.4), we provide examples of lattices/graphs, on which such a local correspondence exists (does not exist). In Fig. 3.4, the two lattices do not support any one-to-

one correspondence between vertices and faces, because the number of faces does not match the number of vertices.

In Figs. 3.3(b) and 3.3(c), the two lattices are dual to each other. Generically, if a graph G has a local vertex-face correspondence, so does its dual graph G^*. This is because one can construct such a correspondence for G^* by simply swapping the vertices and faces in the original vertex-face correspondence defined on G. As a result, our discretized Chern-Simons gauge theory always arises in pairs (one on the graph G and the other on the dual graph G^*). This duality relation is different from the continuum, in which the Chern-Simons theory is self-dual. A discretized Chern-Simons gauge theory is in general not self-dual, unless the underlying graph is self-dual. One example of a self dual graph is shown in Fig. 3.3(a), i.e., a square lattice.

For a graph G, we label the numbers of vertices, edges, and faces as N_v, N_e and N_f respectively, and we use the subindices v, e and, f to label each vertex, edge and face, respectively, where v, e and f take integer values ($1 \leq v \leq N_v$, $1 \leq e \leq N_e$ and $1 \leq f \leq N_f$). For the dual graph G^*, we will use the "$*$" symbol to label every object. For the gauge field, the time-component lives on vertices and thus will be labeled as A_v. The spatial components (i.e. the vector potential) are defined on edges, and thus will be shown as A_e. Because the vector potential is a vector, we must choose a positive direction for each edge (from one of its end to the other). The vector potential A_e on an edge e is positive (negative), if it is along (against) the direction of the edge e. In graph theory, after a direction is assigned to each edge, the graph is called a directed graph (or a digraph).[83]

3.3 The discretized Chern-Simons action

In this section, we construct the action of the discretized Chern-Simons gauge theory. We should emphasize that as long as the conditions discussed in the previous section are satisfied, our construction is applicable for arbitrary graphs. In addition, as will be shown below, the discretized gauge theory obtained here is a topological field theory, whose action only relies on the connectivity of the graph without any free parameter, except for a quantized topological index k.

3.3.1 The M matrix and the K matrix

In this section, we define two matrices for arbitrary graphs with a local vertex-face correspondence. For a graph satisfying the criterion given in the previous section typically there is more than one way to define the local vertex-face correspondence, and different choices here will in general result in different M and

K matrices and thus lead to slightly different actions. Here we choose an specific (albeit arbitrary) one, consistently throughout the lattice.

The vertex-face correspondence defines a matrix $M_{v,f}$ with dimensions $N_v \times N_f$. The first index of this matrix runs over all vertices, while the second one indicates faces in the graph. If vertex v and face f are paired-up according to the vertex-face correspondence, then $M_{v,f} = 1$. Otherwise, the matrix element is zero. Hence,

$$M_{v,f} = \begin{cases} 1 & \text{if } v \text{ is paired with } f \\ 0 & \text{otherwise} \end{cases} \tag{3.6}$$

Because the vertex-face correspondence requires $N_v = N_f$, the matrix M is a square matrix. In addition, it is easy to realize that, by definition, M is an invertible and orthogonal matrix, i.e. the inverse matrix M^{-1} is the transpose matrix, $M^T = M^{-1}$. The M matrix can essentially be thought of as the flux attachment part or Gauss Law part of the Chern-Simons action (analogous to the discussion in Ch 2).

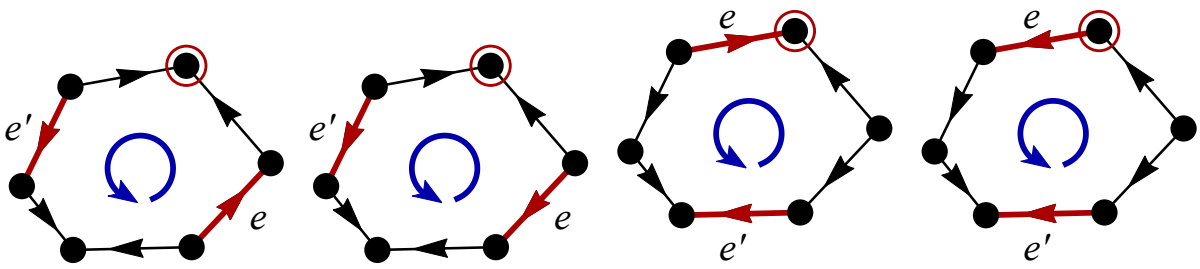

(a) $\eta_1 = +1$ and $\eta_2 = +1$ (b) $\eta_1 = +1$ and $\eta_2 = -1$ (c) $\eta_1 = -1$ and $\eta_2 = +1$ (d) $\eta_1 = -1$ and $\eta_2 = -1$

Figure 3.5: (Color online) Nonzero components of the K matrix. Here, we consider two edges e and e', which belongs to the same face f (otherwise $K_{e,e'} = 0$). Based on the local vertex-face correspondence, the face f is paired up with one of its vertices, which is marked by the (red) circle. We go around the face f from e to e' by following the direction of the positive orientation marked by the (blue) circle at the center of the face. In Fig. (a) and (b), the path from e to e' goes through the special site (marked by the red circle), and thus $\eta_1 = +1$. For Figs. (c) and (d), the special site is not on our path, and thus $\eta_1 = -1$. The sign of η_2 is determined by the orientation of e and e'. If their directions are both along (or opposite) to the direction of the positive orientation [Figs (a) and (c)], $\eta_2 = +1$. Otherwise [Figs. (b) and (d)], $\eta_2 = -1$. Once η_1 and η_2 are determined, the value of $K_{e,e'}$ can be obtained as $K_{e,e'} = -\eta_1 \times \eta_2/2 = \pm 1/2$.

In addition to M, the local vertex-face correspondence can be used to define another $N_e \times N_e$ square matrix, which we will denote by K, whose two indices run over all edges of the graph (with N_e being the

number of edges),

$$K_{e,e'} = \begin{cases} \pm\frac{1}{2} & \text{if } e \text{ and } e' \text{ belongs to the same face} \\ 0 & \text{otherwise} \end{cases} \tag{3.7}$$

If there exists a face f such that e and e' are both edges of this face, the component of the matrix $K_{e,e'}$ is $\pm 1/2$. Otherwise the matrix element vanishes. For nonzero $K_{e,e'}$, the $\pm$ sign is determined by the following formula,

$$K_{e,e'} = -\frac{\eta_1 \times \eta_2}{2} = \pm\frac{1}{2}, \tag{3.8}$$

where $\eta_1 = \pm 1$ and $\eta_2 = \pm 1$ are two $\mathbb{Z}_2$ integers.

The sign of η_1 is determined using the following rule. As shown in Fig. 3.5, we first mark the vertex that is paired up with f in the local vertex-face correspondence using a (red) circle. After that, we go from the edge e to the edge e' by moving counter-clockwise around the face f. If the path goes though the specially marked vertex (the red circle in Fig. 3.5), $\eta_1 = +1$, and otherwise $\eta_1 = -1$

The sign of η_2 is determined by the directions of the two edges e and e'. As discussed above, to define the vector potential, we must specify the direction for each edge. When we go around the face f in the counter-clockwise direction, if both e and e' are pointing along (or opposite to) the direction of the path, $\eta_2 = +1$. If one of them points along the path while the other is opposite, $\eta_2 = -1$.

With η_1 and η_2, their product (multiplied by -1), $-\eta_1 \times \eta_2 = \pm 1$, determines the sign of $K_{e,e'}$ in Eq. (3.7). Some examples can be found in Fig. 3.5. The K matrix enforces the commutation relations between the various gauge fields defined on the edges of the lattice/graph.

3.3.2 The Action

With the two matrices defined above, we can now write down the action of our discretized Chern-Simons gauge theory:

$$S = \frac{k}{2\pi} \int dt \left[A_v M_{v,f} \Phi_f - \frac{1}{2} A_e K_{e,e'} \dot{A}_{e'} \right]. \tag{3.9}$$

Here, we sum over all repeated indices. The index v, f and e run over all vertices, faces and edges respectively. A_v is the time-component of the gauge field, which lives on vertices and A_e represents the spatial components, which are defined on edges. Here, $\dot{A}$ represents the time derivative, K and M are the two matrices defined

in the previous subsection, and Φ_f is the magnetic flux on the face f, which equals to the loop integral of A_e around f,

$$\Phi_f = \xi_{f,e} A_e. \tag{3.10}$$

Here we sum over all edges and

$$\xi_{f,e} = \begin{cases} +1 & e \text{ is an edge of } f \text{ with positive orientation} \\ -1 & e \text{ is an edge of } f \text{ with negative orientation} \\ 0 & e \text{ is not an edge of } f \end{cases} \tag{3.11}$$

The sign of $\xi_{f,e}$ is determined by going around the face f along the counter-clockwise direction. If the direction of the edge e is along this path, $\xi_{f,e} = +1$. Otherwise, $\xi_{f,e} = -1$. As can be seen from Eq. (3.10), the matrix $\xi_{f,e}$ is a discretized curl operator ($\nabla\times$) for planar graphs.

On a square lattice, the action that we constructed here reduces to the action found in Refs. [19] and [20], which can be considered as a special situation of our generic construction. Similarly, for the Kagome lattice this general construction reduces to the construction that we presented the previous chapter and in Ref. [[44]].

We conclude this section by comparing our discretized theory with the Chern-Simons gauge theory in the continuum. For comparison, we choose to write down the action in the continuum in a special form

$$S = \frac{k}{2\pi} \int dt d\boldsymbol{x} \left(A_0 B - \frac{1}{2} A_i \epsilon_{i,j} \dot{A}_j \right). \tag{3.12}$$

Here A_0 is the time component of the gauge field. A_i and A_j are the spatial component with i and j being x or y. $\epsilon_{i,j}$ is the Levi-Civita symbol and B is the magnetic field perpendicular to the 2D plane. The first term here enforces the flux attachment and the second term dictates the dynamics of the vector potential A_x and A_y.

By comparing Eq. (3.9) with Eq. (3.12), we find that our discretized theory is in close analogy to the continuum case. Here, the M matrix dictates the flux attachment (i.e. Gauss' law) and the K-matrix plays the role of the Levi-Civita symbol. It is worthwhile to highlight that, just as the Levi-Civita symbol, the K matrix is antisymmetric

$$K_{e,e'} = -K_{e',e}, \tag{3.13}$$

This can be verified easily by noticing that $\eta_1 \to -\eta_1$ and $\eta_2 \to \eta_2$, if we swap e and e'. This antisymmetry property is in fact expected. If we look at the second term in our action, Eq (3.9), because $\int dt A_e \dot{A}_{e'} = -\int dt \dot{A}_e A_{e'}$ (integration by part), only the antisymmetric part of K contributes to the action.

In the next sections, we will demonstrate that our action indeed offers a discretized Chern-Simons gauge theory on generic graphs by showing that all the key properties of the Chern-Simons gauge theory are preserved by our action.

3.4 Gauge invariance

For a gauge theory, the action must be gauge invariant. In this section, we will verify that our action [Eq. (3.9)] preserves the gauge symmetry. In the case of Chern-Simons, this is also true provided the manifold has no boundaries. Furthermore, invariance under large gauge transformations (which wind around non-contractible loops of the systems) holds only if the index k is an integer.[84] These conditions are satisfied by our discretized Chern-Simons theory.

For a graph/lattice, a gauge transformation takes the following form

$$A_v \to A_v - \partial_t \phi_v \tag{3.14}$$

$$A_e \to A_e - D_{v,e}\phi_v \tag{3.15}$$

where ϕ_v is an arbitrary scalar function defined on vertices. The first formula [Eq. (3.14)] is the gauge transformation for the time component of the gauge field, while the second one [Eq. (3.15)] is for the spatial components. The matrix $D_{v,e}$ in Eq. (3.15) is the *incident matrix* of the graph [8]

$$D_{v,e} = \begin{cases} +1 & \text{if } v \text{ is the positive end of } e \\ -1 & \text{if } v \text{ is the negative end of } e \\ 0 & \text{otherwise} \end{cases} \tag{3.16}$$

Here, we called the vertex v a positive (negative) end of the edge e, if v is one of the two ends of e and the direction of the edge e is pointing towards (away from) v. The incident matrix contains all the information about the connectivity of the graph, as well as the direction assigned to each edge.[8] The incident matrix plays the role of a (discretized) gradient operator, $\boldsymbol{\nabla}$, which can be seen easily by noticing that

$$D_{v,e}\phi_v = \phi_{v_1} - \phi_{v_2} \tag{3.17}$$

where ϕ_v is an arbitrary scalar function and the edge e points from v_2 to v_1. As a result, Eq. (3.15) can be considered as a discretized version of $\boldsymbol{A} \to \boldsymbol{A} - \boldsymbol{\nabla}\phi$.

As proven in Appendix A, the sufficient and necessary condition for the action of Eq.(3.9) to be gauge-invariant is that the following identity is satisfied

$$M_{v,f}\xi_{f,e} = K_{e,e'}D_{v,e'} \tag{3.18}$$

where $\xi_{f,e}$ is defined in Eq. (3.11) and the incident matrix $D_{v,e'}$ is defined in Eq. (3.16). It can be shown that this condition is indeed valid for the M and K matrices constructed in Sec. 3.3.1.

3.5 Flux attachment

A key property of the Chern-Simons gauge theory is the constraint of flux attachment, which binds a magnetic flux with each charged particle. For a point charge q at location $\boldsymbol{r}_0$, the corresponding magnetic field is

$$B(\boldsymbol{r}) = \frac{2\pi}{k} q\, \delta^2(\boldsymbol{r} - \boldsymbol{r}_0), \tag{3.19}$$

In the continuum classical theory, the flux and the charge are located at the same position, as indicated by the δ-function in Eq. (3.19). In a continuum quantum gauge theory this condition is a constraint on the physical Hilbert space, and is the requirement that the quantum states be invariant under local time-independent gauge transformations,[16] as we discussed in the Introduction, c.f. Eq.(3.3). This condition requires regularization (in the form of splitting the position of the charge and the flux) which leads to a proper framing of the knots represented by Wilson loops.[84, 72, 62] For a discrete system, however, because electric charges live on vertices, while magnetic fluxes are defined on faces (which takes care of the regularization), it is necessary to specify one additional rule to dictate the location of the magnetic flux for charged particles at each site. This is achieved by the local vertex-face correspondence introduced in Sec. 3.1. Here too, this constraint amounts to the conditions that the states of the gauge theory be invariant under time-independent gauge transformations.[42]

Because our action, Eq. (3.9), does not contain any dynamics for the time component of the gauge field A_v (just as in any gauge theory), A_v is not a dynamical field but its role is to enforce a constraint.[16] By

taking a variational derivative of A_v, we get the charge at the vertex v,

$$q_v = \frac{\delta S}{\delta A_v} = \frac{k}{2\pi} M_{v,f} \Phi_f, \tag{3.20}$$

which is proportional to the magnetic flux in the face f. Because M is an orthogonal matrix, this equation implies that

$$\Phi_f = \frac{2\pi}{k} q_v M_{v,f}. \tag{3.21}$$

This equation is the discrete version of the flux attachment, analogous to Eq. (3.19).

Here, we find that for a charge at a vertex v, a magnetic flux is bound to it and the flux is located at the face f, which is the partner of v according to the vertex-face correspondence. This is the physical content of the vertex-face correspondence.

We conclude this section by emphasizing that the flux attachment rule here is *local*, because we have required the vertex-face correspondence to be *local*, i.e., the magnetic flux attached to a charge is located on a neighboring face. For a discrete system, this setup offers the closest analogy to the delta function in Eq. (3.19).

3.6 Commutation relations and the K^{-1} matrix

The Chern-Simons theory in the continuum has a very special commutation relations. In particular, the commutator between the loop integrals of the vector potential is a topologically invariant. We will show in this section that our discretized theory has the same property.

3.6.1 Commutators for the continuum case

For the Chern-Simons gauge theory in the continuum, for two arbitrary curves C and C', we have the following commutation relation

$$\left[\int_C A, \int_{C'} A\right] = \frac{2\pi i}{k} \nu\left[C, C'\right] \tag{3.22}$$

where $\nu[C, C']$ is the number of (oriented) intersections between the two curves, i.e. the number of right-handed interactions of C and C' minus the number of left-handed ones. [19]

If C and C' are closed loops, $\nu[C, C']$ is a topologically invariant, and it is easy to verify that its value

cannot change under any adiabatic procedures. In addition, if either C or C' can be contracted into a point (i.e. contractible), $\nu[C, C'] = 0$.

3.6.2 Canonical quantization

Using canonical quantization, it is straightforward to show that the conjugate field of the vector potential field A_{e_i} is

$$\frac{\delta S}{\delta \dot{A}_e} = \frac{k}{2\pi} K_{e,e'} A_{e'} \tag{3.23}$$

This formula implies that for our discretized Chern-Simons theory, the vector potential A_e (and linear superpositions of A_e's) play both the role of the canonical coordinates and that of the canonical momenta. Because canonical coordinates and canonical momenta arise in pairs, this result requires that we must have even number of linear independent A_es, i.e. the number of edges must be even. This is indeed true for any graphs considered here. Utilizing the Euler characteristic, we know that the numbers of vertices, edges and faces must satisfy the following relation

$$N_v - N_e + N_f = 2 - 2g, \tag{3.24}$$

where g is the genus of the underlying manifold. Because the vertex-face correspondence requires $N_v = N_f$, the number of edge is

$$N_e = 2N_f - 2 + 2g. \tag{3.25}$$

which is an even number.

In canonical quantization, the commutator between a canonical coordinate and the corresponding canonical momentum is $i\hbar$. Therefore, for our theory, we have

$$\left[A_e, \frac{k}{2\pi} K_{e',e''} A_{e''}\right] = i\delta_{e,e'} \tag{3.26}$$

where $\delta_{e,e'}$ is the Kronecker delta and we set $\hbar$ to unity. Multiplying both sides by the inverse matrix of K, we obtain the commutation relation for the vector potential

$$[A_e, A_{e'}] = i\frac{2\pi}{k} K^{-1}_{e',e} = -\frac{2\pi i}{k} K^{-1}_{e,e'} \tag{3.27}$$

Here, we used the fact that K^{-1} is an antisymmetric matrix.

In order to ensure that the commutator $[A_e, A_{e'}]$ is nonsingular, we must require the K matrix being invertible.

3.6.3 Paths, contractible and noncontractible cycles

In this section, we will introduce two concepts from the graph theory: *paths and cycles*, which are discrete versions of curves and loops, respectively. [83]

A *path* is a sequence of vertices $v_0 \to v_1 \to v_2 \to \ldots \to v_m$, in which any two consecutive vertices are connected by an edge. In the literature of graph theory it is often also assumed that a path never go through the same vertex twice. The length of a path is the total number of edges contained in the path.

If $v_0 \neq v_m$, the path is called *open*. For $v_0 = v_m$, the path is *closed*. A closed path (with nonzero length) is also called a *cycle*. In comparison with the continuum, it is easy to realize that open paths are discretized open curves, while cycles (i.e., closed paths) are discretized loops (i.e., closed curves). More precisely, a path (cycle) corresponds to a directed curve (loop), because a path (cycle) has a natural direction built in according to its definition, i.e. $v_0 \to \ldots \to v_m$.

In the continuum, loops on a 2D manifold can be classified into two categories: contractible or noncontractible, depending on whether or not the closed curve can be adiabatically contracted to a point. For a graph, there is a similar classification for cycles (closed paths) using a different but equivalent definition. We call a closed path (i.e. a cycle) contractible, if it is the boundary of some 2D area formed by a set of faces. Otherwise, it is noncontractible. For 2D closed and orientable surfaces in the continuum, noncontractible loops only exist for surfaces with nonzero genus (torus, double torus, etc.), while all loops on a genus zero surface (e.g. a sphere) are contractible. In graph theory, the same is true for cycles. For planar graphs defined on 2D closed and orientable surfaces, noncontractible cycle can only exist if the genus of the underlying 2D manifold is larger than zero.

For a directed graph (or lattice), each path (P) can be represented by a N_e-dimensional vector, ξ_P, whose eth component is

$$\xi_{P,e} = \begin{cases} +1 & e \in P \text{ and } e \text{ is along the direction of } P \\ -1 & e \in P \text{ and } e \text{ is opposite to the direction of } P \\ 0 & e \notin P \end{cases} \tag{3.28}$$

As will be shown in below, this object defines a discretized line integral. In particular, if P is a cycle, $\xi_{P,e}$ provides a discretized loop integral.

3.6.4 Commutators and intersections

For a path P on a graph G, we can define the integral (circulation) of the vector potential along this path as

$$\mathcal{W}_P = \xi_{P,e} A_e \tag{3.29}$$

This object is the discretized version of a line integral $\int_C \boldsymbol{A} \cdot d\boldsymbol{x}$ along a path C.

Now, we consider two different paths, P and P', and we define two integrals $\mathcal{W}_P$ and $\mathcal{W}_{P'}$ for P and P', respectively, using the definition of Eq. (3.29). In this section, we prove that the commutator between $\mathcal{W}_P$ and $\mathcal{W}_{P'}$ is determined by the number of oriented intersections between the two paths $\nu[P, P']$,

$$[\mathcal{W}_P, \mathcal{W}_{P'}] = \frac{2\pi i}{k} \nu\left[P, P'\right], \tag{3.30}$$

which is the direct analog of the corresponding commutator of the Chern-Simons theory in the continuum, Eq. (3.22).

Utilizing the commutator of Eq. (3.27), we find

$$[\mathcal{W}_P, \mathcal{W}_{P'}] = -\frac{2\pi i}{k} \xi_{P,e} \xi_{P',e'} K^{-1}_{e,e'} \tag{3.31}$$

If the two paths P and P' share no common vertex, the intersection number is obviously zero $\nu[P, P'] = 0$. In the same time, $[\mathcal{W}_P, \mathcal{W}_{P'}]$ also vanishes, because every term on the r.h.s. of Eq. (3.31) is zero.

If the two paths share some common vertices, only edges connected to these common vertices contribute to the commutator of Eq. (3.31), because $K^{-1}_{e,e'} = 0$ for all other edges. Therefore, we only need to consider edges adjacent to each common vertex. As shown in Fig. 3.6, we shall distinguish three different situations, shown in Figs. 3.6(a) to 3.6(c) respectively, depending on whether the common vertex is a right-handed intersection, a left-handed intersection, or not an intersection. In Fig. 3.6 we label the edges of P as e_1 and e_2, while the edges of P' are called e'_1 and e'_2.

If the common vertex is a right-handed intersection of P and P', Fig. 3.6(a), we get a contribution of $2\pi i/k$ to the commutator. Similarly, for a left handed intersection, we can prove $[\mathcal{W}_P, \mathcal{W}_{P'}] = -2\pi i/k$ for Fig. 3.6(b). For the case where the paths touch but do not cross we get $[\mathcal{W}_P, \mathcal{W}_{P'}] = 0$ for Fig. 3.6(c).

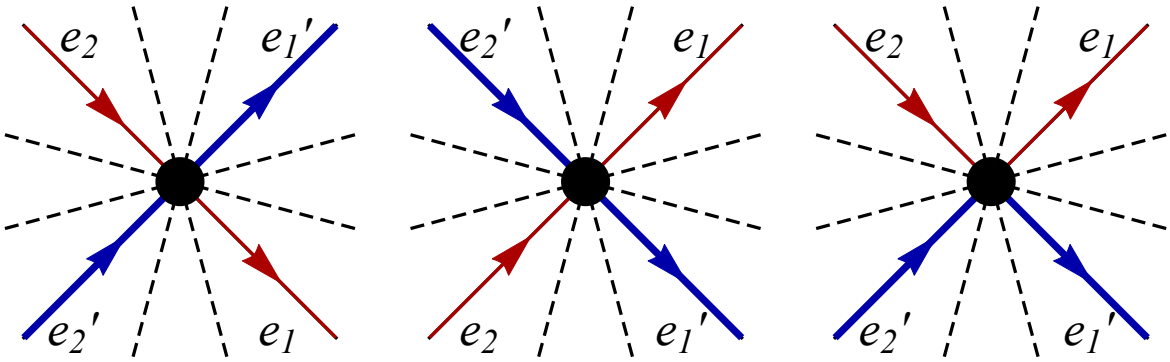

(a) Right-handed intersection ($\nu = +1$)

(b) Left-handed intersection ($\nu = -1$)

(c) No intersection ($\nu = 0$)

Figure 3.6: (Color online) One common vertex shared by two paths. Here, we consider two paths P (thin red solid lines) and P' (thick blue solid lines). The arrows indicate the direction of each path. The disk in the middle is one common vertex shared by the two paths. Dashed lines represent other (possible) edges that are connected to the vertex, and they don't contribte to the commutator that we want to compute. Figure (a) shows a right-handed intersection between P and P' and Fig. (b) is a left-handed one. In Fig. (c), the two paths don't intersect.

3.7 Wilson loops for non-contractible cycles

We start this section by considering a planar graph embedded on a 2D torus (with genus $g = 1$). For this graph, there are two independent non-contractible cycles (i.e. discretized counterparts of the two non-contractible loops on a torus), which will be labeled as C and C' in this section. These two cycles intersect once with each other. Without loss of generality, we choose the oriented intersection number to be $+1$, instead of -1, i.e., $\nu[C, C'] = +1$. As we proved above in Eq. (3.30), the commutator $[\mathcal{W}_C, \mathcal{W}_{C'}] = 2\pi i/k$.

Here we define Wilson loops for the two non-contractible cycles C and C' of the torus

$$W_C = \exp(i\mathcal{W}_C) \tag{3.32}$$

$$W_{C'} = \exp(i\mathcal{W}'_C) \tag{3.33}$$

Because the commutator $[\mathcal{W}_C, \mathcal{W}_{C'}] = 2\pi i/k$ is a complex number (i.e. is proportional to the identity operator), it commutes with both $\mathcal{W}_C$ and $\mathcal{W}'_C$. Hence, using the Baker-Hausdorff-Campbell formula it follows that

$$e^{i\mathcal{W}_C} e^{i\mathcal{W}'_C} = e^{i\mathcal{W}'_C} e^{i\mathcal{W}_C} e^{[i\mathcal{W}_C, i\mathcal{W}_{C'}]} \tag{3.34}$$

and thus

$$W_C W_{C'} = W_{C'} W_C e^{-2\pi i/k} \tag{3.35}$$

If we consider an eigenstate of W_C with eigenvalue w,

$$W_C|\Psi\rangle = w|\Psi\rangle \tag{3.36}$$

where w is a complex number, utilizing Eq. (3.35), it is straightforward to show that $W_{C'}|\Psi\rangle$ is also an eigenstate of W_C and its eigenvalue is $we^{-2\pi i/k}$

$$W_C(W_{C'}|\Psi\rangle) = we^{-2\pi i/k}(W_{C'}|\Psi\rangle) \tag{3.37}$$

In other words, we can consider $W_{C'}$ as a raising/lowering operator for the operator W_C, and vice versa. Starting from the eigenstate $|\Psi\rangle$, eigenstates of W_C can be generated by applying this raising/lowering operator,

$$W_C(W^n_{C'}|\Psi\rangle) = we^{-2n\pi i/k}(W^n_{C'}|\Psi\rangle) \tag{3.38}$$

i.e. $W^n_{C'}|\Psi\rangle$ is an eigenstate with eigenvalue $we^{-2n\pi i/k}$

For an integer k, it is easy to note that when $n = k$, the state $W^k_{C'}|\Psi\rangle$ has the same eigenvalues as $|\Psi\rangle$. If $W^k_{C'}|\Psi\rangle$ and $|\Psi\rangle$ are the same quantum state, $W^n_{P'}|\Psi\rangle$ generates k different eigenstates of W_P. From this results it follows the well known result that a Chern-Simons gauge theory has a k-fold topological degeneracy on a torus. This conclusion is well known in the continuum. Our discussion above shows that the same is true in our discretized theory. It is straightforward to generate the discussion above to other 2D manifolds with different genus.

3.8 Locality

In this section, we re-emphasize the point that our theory is *local*. More precisely, our action is local, (1) i.e. the action does not have any coupling between fields that are not around the same face, (2) the flux attachment is local, i.e. for a charge at the vertex v, its magnetic flux must be located on a neighboring face, and (3) the commutator between vector potentials is *local*, i.e. for any two edges that do share a common vertex, the vector fields defined on them commute with each other.

In the discretized action of Eq. (3.9) there are no long range couplings beyond edges and vertices of the same face. In the first term in Eq. (3.9), because $M_{f,v}$ vanishes unless f and v are adjacent to each other, the action only contains couplings between nearby A_v and A_e (i.e. e and v must belong to the same face). For the second term, we know that $K_{e,e'} = 0$, if e and e' do not belong to the same face, and therefore, only short-range coupling (for edges of the same face) is included in this term.

For the Chern-Simons gauge theory in the continuum, the flux attachment is *local*, i.e. for a point charge at r_0, the magnetic field is a delta function $B \propto \delta(\vec{r} - \vec{r}_0)$, and the B field vanishes when we more away from the point charge.

In our discretized theory, this condition of locality is preserved to the maximum extent. As shown in Eq. (3.21), for a charge at the site v, the corresponding magnetic field only is present inside *a single face*, which is the closest analog of a delta function in a discrete setup. As for the relative locations of the charge and its flux, because these two objects on different parts of the graph (charges on vertices and fluxes on faces), it is impossible to require their location to coincide. Instead, we require the charge and the flux to be adjacent to each other.

We emphasize that this locality condition plays a very important role, if we use the Chern-Simons gauge theory as a statistical field to change the statistics for matter fields coupled to it. To ensure that all particles have the correct statistics, when we move a particle A around another particle B, A must feel all the statistical field of B. In other words, no matter which path we choose, as long as A moves around B, the magnetic flux attached to B must be enclosed by the path of A. For our theory (and for the continuous Chern-Simons gauge theory), this is always true. However, if one were to violate the locality condition by putting the magnetic flux in a face not adjacent to the charge, it would be possible to move A around B without enclosing the flux inside the path. As a result, the statistics of the matter field would become ill defined.

Further, as shown in Eq. (3.27), the commutator for the vector potential is determined by the inverse of the K matrix. The K^{-1} matrix is also local, where the matrix element $K^{-1}_{e,e'} = 0$, if e and e' does not share a common vertex. This results implies that a nonzero commutator can only arise for two neighboring edges, while for two edges separated away from each other (i.e. not sharing a common vertex), the vector potential always commutes with each other.

3.9 Why $N_v = N_f$?

Above, we have shown that the existence of a local vertex-face correspondence is sufficient for the discretization of the Chern-Simons gauge theory. In this section, we prove that this condition is also necessary, if we want to preserve key properties of the Chern-Simons theory.

Let us consider a generic discretized action of gauge fields A_v and A_e. Just as in the Chern-Simons gauge theory in the continuum, we assume that the action does not contain time derivatives of the time component of the gauge field A_v, and that A_v plays the role of a Lagrange multiplier field that enforces a constraint on the local flux. For the coupling among the components of the gauge fields A_e on different edges, the action only contains product between A_e and $\partial_t A_{e'}$. We ignore possible terms with higher orders in time derivatives, which are less relevant in the sense of the renormalization group. In addition, we will only keep terms to the leading order in our action.

With these assumptions, the most generic action that one can write down is

$$S = \frac{k}{2\pi} \int dt \left[A_v M_{v,f} \xi_{f,e} A_e - \frac{1}{2} A_e K_{e,e'} \dot{A}_{e'} \right] \tag{3.39}$$

This action is very similar to the action we constructed above in Eq. (3.9). However, we must emphasize that here M and K are generic matrices, and that so far we are not putting any constraints on them. Most importantly, now we don't require the graph to support a local vertex-face correspondence. Instead, we will consider generic situation and show that if we want the action to take this form, then the local vertex-face correspondence will arise naturally.

3.9.1 Edge-space, Cut-space and Loop-space

Here we introduce some concepts from the algebra graph theory, [8] that will be used later. In algebraic graph theory, an N_e-dimensional vector represents each edge e of a graph G,

$$\epsilon_e = (0, 0, \ldots, 1, \ldots, 0), \tag{3.40}$$

where the eth component of the vector is 1 and all other components are 0. These vectors form the basis of a N_e-dimensional linear space, which is called the *edge space* of the graph G. It is easy to realize that the K-matrix defined above is a rank-2 tensor in this linear space.

For a directed graph (i.e., a digraph), each (contractible or non-contractible) cycle C can be represented

as an N_e-dimensional vector, ξ_C, whose eth component is

$$\xi_{C,e} = \begin{cases} +1 & e \in C \text{ and } e \text{ is along the direction of } C \\ -1 & e \in C \text{ and } e \text{ is opposite to the direction of } C \\ 0 & e \notin C \end{cases} \tag{3.41}$$

These vectors span a linear space, which is a subspace of the edge space. In algebraic graph theory, this subspace is known as the *circuit-subspace*.

A *cutset* is a set of edges, where if we cut all the edges in a cutset, the graph is cut into two disconnected pieces. A more rigorous definition of a cutset relies on a partition of vertices. If V is the set of all vertices of a graph G, we can separate these vertices into two subset V_1 and V_2, such that $V_1 \cup V_2 = V$ and $V_1 \cap V_2 = 0$. This is called a partition of the set V. For each partition of V, we can define a cutset by collecting all edges of G that have one end in V_1 and the other in V_2. For a digraph, one can choose one of the two possible orientations for a cutset by specifying the vertices in V_1 (or V_2) to be the positive ends, while the other to be negative. If an edge in the cutset points to the positive end of the cutset, it is a positive edge in this cutset. Otherwise, it is a negative edge.

Similar to cycles discussed above, each cutset can also be represented by an N_e-dimensional vector ξ_H, whose eth component is

$$\xi_{H,e} = \begin{cases} +1 & e \in H \text{ and } e \text{ is a positive edge} \\ -1 & e \in H \text{ and } e \text{ is a negative edge} \\ 0 & e \notin H \end{cases} \tag{3.42}$$

The linear space spanned by these vectors is known as the *cut-subspace*, which is also a subspace of the edge space. For a planar graph, each cutset corresponds to a contractible cycle in the dual graph.

In algebraic graph theory, it is shown that the edge space is the direct sum of the circuit-subspace and the cut-subspace. In Appendix B we provide a proof for the planar graphs considered here. This result implies that for the edge space, instead of using the basis shown above in Eq. (3.40), we can choose a new basis for the edge space by selecting a complete basis of the circuit-subspace and a complete basis of the cut-subspace.

For planar graphs, we can use all independent (contractible or noncontractible) cycles to form a basis for the circuit-subspace. For the cut-subspace, all independent contractible cycles in the dual graph forms a complete basis. Therefore, we can span the edge space using these loops. Using this new basis, we can rewrite all tensors defined on the edge space, including the K^{-1} matrix, which will be done in the next

section.

3.9.2 $N_v \geq N_f$

We will now prove that for the K matrix to be nonsingular and the discretized theory to preserve the correct commutation relation of Eq (3.22), the number of faces can never exceed the number of vertices. Using the generic action shown in Eq. (3.39) (remember that K and M are now two arbitrary matrices), we find that for the generic setup, we shall still expect the commutation relation

$$[A_e, A_{e'}] = -\frac{2\pi i}{k} K^{-1}_{e,e'} \tag{3.43}$$

Because singularities in the commutation relations must be avoided, the K matrix must be invertible. In addition, if we consider two cycles (loops) C and C', we shall expect the commutation relation

$$[\mathcal{W}_C, \mathcal{W}_{C'}] = \frac{2\pi i}{k} \nu\,[C, C']\,, \tag{3.44}$$

As shown above, this commutator is a topological invariant and it is one of the key feature of the Chern-Simons gauge theory. Thus, we will require Eq. (3.44) for our discretized theory.

Below, we prove that if we assume the topologically invariant commutation relation, Eq. (3.44), then the K matrix must be singular if $N_v < N_f$. Therefore, we must have $N_v \geq N_f$. We will start from a genus zero surface and then expand the conclusion to other surfaces with nonzero genus.

For the below discussion we only consider graphs defined on a genus zero surface (a sphere). Instead of directly showing that the K matrix is singular for $N_v < N_f$, here we take a different but equivalent approach. We will start by assuming the K matrix is invertible and work with the K^{-1} matrix. Then, using the commutation relation, we will show that the determinant of K^{-1} matrix is zero for $N_v < N_f$, and thus the K matrix is singular.

Using Eqs. (3.43) and (3.44), we know that

$$K^{-1}_{e,e'} \xi_{C,e} \xi_{C',e'} = -\nu\,[C, C'] \tag{3.45}$$

Here, we choose a new basis set for the edge space. Instead of using the vectors shown in Eq. (3.40), we use a set of vectors ξ_i with $i = 1, 2, \ldots, N_e$. For $i = 1, 2, \ldots N_f - 1$, ξ_i are independent cycles, i.e. they form a complete basis of the circuit-subspace. For $i = N_f, N_f + 1, \ldots, N_e$, the corresponding ξ_i are independent cutsets, i.e. they are a complete basis of the cut-subspace. Using this new basis, we can define a $\tilde{K}^{-1}$ matrix

as

$$\tilde{K}^{-1}_{i,j} = K^{-1}_{e,e'} \xi_{i,e} \xi_{j,e'}, \tag{3.46}$$

For i and j smaller than N_f, ξ_i and ξ_j are contractible cycles of the graph (for a planar defined on a closed orientable 2D surface with genus zero, all cycles are contractible). Using Eq. (3.45), it is easy to realize that $\tilde{K}^{-1}_{i,j} = 0$ for i and j smaller than N_f. (As shown above, the number of oriented intersection for contractible loops is always zero). Therefore, we can write the $\tilde{K}^{-1}$ matrix in a block form

$$\tilde{K}^{-1} = \begin{pmatrix} 0 & A \\ -A^T & B \end{pmatrix} \tag{3.47}$$

Here the first block 0 is a $(N_f-1)\times(N_f-1)$ zero matrix and B is a $(N_e-N_f+1)\times(N_e-N_f+1)$ matrix. Using the Euler characteristic $N_v - N_e + N_f = 2 - 2g$, we can rewrite the dimensions of B as $(N_v-1)\times(N_v-1)$, since we have assumed the genus being zero, $g = 0$. The block A has dimension$(N_f-1)\times(N_v-1)$ and A^T is the transpose of A.

For a matrix with a block of zeros as shown in Eq. (3.47), the determinant of the matrix must be zero, if the zero block is larger than the B block (see Appendix Sec. C for a proof). Therefore, if $N_v < N_f$, $\det \tilde{K}^{-1} = 0$. Because ξ_i is a complete basis for the edge space, this implies that $\det K^{-1} = 0$ and thus K is a singular matrix.

For a surface with nonzero genus, the same conclusion can be proved.

3.9.3 Flux attachment and $N_v \leq N_f$

Let us now prove that the flux attachment also requires $N_v \leq N_f$. Flux attachment implies that for each charge distribution, there is a corresponding unique distribution for magnetic fluxes. Because charge can be distributed on N_v sites, to ensure that there is a corresponding flux distribution for every charge configuration, we must have equal number or more faces to put the fluxes.

A more rigorous proof can be formulated by taking a functional derivative to the generic action Eq. (3.39), $\delta S/\delta A_v$, which result in the flux attachment condition

$$q_v = \frac{k}{2\pi} M_{v,f} \Phi_f, \tag{3.48}$$

If we want the flux attached to a charge to be local (i.e. the flux for a point charge occupies only a single

face), for each vertex v, the $M_{v,f}$ is nonzero only for one value of f. As a result, the M matrix defines a mapping from v to f.

This mapping must be injective. Namely, for two different vertices, their corresponding faces must be different. This is so because if two different vertices v and v' are mapped to the same face f, then Eq. (3.48) will require that $q_v = q'_v$, i.e. two different vertices always have the same charge, which is obviously not a physically necessary constraint. Thus, for a injective mapping from vertices to faces, we must have $N_v \leq N_f$.

3.9.4 local vertex-surface correspondence

In the previous two subsections we proved that $N_v \leq N_f$ and $N_v \geq N_f$ must hold simultaneously. Therefore, the graph must have the same numbers of vertices and faces $N_v = N_f$. With $N_v = N_f$, the mapping from vertices to faces discussed above become a one-to-one correspondence between vertices and faces. As addressed in Sec. 3.8, it is important to ensure that this correspondence is local. As a result, the local vertex-face correspondence arises naturally, when we try to ensure the theory being nonsingular and the key properties of the Chern-Simons gauge theory is preserved.

Chapter 4

Magnetization plateaus in XXZ Heisenberg model

In this chapter, I go back to the Kagome lattice and specifically consider the spin-$\frac{1}{2}$ XXZ Heisenberg model in the presence of an external magnetic field introduced in Ch 2. We will utilize the flux attachment transformation developed in Ch 2 and setup the mean-field theory on the Kagome lattice in Sec 4.1. In Sec 4.2 we will then establish the mean-field states that can arise and characterize its properties. Then we will include the effects of fluctuations in 4.3 and derive an effective continuum field theory. We will then show that the resultant continuum Chern-Simons field theory predicts a chiral spin liquid phase. Some of the technical details of the calculations are included in Appendices D and E. A majority of this chapter is also published in [43].

4.1 Mean-field theory

In this section we discuss the physics of the magnetization plateaus of the spin-$\frac{1}{2}$ XXZ quantum Heisenberg antiferromagnet on the Kagome lattice at the mean-field level. As already mentioned above the Chern-Simons term imposes the flux attachment condition $n(x,t) = \theta B(x,t)$. This allows us to re-write the interaction term of the action for the fermions, *c.f.* Eq.(2.3), (originally the $S_z S_z$ term of the Heisenberg Hamiltonian) purely in terms of the Chern-Simons gauge field as follows

$$S_{\rm int}(A_\mu) = \int dt \lambda J \sum_{<x,y>} \left(\frac{1}{2} - \theta B(x,t)\right)\left(\frac{1}{2} - \theta B(y,t)\right) \tag{4.1}$$

As a result of this substitution, the action is now quadratic in fermionic fields and the fermionic degrees of freedom can be integrated out to yield the effective action just in terms of gauge fields. The effective action has the form

$$S_{\rm eff}(A_\mu) = -i{\rm tr}\ln[iD_0 + \mu - h(A)] + S_{\rm int}(A_\mu) + \theta S_{CS}(A_\mu) \tag{4.2}$$

where the hopping Hamiltonian $h(A)$ is (in matrix notation)

$$h(A) = \frac{J}{2} \sum_{\langle x;x' \rangle} \left[e^{iA_j(x,t)} \left| x,t \right\rangle \left\langle x',t \right| + h.c \right] \tag{4.3}$$

and the label $\langle x, x' \rangle$ refers to the nearest neighbors sites x and x' on the Kagome lattice.

The saddle-point equations are obtained by extremizing the action in Eq.(4.2) w.r.t the gauge fields

$$\left. \frac{\delta S_{\text{eff}}(A)}{\delta A_\mu} \right|_{A_\mu = \bar{A}_\mu} = 0 \tag{4.4}$$

Before writing down the expressions for the saddle point equations, we first focus on the fermionic part of the action S_F. Its derivative w.r.t the temporal A_0 component of the gauge field gives

$$\langle n(x,t) \rangle = \left\langle -\frac{\delta S_F}{\delta A_0(x,t)} \right\rangle = -iS(x,t;x,t) \tag{4.5}$$

Similarly, for the spatial A_k component one gets

$$\begin{aligned} \langle j_k(x,t) \rangle =& \left\langle -\frac{\delta S_F}{\delta A_k(x,t)} \right\rangle \\ =& \frac{J}{2} \left[S(x+e_k,t;x,t) e^{i\bar{A}_k(x,t)} - S(x,t;x+e_j,t) e^{-i\bar{A}_k(x,t)} \right] \end{aligned} \tag{4.6}$$

Here, $j_k(x,t)$ is the (gauge-invariant) fermionic current. $S(x,t;x',t')$ is the propagator for the fermions in an average background field $\bar{A}_\mu(x,t)$, and it is the solution of the lattice differential equation

$$\left(i\bar{D}_0 + \mu - h(\bar{A}) \right) S(x,t;x',t') = \delta_{x,x'} \delta(t-t') \tag{4.7}$$

where $h(\bar{A})$ is given in Eq.(4.3).

Hence, the saddle point equation w.r.t $A_0(x)$ field yields the expectation value of the local fermion density

$$\langle n(x) \rangle = \theta \langle B(x) \rangle \tag{4.8}$$

which amounts to imposing the flux attachment constraint on average.

Similarly for the field $A_k(x)$, one gets the mean-field equation for the expectation value of the local fermion current

$$\langle j_k(x,t) \rangle = \theta \left\langle \frac{\delta S_{CS}}{\delta A_k(x,t)} \right\rangle + \left\langle \frac{\delta S_{\text{int}}}{\delta A_k(x,t)} \right\rangle \tag{4.9}$$

The expectation values in Eq.(4.9) are explicitly given by

$$\begin{aligned}\left\langle \frac{\delta S_{CS}^{(1)}}{\delta A_k(x,t)} \right\rangle =& \bar{d}^{k\alpha} \bar{A}_{0\alpha}(x) \\ \left\langle \frac{\delta S_{CS}^{(2)}}{\delta A_k(x,t)} \right\rangle =& \frac{1}{2}(K_{ki} - K_{ik})\partial_0 \bar{A}_i(x) = K_{ki}\partial_0 \bar{A}_i(x)\end{aligned} \tag{4.10}$$

where α is the sub-lattice index and

$$\bar{d}^{k\alpha} = \begin{pmatrix} 1 & 0 & -S_2^{-1} \\ -1 & S_1^{-1} & 0 \\ 1 & -1 & 0 \\ -S_2^{-1} & 1 & 0 \\ S_1^{-1} & 0 & -1 \\ -1 & 0 & 1 \end{pmatrix} \tag{4.11}$$

where S_1 and S_2 are again the shift operators as defined earlier in Section 2.3.

The full form of the saddle point-equation for the A_k fields is quite cumbersome and will not be written down explicitly here. Instead, as we are looking for time-independent/static and uniform solutions, we take the fluxes on any particular sub-lattice to be the same (i.e. $\bar{B}^\alpha(x) = \bar{B}^\alpha(y)$ for any x and y), and the resulting simplified mean-field expression for the mean-field currents is

$$\langle j_k(x) \rangle = \theta \bar{d}^{k\alpha} \bar{A}_{0\alpha}(x) - 2J\lambda\theta^2(-1)^k \left[\bar{B}^a - f_k \bar{B}^c - (1 - f_k)\bar{B}^b\right] \tag{4.12}$$

with $f_k = 1$ when $k = 1, 5, 6$ and $f_k = 0$ when $k = 2, 3, 4$.

4.2 Mean-Field Theory of the magnetization plateaus

4.2.1 XY model

Let us now analyze the XY Heisenberg antiferromagnet ($\lambda = 0$) and its magnetization plateaus at the mean-field level. Setting $\lambda = 0$ gets rid of the $S^z S^z$ components and makes the fermions non-interacting. However, the fermions are still coupled to the Chern-Simons gauge field. Further, the mean-field equation Eq.(4.12) is satisfied by $\bar{A}_{0\alpha} = 0$ in the absence of any currents. This implies that we are just left with the flux attachment condition in Eq.(4.8).

At the mean-field level, we look for uniform flux states i.e. $\bar{B}_a = \bar{B}_b = \bar{B}_c = \phi = 2\pi\frac{p}{q}$ with $p, q \epsilon \mathbb{Z}$. This

makes the total flux through the unit cell (which has three plaquettes) $B_{u.c} = 3\phi = 2\pi\frac{3p}{q}$. By imposing the Chern-Simons constraint on average, we deduce that, for uniform states and taking into account that $\theta = \frac{1}{2\pi}$, the average site occupancy (density) of each sublattice of the unit cell is $\langle n \rangle = \frac{p}{q}$.

Such a state can be realized with the below choice of gauge fields

$$\begin{aligned} A_1(\vec{x}) &= 0 & A_2(\vec{x}) &= \phi & A_3(\vec{x}) &= 0 \\ A_4(\vec{x}) &= 0 & A_5(\vec{x}) &= -\phi + 3\phi x_1 & A_6(\vec{x}) &= 3\phi x_1 \end{aligned} \tag{4.13}$$

with $\vec{x} = (x_1, x_2)$ where x_1 and x_2 are the co-ordinates along the e_1 and e_2 directions respectively in Fig.2.1.

Hofstadter spectrum

The XY model has now been reduced to a problem of non-interacting fermions hopping in a lattice in the presence of a (statistical) magnetic field. This is very similar to the problem of the integer quantum Hall (IQH) effect where the one-particle states possess non-trivial Chern numbers. For a square lattice one can obtain these Chern numbers by solving the resulting Harper equation either numerically or by performing a perturbation theory in the hopping parameters.[71] The final structure is most easily seen in the Hofstadter spectrum as was pointed out by G. Misguich et. al. [53] in their studies on the triangular and Shastry-Sutherland lattices using a similar analysis. By extrapolating the Chern numbers from the case of the square lattice, one can obtain the Chern numbers for the case of the Kagome XY Heisenberg model.

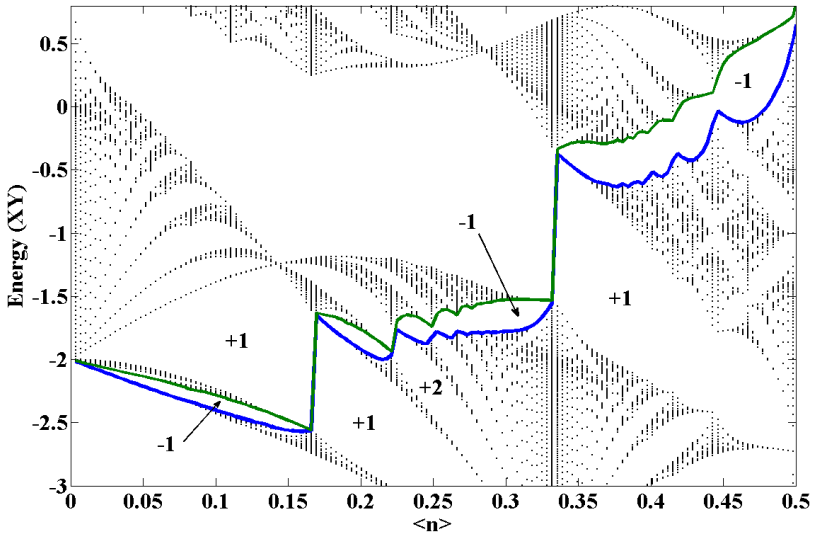

Figure 4.1: Hofstadter spectrum for the XY model as a function of sublattice density $\langle n \rangle$. The numbers shown are the Chern numbers of the respective filled bands. The magnetization plateaus at $\frac{1}{3}, \frac{5}{9}, \frac{2}{3}$ correspond to the three vertical jumps shown in this figure, respectively at densities $\langle n \rangle = \frac{1}{3}, \frac{2}{9}, \frac{1}{6}$.

The results are shown in Fig.4.1 where the x-axis is the average filling/density $\langle n \rangle$ on each sub-lattice and the y-axis are the single-particle energies of the associated free fermion model of the XY model. The bottom solid line indicates the Fermi level for the occupied bands. The top solid line is the next excited energy single-particle state available.

The numbers shown in Fig.4.1 are the Chern numbers of a state with all the below bands completely filled up to that number. In Section 4.3.2 we will see that we have a quantum Hall type incompressible state if the total Chern number of the occupied bands satisfies $C \neq -1$. The discontinuous jumps in the Fermi level in the figure indicate the fillings at which the Chern number $C \neq -1$. These situations are expected to correspond to magnetization plateaus.[53] These jumps occur at site fillings of $\langle n \rangle = \frac{1}{3}, \frac{1}{6}, \frac{2}{9}$, which correspond, respectively, to 2π flux through each unit cell, π flux through each unit cell (and hence 2π flux for two unit cells), and $\frac{4\pi}{3}$ flux per unit cell (or 4π flux in three unit cells). Since

$$\langle n \rangle = \frac{1}{2} - \langle S_z \rangle = \frac{1}{2} - M \tag{4.14}$$

we could find possible magnetization plateaus corresponding to $m = \left| \frac{M}{M_{sat}} \right| = \frac{1}{3}, \frac{2}{3}$ and $\frac{5}{9}$, with $M_{sat} = \frac{1}{2}$. Hence, at the mean-field level all these magnetization states have integer Chern numbers and behave like integer quantum Hall (IQH) states, much in the same way as with the behavior of composite fermions in the theory of the fractional quantum Hall effect.[36, 37, 48] In what follows we will focus primarily on the simplest case of the 1/3 magnetization plateau and comment briefly on the other cases.

4.2.2 XXZ model

Following our discussion in the previous section, we now extend the results to the case of the XXZ model by introducing the λ term ($S^z S^z$) in the Hamiltonian. We begin first by performing the mean-field analysis at the fillings associated with the magnetization plateaus.

Mean-field analysis

At the mean-field level each unit cell satisfies the condition $\langle n \rangle_{u.c} = \langle n_a \rangle + \langle n_b \rangle + \langle n_c \rangle = 1$. This density condition translates to the flux condition $\langle B_a \rangle + \langle B_b \rangle + \langle B_c \rangle = 2\pi$ as a result of the flux attachment constraint in Eq.(4.8). (Fluxes on the lattice are defined modulo 2π.) The B fields are gauge invariant quantities and the above ansatz can be satisfied by the below choice of gauge fields

$$\begin{aligned} \bar{A}_1 = -c_2 \qquad \bar{A}_2 = c_1 \qquad \bar{A}_3 = -c_1 \\ \bar{A}_4 = c_1 \qquad \bar{A}_5 = -c_2 \qquad \bar{A}_6 = c_2 \end{aligned} \tag{4.15}$$

where c_1 and c_2 are some constant parameters that will be determined below and the definitions of the links on the Kagome lattice in Fig.2.1 are used. This makes

$$\bar{B}_a = 2\pi - 3c_1 - 3c_2 \qquad \bar{B}_b = 3c_1 \qquad \bar{B}_c = 3c_2 \tag{4.16}$$

Further, assuming that these ground states states have no currents i.e. $\langle j_k(x,t)\rangle = 0$, the second saddle point equation Eq.(4.12) can be satisfied by the below choice of temporal gauge fields on each of the sublattices

$$\begin{aligned} \bar{A}_0^a &= -2J\lambda\theta\,(2\pi - 3c_1 - 3c_2) \\ \bar{A}_0^b &= 2J\lambda\theta 3c_1 \\ \bar{A}_0^c &= 2J\lambda\theta 3c_2 \end{aligned} \tag{4.17}$$

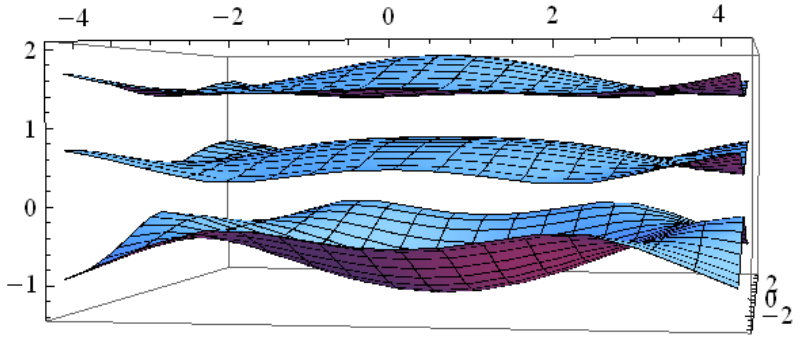

(a) $\lambda = 0$

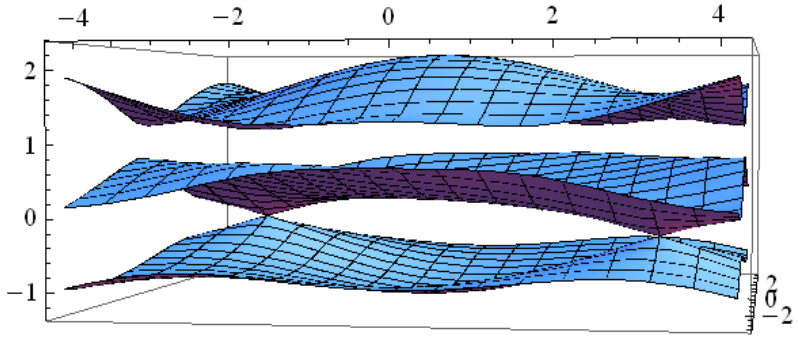

(b) $\lambda = 0.6$

Figure 4.2: The Mean-Field spectrum at $\frac{1}{3}$ filling for $\lambda = 0$ and $\lambda = 0.6$. At $\frac{1}{3}$ filling only the bottom band is filled. The spectrum is gapped for all values of λ except for $\lambda \approx 0.6$ where the bottom band touches the middle band and the Chern numbers of the corresponding bands switch.

Self-consistent solutions

The parameters c_1 and c_2 can be computed (numerically) by demanding that the saddle-point equation Eq.(4.8) is satisfied on each sub-lattice for a given value of the magnetic anisotropy parameter λ, i.e.

$$\langle n_\alpha(x,t)\rangle = -iS_{\alpha,\alpha}(x,t;x,t) \tag{4.18}$$

where α is the sub-lattice index. The expression for the propagator in momentum space is given by

$$S_{\alpha\beta}(x,t;x',t') = \int_{\omega,\vec{k}\epsilon B.Z.} e^{i\omega(t-t')-ik(x-x')} S_{\alpha\beta}(\omega,\vec{k}) \tag{4.19}$$

where

$$S^{-1}_{\alpha\beta}(\omega,\vec{k}) = \begin{pmatrix} \omega-\bar{A}_{0a} & -\frac{J}{2}\left(e^{-i\bar{A}_4-ik_1}+e^{i\bar{A}_1}\right) & -\frac{J}{2}\left(e^{-i\bar{A}_5-ik_2}+e^{i\bar{A}_2}\right) \\ -\frac{J}{2}\left(e^{i\bar{A}_4+ik_1}+e^{-i\bar{A}_1}\right) & \omega-\bar{A}_{0b} & -\frac{J}{2}\left(e^{i\bar{A}_3+ik_1}+e^{-i\bar{A}_6-ik_2}\right) \\ -\frac{J}{2}\left(e^{i\bar{A}_5+ik_2}+e^{-i\bar{A}_2}\right) & -\frac{J}{2}\left(e^{i\bar{A}_6+ik_2}+e^{-i\bar{A}_3-ik_1}\right) & \omega-\bar{A}_{0c} \end{pmatrix} \tag{4.20}$$

The values of c_1 and c_2 that satisfy Eq.(4.18) are listed in table 4.1 for a few different values of λ. For the XY model, $\lambda = 0$, the densities on all the sites are the same (and equal to 1/3). As λ is increased (and the interactions are turned on), the density n_a steadily increases while the density $n_b = n_c$ decreases. For very large anisotropy λ, $n_a \approx 1$ while $n_b = n_b \approx 0$ in this model. Intuitively, in the Ising limit ($\lambda \to \infty$), this corresponds to the spins either pointing strictly up or down as expected. At one-third filling, this translates to two up spins and one down spin on average. The fluxes on each of the plaquettes would then either be 0 or 2π which are equivalent on the lattice. Hence, in the Ising limit, this maps to a problem of fermions hopping on the Kagome lattice with no flux at the mean-field level.

Chern Numbers of the Hofstadter States

The energy spectrum of the mean-field phases has three bands as shown in Fig.4.2 (for two values of anisotropy parameter λ). At $\frac{1}{3}$ filling only the bottom band is filled. This state is gapped for all values of λ except at $\lambda \approx 0.6$ when the bottom two bands cross and the low-energy fermionic states become gapless Dirac fermions.

The Chern number of the bands is given by

$$C = \frac{1}{2\pi}\int_{BZ} d^2k F_{12}(k) \tag{4.21}$$

λ	$c_1 = c_2$	n_a	$n_b = n_c$
0	0.698062	0.3333	0.3333
0.25	0.600673	0.4264	0.2868
0.5	0.450504	0.5698	0.2151
0.6	0.361283	0.655	0.1725
0.75	0.235619	0.775	0.1125
1	0.143257	0.8632	0.0684

Table 4.1: Sublattice occupation numbers n_a, n_b and n_c, and values of the parameters $c_1 = c_2$ for different values of the magnetic anisotropy λ, where $\lambda = 0$ is the XY model and $\lambda \to \infty$ is the Ising model.

where $F_{ij} = \partial_i a_j - \partial_j a_i$ and $a_i = -i \langle\psi| \partial_{k_i} |\psi\rangle$ is the Berry flux. Here $|\psi\rangle$ is the normalized eigenvector of the corresponding single-particle energy band and the integral is over the first Brillouin zone of the Kagome lattice. The Chern numbers of the three bands are shown in table 4.2.

λ	C_{bottom}	C_{middle}	C_{top}
$\lesssim 0.6$	+1	0	-1
$\gtrsim 0.6$	0	+1	-1

Table 4.2: Chern numbers for the bottom, middle and top bands for $\lambda < 0.6$ and $\lambda > 0.6$ at 1/3 filling.

At $\lambda = 0$, the Chern number in table 4.2 matches the result for the Chern number obtained from the Hofstadter spectrum shown in Fig. 4.1 at $\frac{1}{3}$ filling. Hence, once again at the mean-field level and for $\lambda \lesssim 0.6$, the phase is gapped and looks like an integer quantum Hall state with Chern number $C_{bottom} = +1$. The point $\lambda \sim 0.6$ marks a transition point between two different phases, an IQH state and an insulating state, again at the mean-field level.

As we had noted in our introductory section on the Jordan-Wigner transformation, the above analysis is valid for $\theta = \frac{1}{2\pi}$. But we could just as easily have chosen $\theta = -\frac{1}{2\pi}$. For this choice of θ the fluxes on each of the plaquettes pick up a negative sign and the sublattice magnetizations have now the opposite sign. This would yield a mean-field state that is related to the above mean-field state by time-reversal symmetry. Also all the signs of the Chern numbers in Table 4.2 would be flipped. We would still get an integer quantum Hall state but with opposite Chern number $C = -1$.

4.3 Continuum Effective Action for the Magnetization Plateaus

We now turn to study the effects of quantum fluctuations for the magnetization plateaus. From now on we will now focus on the case of $\langle n \rangle = \frac{1}{3}$ filling. In this case the magnetic unit cell is the same as the regular

unit cell of the Kagome lattice making it the simplest case to study analytically. Although the other plateaus require larger magnetic unit cells and make the computation analytically unfeasible, the leading part of the long-distance effective action, i.e. the topological piece, can be computed for all three plateaus.

After performing the Jordan-Wigner transformation one obtains the action given by Eq.(2.2) and Eq.(2.3) which is reproduced here

$$S = \int dt \sum_x \psi^*(x) \left[iD_0 + \mu\right] \psi(x) - \frac{J}{2} \int dt \sum_{\langle x,x' \rangle} \left\{\psi^*(x) e^{iA_j(x)} \psi\left(x + e_j\right) + c.c\right\} + S_{\text{int}} + \theta S_{CS} \tag{4.22}$$

with $D_0 = \partial_0 + iA_0$ and again $< x, x' >$ refers to pairs of nearest neighbor sites of the Kagome lattice. Once again at the mean-field level, the state is described as given by Eq. (4.15), Eq. (4.17) and in Table 4.1. The corresponding mean-field phases were discussed in the previous section 4.2.2. Now, we analyze the effect of fluctuations about this mean-field state.

4.3.1 Fluctuations and the 1/3 plateau

In this subsection, we perform an expansion around the mean-field state of the XY model and of the XXZ model. As was outlined earlier in Section 4.1, the action is quadratic in fermions and can be integrated out to give Eq.(4.2). This allows us to perform an expansion around the mean-field state in powers of the fluctuations of the gauge fields by expressing $A_\mu = \bar{A}_\mu + \delta A_\mu$. Here $\bar{A}_\mu$ correspond to the mean-field values of the gauge fields in Eq.(4.15) and Eq.(4.17). The final action in the terms of the fluctuating components will have the form

$$S_{\text{eff}} = \frac{1}{2} \int d^3x d^3y \delta A_\mu(x) \Pi^{\mu\nu}(x,y) \delta A_\nu(y) + \theta S_{CS} + S_{\text{int}} \tag{4.23}$$

where $\Pi^{\mu\nu}$ is the polarization tensor and δA_μ are the fluctuations of the gauge fields. However, unlike the conventional polarization tensor in $2+1$ dimensions where $\mu = 0, 1, 2$, now the indices μ can take a total of nine possible values corresponding to the three temporal fluctuation components and the six spatial fluctuation components on the unit cell of the Kagome lattice.

One way to reduce these additional degrees of freedom is to express the fluctuating components in terms of slow and fast components as follows

$$\begin{aligned} \delta A_{0a} &= \delta A_{0s} + \delta A_0^{f1} + \delta A_0^{f2} \\ \delta A_{0b} &= \delta A_{0s} - \delta A_0^{f1} + \delta A_0^{f2} \\ \delta A_{0c} &= \delta A_{0s} + \delta A_0^{f1} - \delta A_0^{f2} \end{aligned} \tag{4.24}$$

where the labels a, b, c refer to the sub-lattice indices. The subscript label $0s$ refers to the slow component of

the temporal fluctuations and the superscript labels $f1$ and $f2$ refer to the fast components of the temporal fluctuations. (In the absence of the fast components, this just amounts to replacing the various fluctuations on the sub-lattices with a slowly varying fluctuating component.) This construction will also allow us to treat the slow fluctuations as the more relevant fields.

Similarly for the spatial gauge fields

$$\begin{aligned} \delta A_1 &= \delta A_{1s} + \delta A_1^f \qquad & \delta A_4 &= \delta A_{1s} - \delta A_1^f \\ \delta A_2 &= \delta A_{2s} - \delta A_2^f \qquad & \delta A_5 &= \delta A_{2s} + \delta A_2^f \\ \delta A_3 &= \delta A_{3s} - \delta A_3^f \qquad & \delta A_6 &= \delta A_{3s} + \delta A_3^f \end{aligned} \tag{4.25}$$

where the subscript labels js refer to the slow components and the superscript labels f refer to the fast components again. To simplify the notation, the δ label for fluctuations and the label s for the slow components will be dropped from now on.

The polarization tensor $\Pi^{\mu\nu}$ in Eq.(4.23) is calculated by computing the one loop correction about the mean-field state using the mean-field fermion Green function in Eq.(4.20). This computation will be performed numerically due to the complexity of the energy bands in the mean-field phase. The final action in Eq.(4.23) must also be invariant under local gauge transformations, $A_\mu \to A_\mu + \partial_\mu \Lambda$. This imposes the transversality condition on the polarization tensor, $\partial_\mu^x \Pi_{\mu\nu}(x,y) = 0$ or equivalently, $P^\mu \Pi_{\mu\nu}(P) = 0$ in Fourier space (under $A_\mu(P) \to A_\mu(P) - iP_\mu \lambda(P)$) on the polarization tensor. The transversality condition can be used to simplify the computation to some extent. More explicit details of this calculation are shown in Appendix D.1

4.3.2 Full Continuum Action

Expanding the above action about the mean-field state up to second order in fluctuations gives the below terms

$$S_{\text{final}} = S_{00} + S_{0j} + S_{ij} + \theta S_{CS} + S_{\text{int}} \tag{4.26}$$

where S_{00}, S_{0j} and S_{ij} account for the temporal and spatial components of the polarization tensor. The S_{CS} and S_{int} terms are obtained by taking the continuum limits of the Chern-Simons and interaction terms respectively. In obtaining these terms we make the further simplification that only terms to second order in derivatives are kept for the slowly fluctuating gauge fields. For the fast fluctuating gauge fields, only the leading order non-derivative terms are retained. The explicit expressions for the above terms are quite cumbersome and are saved for Appendix D.1.

As mentioned above S_{final} has many more gauge fields than a usual gauge theory in $2+1$ dimensions. However, the important thing to note is that S_{final} is quadratic and massive in many of the fluctuating gauge fields. This will allow us to integrate out some of these extra fields and reduce the excessive number of gauge fields in this model. More precisely, the action in Eq.(4.26) is quadratic and massive in fields A_0^{f1}, A_0^{f2}, $A_1^f + A_2^f - A_3^f$ and A_3. In order to safely integrate out these fields, the mass terms have to have the correct sign i.e. the masses of the temporal fields must be positive and the masses of the spatial gauge fields must be negative. These conditions have been verified numerically for different values of λ. Once, these extra fields have been integrated out, we are just left with the traditional three fields A_0, A_x and A_y (after re-expressing the remaining fields along the x and y directions). (Recall that the above fields correspond to the fluctuating components and that we dropped the δ label to simplify the notation.)

The long-distance behavior of the final effective action can be more succinctly expressed as

$$\begin{aligned} S_{\text{eff}} =& S_{CS}^{\text{eff}} + S_M^{\text{eff}} + \dots \\ S_{CS}^{\text{eff}} =& \int d^3x \frac{1}{2} \left(\theta + \theta_F\right) \epsilon_{\mu\nu\lambda} A_\mu \partial_\nu A_\lambda \\ S_M^{\text{eff}} =& \int d^3x \left[\frac{1}{2}\epsilon \boldsymbol{E}^2 - \frac{1}{2}\chi B^2\right] \end{aligned} \tag{4.27}$$

where S_M^{eff} donates the Maxwell action with coefficients $\epsilon > 0$ and $\chi > 0$. $\boldsymbol{E}$ and B are, respectively, the effective "electric" and "magnetic" fields of the statistical gauge field A_μ.

The effective Chern-Simons parameter for the XY and Ising regimes are given in Table 4.3. In Eq.(4.27), the labels μ, ν now only take values $0, x, y$. To lowest order the most important term is just the effective Chern-Simons term S_{CS}^{eff} as it has the least number of derivatives. For $\lambda \lesssim 0.6$, the Chern-Simons term obtained by integrating out the fermions and the original Chern-Simons term obtained from the Jordan-Wigner transformation add where as, for $\lambda \gtrsim 0.6$, we are just left with the original Chern-Simons term.

λ	$\theta + \theta_F$
$\lesssim 0.6$	$\frac{1}{2\pi} + \frac{1}{2\pi}$
$\gtrsim 0.6$	$\frac{1}{2\pi} + 0$

Table 4.3: Effective Chern-Simons parameter for the XXZ model in the XY and Ising regimes.

The results of the above computation can be divided into two regimes.

4.3.3 XY regime

In the XY-regime i.e. for $\lambda \lesssim 0.6$, the Chern-Simons terms add. The final low energy action (just keeping the Chern-Simons part) has the form[25, 86]

$$S_{\text{eff}}^{CS}(A_\mu) = \frac{1}{2}\left(\theta_F + \theta\right) S_{CS}(A_\mu) \tag{4.28}$$

Here θ_F is the coefficient of the induced Chern-Simons term obtained by integrating out the fermionic degrees of freedom and it is given by

$$\theta_F = \frac{C}{2\pi} \tag{4.29}$$

and is the effective Hall conductivity of the mean field state. Here C is the total Chern number of the occupied bands of the mean field theory.

In Eq.(4.28) we have neglected terms in the effective action with more than one derivatives since they are irrelevant at long distances. As it is apparent from Eq.(4.28),[25, 86] the physics of the full system (beyond mean field theory) depends on whether $\theta+\theta_F$ vanishes or not. In particular we will have a gapped state (with broken time reversal invariance) only if $\theta + \theta_F \neq 0$. Otherwise, if $\theta + \theta_F = 0$, the Maxwell-type subleading terms control the low energy physics. In this case the system has a gapless excitation, a "photon", which is equivalent to a Goldstone boson of the antiferromagnet. (For a detailed discussion see Ref.[[26]].) Since we are working with $\theta = \frac{1}{2\pi}$, a gapless state will occur whenever $C = -1$.

The response of this system to an external field can be measured by introducing a small external gauge field $\widetilde{A}_\mu$. [48] In a FQH system this field is an external electromagnetic perturbation which induces a charge current. However, in the case of the antiferromagnet it is a field that induces an spin current of the form

$$J_s(\boldsymbol{r}, \boldsymbol{r}') = i(S_x(\boldsymbol{r})S_y(\boldsymbol{r}') - S_y(\boldsymbol{r})S_x(\boldsymbol{r}')) \tag{4.30}$$

at the link $(\boldsymbol{x}, \boldsymbol{x}')$ of the Kagome lattice. This field $\widetilde{A}_\mu$ couples to the fermionic degrees of freedom in the same way as the statistical gauge fields A_μ. In the presence of this perturbation the effective action becomes

$$S_{\text{eff}}^{CS}(A_\mu, \widetilde{A}_\mu) = \frac{1}{2}\left(\theta_F S_{CS}(A_\mu + \widetilde{A}_\mu) + \theta S_{CS}(A_\mu)\right) \tag{4.31}$$

where again we have assumed that $\theta + \theta_F \neq 0$ and thus the Maxwell-type subleading terms can be safely ignored at low energies.

The actual response of the system to this perturbation is obtained by integrating out the statistical gauge

fields. This gives

$$S^{CS}_{\rm eff}(\widetilde{A}_\mu) = \frac{1}{2}\theta_{\rm eff} S_{CS}(\widetilde{A}_\mu) \tag{4.32}$$

where $\theta_{\rm eff}$ is given by

$$\frac{1}{\theta_{\rm eff}} = \frac{1}{\theta} + \frac{1}{\theta_F} \tag{4.33}$$

This result yields a spin Hall conductance σ^s_{xy} of

$$\sigma^s_{xy} = \frac{\theta_{\rm eff}}{2} \tag{4.34}$$

Following the results for the continuum effective action, we now consider the consequences for the different plateaus which are also summarized in Table 4.4.

The $\frac{1}{3}$ magnetization plateau

Since $\theta = \frac{1}{2\pi}$ and at the $\frac{1}{3}$ plateau we found $\theta_F = \frac{1}{2\pi}$ (from Table 4.3), this implies that $\theta_{\rm eff} = \frac{1}{2}\frac{1}{2\pi}$. Hence at the $\frac{1}{3}$ magnetization plateau Kagome antiferromagnet has a *fractional spin Hall conductivity*

$$\sigma^s_{xy} = \frac{1}{2}\frac{1}{2\pi} \tag{4.35}$$

Hence, the fluctuation effects tell us that the ground state of the Kagome antiferromagnet in the XY regime at $\frac{1}{3}$-filling resembles a $\nu = 1/2$ Laughlin fractional quantum Hall state for (hard-core) bosons. In fact, an alternative description of the state that used the hydrodynamic theory[77] shows that the effective field theory of this state is a level $k = 2$ Chern-Simons gauge theory. The upshot of this analysis is then that the ground state of the Kagome spin-1/2 Heisenberg antiferromagnet at its magnetization plateau at $\frac{1}{3}$ is a topological fluid with a (spin) Hall conductivity of $\frac{1}{2}\frac{1}{2\pi}$, a *two-fold degenerate ground state* on a torus, *a single chiral edge state* (with compactification radius $\sqrt{2}$) on a disk, and excitations are semions with statistical angle $\pi/2$. The same results apply to the equivalent magnetization plateau at $\frac{2}{3}$.

The magnetization plateau at $\frac{5}{9}$

By extending this analysis to the magnetization plateau at $\frac{5}{9}$, we obtain the results summarized in Table 4.4. The $\frac{5}{9}$ plateau has mean-field Chern number $C = 2$, and hence it is equivalent to the first FQH daughter Jain state for bosons in the $\frac{1}{2}$ FQH bosonic Laughlin state. From standard results of the theory of the FQH states,[77] we can then predict that the $\frac{5}{9}$ plateau has *two chiral edge states* on a disk and a *three-fold degenerate ground state* on the torus. In this case, the Hall spin conductivity is $\sigma^s_{xy} = \frac{2}{3}\frac{1}{2\pi}$ and the

excitations are anyons with statistical angle $\pi/3$.

$\langle n \rangle$	m	$2\pi\theta_F$	σ_{xy}	δ
$\frac{1}{6}$	$\frac{2}{3}$	$+1$	$\frac{1}{2}$	$\frac{\pi}{2}$
$\frac{2}{9}$	$\frac{5}{9}$	$+2$	$\frac{2}{3}$	$\frac{\pi}{3}$
$\frac{1}{3}$	$\frac{1}{3}$	$+1$	$\frac{1}{2}$	$\frac{\pi}{2}$

Table 4.4: Summary of results for the magnetization plateaus of the XY model at 1/3, 5/9 and 2/3.

Other fillings

At all other fillings, the expected value of θ_F is $\theta_F = -\frac{1}{2\pi}$. In these regions the pre-factor of the effective Chern-Simons term in Eq.(4.28) exactly cancels out, i.e. $\theta + \theta_F = \frac{1}{2\pi}(1 + (-1)) = 0$, leaving just the Maxwell term in Eq.(4.27) as the leading term. In this case, the elementary excitation is not a vortex but a "photon". However, in $2 + 1$ dimensions there is only one possible polarization state for a photon and this problem then turns out to be equivalent to a system with a Goldstone boson. In other words, away from the plateaus the transverse excitations are Goldstone modes of the spontaneously broken residual $U(1)$ symmetry. This is also the behavior that one expects in the low density (low filling $\langle n \rangle \to 0$) regime when the lattice is sparsely filled and frustration effects are minimal.

Finally we consider the implications if we had chosen $\theta = -\frac{1}{2\pi}$, instead, in our original Jordan-Wigner transformation. As noted in the introduction as well as in our discussion on the mean-field physics, flipping the sign of θ breaks the time-reversal symmetry in the opposite manner and yields a new set of degenerate states. Again, at the mean-field level this gave rise to an integer quantum Hall state with the opposite Chern number $C = -1$. When the effect of fluctuations are taken into about, this now corresponds to an effective Chern-Simons term with $\theta + \theta_F = -\frac{1}{\pi}$. This again describes a fractional quantum Hall state for bosons but with opposite spin Hall conductivity $\sigma^s_{xy} = -\frac{1}{2}$.

4.3.4 Ising regime

In the Ising regime ($\lambda \gtrsim 0.6$), $\theta_F = 0$. Hence, the effective Chern-Simons theory just has the parameter θ from the Jordan-Winger transformation and the statistical angle is simply $\delta = \pi$. This effectively transmutes the fermions back to the bosons that we began with. A similar analysis has been performed in the case of the square lattice by López et. al. [49] and they obtained a similar result in the Ising regime. The square lattice is unfrustrated and the spins behaving like bosons leads to the familiar Néel state on the square lattice in the Ising regime. However, the Kagome lattice is still frustrated in the Ising limit and our analysis does not

choose a specific configuration. An analysis of quantum order by disorder is the needed. There is a lot of numerical evidence that indicates that in the Ising regime, the Kagome lattice favors a VBC type state with a much larger unit cell (based on a $\sqrt{3} \times \sqrt{3}$ structure),[9, 10, 59] and possibly a $\mathbb{Z}_2$ time-reversal-invariant topological phase in between as in the simpler Ising systems.[55]

4.4 Spin correlations in the Magnetization Plateaus

4.4.1 $S^z S^z$ correlations

The fluctuating component of the $\langle S^z S^z \rangle$ correlation can be computed by expressing them in terms of the magnetic fields as follows

$$\langle S^z(x) S^z(y) \rangle = \frac{1}{4} + \theta^2 \langle B(x) B(y) \rangle \tag{4.36}$$

This calculation can be performed by introducing the usual source term j_μ coupled to a Chern-Simons term. The details are presented in Appendix E.1. The Fourier transform of the connected $S^z S^z$ spin correlation, which we denote by $f^{zz}(p)$, can be expressed as follows

$$f^{zz}(p) = i\theta^2 \Big(p_1^2 G_{22}(p) - p_1 p_2 G_{12}(p) - p_1 p_2 G_{21}(p) + p_2^2 G_{11}(p) \Big) \tag{4.37}$$

where $G_{\mu\nu}(p)$ is the Fourier transform of the propagator of the gauge field of the continuum action given in Eq.(4.27). This propagator can easily be computed by introducing a usual gauge fixing term. In the Lorentz gauge $\partial^\mu A_\mu = 0$. This yields the following expectation value in the low energy and long wavelength limit

$$f^{zz}(p) = \theta^2 \frac{\epsilon \boldsymbol{p}^2}{\epsilon^2 \omega^2 - \epsilon \chi \boldsymbol{p}^2 - (\theta + \theta_F)^2 + i\eta} \tag{4.38}$$

where $\boldsymbol{p}^2 = p_1^2 + p_2^2$, and as usual we must take the limit $\eta \to 0^+$. Hence, in the magnetization plateaus the longitudinal spin susceptibility has a Lorentzian shape centered at zero momentum with a width determined by the energy gap $\sim (\theta + \theta_F)/\epsilon$.

For the case of the $m = \frac{1}{3}$ plateau $\theta + \theta_F = \frac{1}{\pi}$ and the collective modes are gapped. At all other fillings on the Kagome lattice that do not correspond to these plateau type states or for the case of the square lattice where $\theta + \theta_F = 0$, the collective modes would be gapless and correspond to Goldstone modes of the transverse fluctuations.

4.4.2 XY correlations

These components can be expressed as

$$S^x(x)S^x(y) + S^y(x)S^y(y) = \frac{1}{2}\left(S^+(x)S^-(y) + S^+(y)S^-(x)\right) \tag{4.39}$$

Hence, the computation of the above expectation value boils down to a computation of $\langle S^+(x)S^-(y)\rangle$. From the Jordan-Wigner transformation, we know that this can be expressed in the continuum as (plus its Hermitian conjugate which is not written down explicitly)

$$\begin{aligned} S^{XY}_\Gamma(x,y) =& \langle S^+(x)S^-(y)\rangle \\ =& \langle \psi^\dagger(x) e^{i\int_{\Gamma(x,y)} A_\mu dx^\mu} \psi(y)\rangle \\ =& \langle G_F(x,y;A_\mu) e^{i\int_{\Gamma(x,y)} A_\mu dx^\mu}\rangle_{A_\mu} \end{aligned} \tag{4.40}$$

where $G_F(x,y;A_\mu)$ is the fermion propagator in the presence of the statistical gauge field A_μ. In the second step we have just averaged over the fermionic degrees of freedom. This gives rise to the expectation of the operator in the last step where the average is just over the statistical gauge fields A_μ.

This expectation is quite difficult to compute in general due to the non-local string along the path $\Gamma(x,y)$ that connects points x and y. To simplify the above expression, the fermionic propagator can be expressed in terms of a Feynman path integral as a sum over histories of the particles. At a semi-classical level the above integral can then be expressed in terms of smooth trajectories which are the dominant contributions for a problem with an energy gap and in the long-distance limit. The below simplifications also rely on the fact that the photon propagator is massive as in the case of the $m = \frac{1}{3}$ plateau. If this were not the case the below results would be drastically altered. The details of this calculation are shown in Appendix E.2.

Finally, the above correlation can be approximated as

$$S^{XY}_\Gamma(x,y) \simeq \sum_\gamma (\text{Amp})_\gamma e^{I_1+I_2} \tag{4.41}$$

where the $(\text{Amp})_\gamma$ is the weight associated with a smooth trajectory γ. The set of paths $\{\gamma\}$ are closed curves which are the oriented sum of the paths Γ and its histories.

The first integral I_1 in the exponent is proportional to the length of the path associated with the curve γ and is given by

$$I_1 = -\frac{\epsilon}{2(\theta+\theta_F)^2} L(\gamma) \tag{4.42}$$

where $L(\gamma)$ is the perimeter of the path γ.

The second integral I_2 can be expressed as

$$I_2 \approx \frac{i}{2\bar{\theta}} \frac{\Phi_\gamma}{\phi_0} = \frac{i}{2}\Phi_\gamma \tag{4.43}$$

where Φ_γ is the average flux over the path γ. Hence, the term e^{I_2} corresponds to an Aharonov-Bohm phase associated with the path γ. In the last step, we have used the fact that $\bar{\theta} = \theta + \theta_F = \frac{1}{\pi}$ and the flux quantum $\phi_0 = 2\pi$.

If one chooses the path γ to correspond to the shortest path between the points x and y (i.e. the path that minimizes the classical equations of motion), then the expectation can be further simplified as

$$S_\Gamma^{XY}(x,y) \simeq \sum_{s.p} (\text{Amp})_{s.p.} exp\left\{ -\frac{\epsilon}{2\bar{\theta}^2} L_{s.p.} + \frac{i}{2}\Phi_{s.p.} \right\} \tag{4.44}$$

where $s.p.$ correspond to the classically shortest paths and $\bar{\theta} = \theta + \theta_F$ again.

Case 1: In this first case, the trajectory of the classically shortest path does not enclose any loops. As an example one could consider measuring this XY correlation between a point x and another point along e_1 direction of the lattice (in Fig.2.1) at say $x + d_x$. In this case there is just one classical path corresponding to the straight line between points x and y and the area of the loop associated with the Aharonov-Bohm phase would reduce to zero. In this case, the above correlation would simply reduce to

$$S_\Gamma^{XY}(x, x+d_x) \approx e^{-\epsilon\pi^2 d_x} \tag{4.45}$$

i.e. just exponentially decaying in the distance between the two points.

Case 2: In the second case, the classical trajectory can enclose some number of hexagons leading to an Aharonov-Bohm phase factor. For instance, let us consider the correlation between the point x and another point, say, along the $e_1 + e_2$ direction of the lattice in Fig.2.1. This would correspond to points along the diagonal of the hexagons. Classically there are four paths/ways to reach the point across the diagonal of the hexagon, two of which lead to a phase of $\Phi_{\text{hex}} = \frac{2\pi}{3}$ (in the XY limit). Hence, the XY correlation picks up an additional phase of $(2 + 2e^{i\frac{2\pi}{3}})$ for each hexagon that the classical trajectory encounters. More generally,

for a path that encloses a certain number n of hexagons and the generic result would be

$$S_{\Gamma}^{XY}(x,y) \simeq 2^n(1+e^{i\frac{2\pi}{3}})^n e^{-\epsilon\pi^2 d_{(x,y)}}$$
$$S_{\Gamma}^{XY}(x,y) \simeq 2^n e^{in\frac{\pi}{3}} e^{-\epsilon\pi^2 d_{(x,y)}} \tag{4.46}$$

where $d_{(x,y)}$ is the distance along a classical trajectory from x to y and then back. Here there are several different Aharonov-Bohm phases that can arise depending on the number of hexagons encircled by a classical trajectory (The distinct values would correspond to $n = 0, ..., 5$).

Chapter 5

Magnetization plateaus in the presence of other terms

In this chapter we investigate the occurrence of chiral spin liquid states in the presence of three other terms in addition to the XXZ Heisenberg antiferromagnet on the kagome lattice: a) by adding the chiral operator acting on the triangles of this lattice, b) by considering the effects of a Dzyaloshinskii-Moriya interaction, and c) by adding a ring-exchange term on the bowties of the kagome lattice. We will first show that the flux attachment transformation can also be applied to a chiral term, a Dzyaloshinskii-Moriya term or a bowtie term. The chiral and Dzyaloshinskii-Moriya terms explicitly break the time reversal invariance (similar to the external magnetic field in Ch 4). We will show that both these terms also give rise to chiral spin liquids with spin Hall conductance of $\sigma^s_{xy} = \frac{1}{2}$. The final term is equivalent to the product of two chiral operators of the two triangles on the bowtie and does not break time-reversal invariance explicitly. Such a term allows us to investigate the possibility of a spontaneous breaking of time-reversal symmetry.

5.1 XXZ Heisenberg model with a chirality breaking field

Next, we will consider the effects of adding a chirality breaking term to the Heisenberg Hamiltonian in Eq.(2.1). A system of spin-1/2 degrees of freedom on the kagome lattice with a chirality breaking term as its Hamiltonian was considered recently by Bauer and coworkers.[6] Using finite-size diagonalizations and DMRG calculations, combined with analytic arguments, these authors showed that the ground state of this system with an explicitly broken time-reversal invariance is a topological fluid in the universality class of the Laughlin state for bosons at level 2 (or, equivalently, filling fraction 1/2). Here we will examine this problem (including the XXZ Hamiltonian) and find that the ground state has indeed the same universal features found by Bauer and coworkers, and by us in the 1/3 plateau.[43]

The resultant Hamiltonian is given as

$$H_{\rm tot} = H_{XXZ} + H_{\rm ch} - h_{\rm ext} \sum_i S^z_i \tag{5.1}$$

where H_{XXZ} is the XXZ Heisenberg Hamiltonian in (2.1). The chirality breaking term is given by

$$H_{\rm ch} = h \sum_{\triangle} \chi_{ijk}(\triangle) = h \sum_{\triangle} \boldsymbol{S}_i \cdot (\boldsymbol{S}_j \times \boldsymbol{S}_k) \tag{5.2}$$

where $\chi_{ijk}(\triangle)$ is the chirality of the three spins on each of the triangular plaquettes of the kagome lattice and the sum runs over all the triangles of the kagome lattice. Recall the important fact that each unit cell of the of the kagome lattice contains two triangles.

In order to use the flux attachment transformation, it is convenient to express the spin operators S^x and S^y in terms of the raising and lowering S^+ and S^-. As an example, one can re-write the chirality term on a triangular plaquette associated with site b (shown in Fig 2.1) as follows

$$\begin{aligned} \chi_b =& \boldsymbol{S}_a \cdot (\boldsymbol{S}_c \times \boldsymbol{S}_b) \\ =& \frac{i}{2} \Big\{ - S^-_a S^+_c S^z_b + S^+_a S^-_c S^z_b + S^-_a S^z_c S^+_b - S^+_a S^z_c S^-_b - S^z_a S^-_c S^+_b + S^z_a S^+_c S^-_b \Big\} \end{aligned} \tag{5.3}$$

where the subscripts a, b and c label the three corners of a triangular plaquette in Fig 2.1.

The raising and lowering spin operators $S^{\pm}$ are interpreted as the creation and destruction operators for bosons with hard cores, and S^z operators are simply related to the occupation number n of the bosons by $S^z = \frac{1}{2} - n$. Under the flux attachment transformation, the hard core bosons are mapped onto a system of fermions coupled to Chern-Simons gauge fields (residing on the links of the kagome lattice). The boson occupation number at a given site is mapped (as an operator identity) onto the gauge flux in the adjoining plaquette (in units of 2π).

It is the straightforward to see that the chirality term gets mapped onto an additional hopping term on the links of the kagome lattice which carries a gauge as an extra phase factor on each link determined by the fermion density on the opposite site of the triangle. As a result, only the fermionic hopping part of the action in Eq.(2.2) gets modified, and the interaction part and the Chern-Simons part are unaffected.

Putting things together we get an effective fermionic hopping part that has the form

$$S_F(\psi, \psi^*, A_\mu) = \int_t \sum_{\boldsymbol{x}} \Big\{ \psi^*(x) \left(iD_0 + \mu\right) \psi(x) - \sum_{\langle \vec{x}, \vec{x}' \rangle} \overline{J}(x_{(a)}) \left(e^{-i\phi(x_{(a)})} \psi^*(x) e^{iA_j(x)} \psi(x') + h.c \right) \Big\} \tag{5.4}$$

where once again x and x' are nearest neighbor sites and $x_{(a)}$ refers to third site on the triangle formed by sites x and x'. The subscript (a) refers to the sub-lattice label. The expressions of $\overline{J}$ and ϕ on each

sub-lattice can be written as

$$\begin{aligned}\overline{J}_{(a)}(x) =& \frac{1}{2}\sqrt{J^2 + h^2\left(\frac{1}{2} - n_{(a)}(x)\right)^2} \\ \phi_{(a)}(x) =& \tan^{-1}\left[\frac{h}{J}\left(\frac{1}{2} - n_{(a)}(x)\right)\right]\end{aligned} \tag{5.5}$$

Hence, we have expressed the effects of the chirality term in terms of a modified hopping strength $\overline{J}_{(a)}$ and an additional gauge field ($\phi_{(a)}(x)$) on each of the links of the lattice. In the limit that $h = 0$, we just have the original gauge fields and in the other limit with $J = 0$ each link has an additional contribution of ($\phi_{(a)}(x) = \pm\frac{\pi}{2}$).

5.2 Mean-field theory

In this section, we will set up the mean-field expressions for the fermionic action in Eq.(2.2) and Eq.(5.4). The basic setup here is very similar to the situation described in our earlier work,[43] but it has been modified to account for the addition of the chirality term in this paper.

Using the flux attachment constraint imposed by the Chern-Simons term ($n(x) = \theta B(x)$), the interaction term in Eq.(2.2) can now be re-written as follows

$$L_{\text{int}}(A_\mu) = \lambda J \sum_{\langle \vec{x}, \vec{x}' \rangle} \left(\frac{1}{2} - \theta B(x)\right)\left(\frac{1}{2} - \theta B(x')\right) \tag{5.6}$$

The interaction term has been expressed purely in terms of gauge fields. Hence, the resultant action after the flux attachment transformation is quadratic in the fermionic fields. Integrating out the fermionic degrees of freedom gives rise to the below effective action just in terms of the gauge fields

$$S_{\text{eff}}(A_\mu) = -i\text{tr}\ln[iD_0 + \mu - H_{\text{hop}}(A)] + S_{\text{int}}(A_\mu) + \theta S_{CS}(A_\mu) \tag{5.7}$$

where the hopping Hamiltonian $H_{\text{hop}}(A)$ is (in matrix notation)

$$H_{\text{hop}} = \sum_{\langle \vec{x}, \vec{x}' \rangle} \left\{\overline{J}_{(a)} e^{iA_j(x) - i\phi_{(a)}} \left|x\right\rangle \left\langle x'\right| + h.c\right\} \tag{5.8}$$

where the above sum runs over all nearest neighbors $\vec{x}$ and $\vec{x}'$. The gauge field $A_j(x)$ refers to the hopping term required to go from point $\vec{x}$ to $\vec{x}'$ on the lattice. The term $\overline{J}_{(a)}$ and $\phi_{(a)}$ are as defined in Eq.(5.5) with (a) once again referring to the sub-lattice index. In the above expression (a) would correspond to the third site in the triangle formed by nearest-neighbor sites $\vec{x}$ and $\vec{x}'$.

Now the mean-field equations can be obtained by extremizing the action in Eq.(5.7) w.r.t. the gauge fields

$$\left.\frac{\delta S_{\text{eff}}(A)}{\delta A_\mu}\right|_{A_\mu=\bar{A}_\mu} = 0 \tag{5.9}$$

Differentiation with respect to the time components A_0 yields the usual equation relating the density to the flux,

$$\langle n(x)\rangle = \frac{1}{2\pi}\langle B(x)\rangle \tag{5.10}$$

which implies that the flux attachment is now enforced at the mean-field level. The average density can be expressed in terms of the mean-field propagator by

$$\langle n(x,t)\rangle = \left\langle -\frac{\delta S_F}{\delta A_0(x,t)}\right\rangle = -iS(x,t;x,t) \tag{5.11}$$

where S_F refers to just the fermionic part of the action (i.e. the hopping part) and $S(x,t;x',t')$ is the fermion propagator in an average background field $\bar{A}_\mu(x,t)$.

Differentiation with respect to the spatial A_k components yields an expression for the local currents,

$$\langle j_k(x,t)\rangle = \theta\left\langle \frac{\delta S_{CS}}{\delta A_k(x,t)}\right\rangle + \left\langle \frac{\delta S_{\text{int}}}{\delta A_k(x,t)}\right\rangle \tag{5.12}$$

Here too, we can express the average current in terms of the fermionic action in the usual manner

$$\langle j_k(x,t)\rangle = \left\langle -\frac{\delta S_F}{\delta A_k(x,t)}\right\rangle \tag{5.13}$$

We will look for uniform and time-independent solutions af these equations. Under these conditions the mean-field equations for the currents, Eq.(5.12), becomes

$$\langle j_k(x)\rangle = \theta\bar{d}^{k\alpha}\bar{A}_{0\alpha}(x) - 2J\lambda\theta^2(-1)^k\left[\bar{B}^a - f_k\bar{B}^c - (1-f_k)\bar{B}^b\right] \tag{5.14}$$

with $f_k = 1$ when $k = 1,5,6$ and $f_k = 0$ when $k = 2,3,4$. In the above expression, we have also fixed the average fluxes on each sub-lattice (i.e. the fluxes on all sub-lattices of a particular type are the same), α is

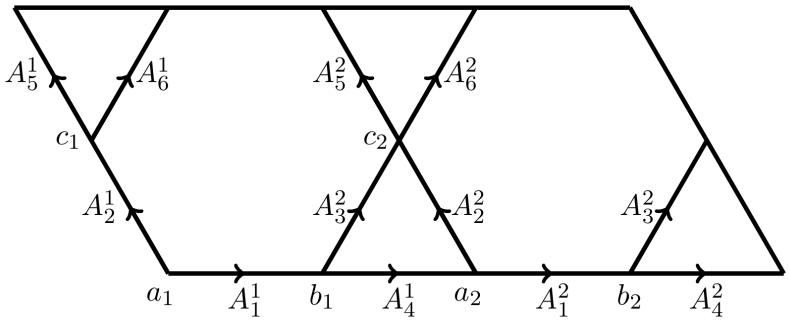

Figure 5.1: Magnetic unit cell at half filling. a, b and c label the different sub-lattices in each of the unit cells. The gauge fields now have an additional label to indicate the unit-cell they belong to.

the sub-lattice index, and

$$\bar{d}^{k\alpha} = \begin{pmatrix} 1 & 0 & -s_2^{-1} \\ -1 & s_1^{-1} & 0 \\ 1 & -1 & 0 \\ -s_2^{-1} & 1 & 0 \\ s_1^{-1} & 0 & -1 \\ -1 & 0 & 1 \end{pmatrix} \tag{5.15}$$

where s_1 and s_2 are the same shift operators on the Kagome lattice.

5.2.1 Mean-field ansatz for XXZ model

We will begin by studying the case with of the XXZ Heisenberg model i.e. we set to zero both the chirality coupling h and the external magnetic field, h_{ext}. This translates to the case of half-filling in the fermionic language. At $\frac{1}{2}$ filling, the average density within each unit cell is given by

$$\frac{1}{3}\left(\langle n_a\rangle + \langle n_b\rangle + \langle n_c\rangle\right) = \frac{1}{2} \tag{5.16}$$

where a, b and c refer to the three sublattices. This gives an average flux of π in each unit cell which implies that the magnetic unit cell consists of two unit cells as shown in Fig 5.1.

In the absence of the chirality term we will primarily look for mean-field phases that are uniform and time-independent, and have zero currents, i.e. $\langle j_k(x,t)\rangle = 0$ in Eq.(5.10) and Eq.(5.14). The flux attachment

condition can be imposed as follows on each of the sub-lattices

$$\begin{aligned}\langle n_a(x)\rangle =&\theta\langle B_a(x)\rangle = \frac{1}{2} - \Delta_1 - \Delta_2 \\ \langle n_b(x)\rangle =&\theta\langle B_b(x)\rangle = \frac{1}{2} + \Delta_1 \\ \langle n_c(x)\rangle =&\theta\langle B_c(x)\rangle = \frac{1}{2} + \Delta_2\end{aligned} \tag{5.17}$$

where Δ_1 and Δ_2 are two parameters that will be chosen to satisfy the mean-field self-consistency equations. The fluxes in Eq.(5.17) can be achieved by the below choice of gauge fields in Fig 5.1

$$\begin{aligned} A_1^1 &= 0 & A_1^2 &= 0 \\ A_2^1 &= p_1 & A_2^2 &= p_1 \\ A_3^1 &= 0 & A_3^2 &= 0 \\ A_4^1 &= 0 & A_4^2 &= 0 \\ A_5^1 &= -p_2 & A_5^2 &= -p_2 + 3\pi \\ A_6^1 &= 0 & A_6^2 &= 3\pi \end{aligned} \tag{5.18}$$

where $p_1 = \pi + 2\pi\Delta_1$ and $p_2 = \pi + 2\pi\Delta_2$.

With these expressions for the densities, the mean-field equation (Eq.(5.14)) can be satisfied by the below choices for the temporal gauge fields

$$A_{0,a} = 2\lambda(\Delta_1 + \Delta_2) \quad A_{0,b} = -2\lambda\Delta_1 \quad A_{0,c} = -2\lambda\Delta_2 \tag{5.19}$$

Using this mean-field field setup, we find two regimes at the mean-field level.

XY regime

In the XY regime, $\frac{\lambda}{J} \lesssim 1$, we find that $\Delta_1 = \Delta_2 = 0$ is the only solution that satisfies the self-consistency condition. This leads to a state with a flux of π in each of the plaquettes. We will represent this as the $(\langle B_a\rangle, \langle B_b\rangle, \langle B_c\rangle) = (\pi, \pi, \pi)$ flux state. This state has a total of six bands, shown in Fig. 5.2 (the top two bands are double degenerate). At half-filling the bottom three bands are filled giving rise to two Dirac points in the spectrum, crossed by the dotted line in Fig.5.2 which indicates the Fermi level. See Sec.5.3 for details.

At the mean-field level this spectrum is equivalent to the gapless $U(1)$ Dirac spin liquid state that has been discussed in previous works.[64, 34] We notice, however, that there are other works that favor symmetry

breaking states but with a doubled unit cell and a flux of π in each of the plaquettes [14]. The state we find could survive when fluctuations are considered giving rise to one of the above states. Alternatively, fluctuations could also open up a gap in the spectrum leading to an entirely different phase. In this paper, we will only analyze the gapless states at a mean-field level.

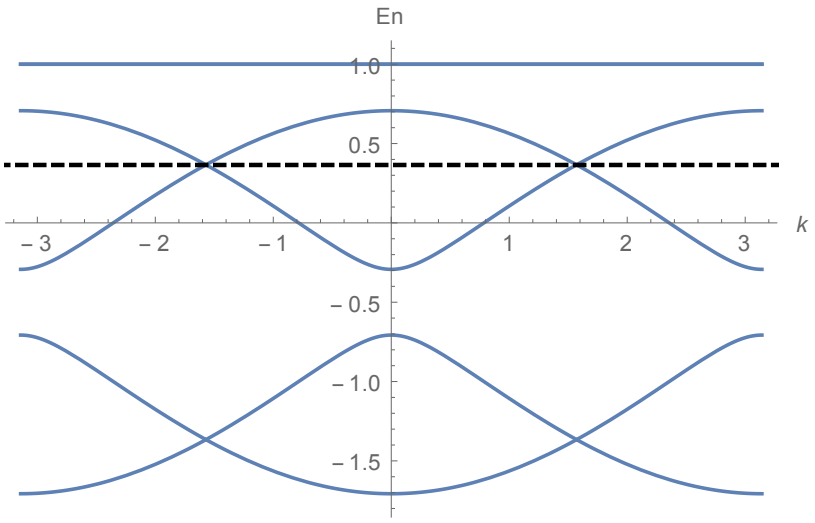

Figure 5.2: (Color online) Mean-field spectrum in the XY regime at half-filling, showing the two Dirac points. The dashed line indicates the Fermi level. The top band is doubly degenerate. These plots are made along the $k_y = -\frac{k_x}{\sqrt{3}}$ line in the Brillouin zone (along which the two Dirac points lie).

Ising Regime

For $\frac{\lambda}{J} \gtrsim 1$, non-vanishing values of Δ_1 and Δ_2 are required to satisfy the mean-field consistency equations. The solution with the lowest energy has the form $\Delta_1 = -\Delta_2 \neq 0$. This solution shifts the mean-field state away from the pattern (π, π, π) for the flux state, and opens up a gap.

The Chern number of each of the resulting bands can be computed by using the standard expression[71] in terms of the flux (through the Brillouin zone) of the Berry connections

$$C = \frac{1}{2\pi} \int_{BZ} d^2k \mathcal{F}_{xy}(k) \tag{5.20}$$

where $\mathcal{F}_{ij} = \partial_i \mathcal{A}_j - \partial_j \mathcal{A}_j$ is the flux of the Berry connection $\mathcal{A}_i = -i \langle \psi | \partial_{k_i} | \psi \rangle$. Here $|\psi\rangle$ refers to the normalized eigenvector of the corresponding band.

In the Ising regime the Chern numbers of the bands are

$$\begin{aligned} C_1 = 0 \qquad C_2 = 0 \qquad C_3 = 0 \\ C_4 = 0 \qquad C_5 = 0 \qquad C_6 = 0 \end{aligned} \tag{5.21}$$

This implies that in the Ising regime, the total Chern number for the filled bands is 0. This means that we are left with the original Chern-Simons term from the flux attachment transformation. In this regime, the fermions are essentially transmuted back to the original hard-core bosons (spins) that we began with and our analysis doesn't pick out any specific state.

5.2.2 Mean-field theory with a non-vanishing chirality field, $h \neq 0$

In this section, we will turn on the chirality term. Looking at the doubled unit cell in Fig. 5.1, there are four corresponding chirality terms (within each magnetic unit cell) which can be written as

$$\chi_{ijk}(x) = \chi_{b1}(x) + \chi_{b2}(x) + \chi_{c1}(x) + \chi_{c2}(x) \tag{5.22}$$

Now, we have to account for the additional contributions from h in Eq.(5.5). Importantly, the added contribution to the gauge fields due to a non-zero value $\phi_{(a)}(x)$ in (5.5) will give rise to additional fluxes and shift the state away from the (π, π, π) flux state observed in the XY regime section in Sec 5.2.1. Notice that, if we were stay in the (π, π, π) flux state, this would imply that the average density $\langle n_{(a)}(x)\rangle = \frac{1}{2}$ at every site. In this situation the expectation value of the chirality operator automatically vanishes due to the relation $\langle S^z_{(a)}\rangle = \frac{1}{2} - \frac{1}{2\pi}\langle B_{(a)}\rangle$. In this situation the chirality term would never pick up an expectation value at the mean-field level and time reversal symmetry would remain unbroken. Hence, in a state with broken time reversal invariance the site densities cannot all be exactly equal to $\frac{1}{2}$.

The fluxes in each of the plaquettes also gets modified due to the contribution from $\phi(x)$. The effective flux at each of the sublattice sites is now given as

$$\begin{aligned} \langle B_a\rangle =& \pi - 2\pi\Delta_1 - 2\pi\Delta_2 + 2\left(\phi_a + \phi_b + \phi_c\right) \\ \langle B_b\rangle =& \pi + 2\pi\Delta_1 - \left(\phi_a + \phi_b + \phi_c\right) \\ \langle B_c\rangle =& \pi + 2\pi\Delta_2 - \left(\phi_a + \phi_b + \phi_c\right) \end{aligned} \tag{5.23}$$

The above fluxes still ensure that we in the half-filled case.

In order to accommodate such a flux state, we also have to allow for non-zero currents in the mean-field state in Eq. (5.14). As a result we will consider an ansatz with $\langle j_k(x,t)\rangle \neq 0$. The chirality terms in

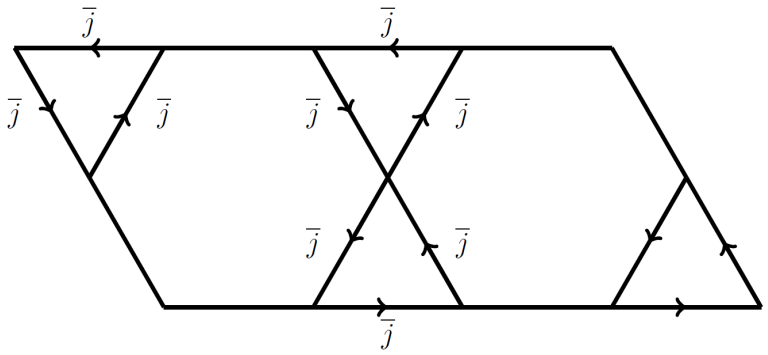

Figure 5.3: Currents induced by the chirality term in each of the triangular plaquettes. The currents are indicated by $\overline{j}$.

the Hamiltonian go across each of the triangular plaquettes in a counter-clockwise manner. Hence, we will choose an ansatz on each of the different links as seen in Fig. 5.3. The mean-field equations for the current terms in Eq.(5.14) can now be satisfied by the below choice of gauge fields

$$\begin{aligned} A_{0,a} =& 2\lambda J(\Delta_1 + \Delta_2) + \overline{j} \\ A_{0,b} =& -2\lambda J\Delta_1 - \overline{j} \\ A_{0,c} =& -2\lambda J\Delta_2 - \overline{j} \end{aligned} \tag{5.24}$$

In the above equations the effect of the chirality term directly enters in the form of a current. Now, we will proceed to look for mean-field phases that self-consistently satisfy the mean-field equations in Eq.(5.10) and Eq.(5.14) as well as constraints set by Eq.(5.5) and Eq.(5.23). Once again, we will analyze the cases of the XY and Ising regimes separately.

The XY regime

In the XY regime, $\frac{\lambda}{J} \leq 1$, we had the (π, π, π) flux state which was gapless and had two Dirac points (see Fig. 5.2). Here, we find that even for small values of h, there exist solutions with $\Delta_1 = \Delta_2 \neq 0$. This shifts the state away from the (π, π, π) flux state and opens up a gap in the spectrum as shown in Fig. 5.4.

The values of the mean-field parameters for a few different values of the field h (the strength of the chirality breaking term) are shown in Table 5.1. A plot of the mean-field spectrum for the specific case of $h = 0.05J$ is shown in Fig. 5.4. As the value of h is increased from 0, the average flux on each of the triangular plaquettes decreases from $\pi \to \frac{\pi}{2}$. The corresponding flux in the hexagonal plaquettes goes from $\pi \to 2\pi$. In the limit of a strong chirality term, one would expect to get a state with flux of 2π in

$\frac{h}{J}$	$\langle n_b \rangle = \langle n_c \rangle$	$\Delta_1 = \Delta_2$	E_G	$\langle \chi \rangle$
0	0.500	0	0	0
0.05	0.460	-0.040	$0.2286J$	0.000782
0.1	0.385	-0.115	$0.5518J$	0.001064
0.5	0.300	-0.200	$0.7351J$	0.002149
1	0.275	-0.225	$0.7638J$	0.002642

Table 5.1: Approximate values for the mean-field parameters for different values of chirality (h) for $\frac{\lambda}{J} = 1$. Here E_G denotes the energy gap in units of J, and $\langle \chi \rangle$ is the expectation value of the chirality operator. As the chirality term gets stronger, the average density on each of the triangular plaquettes approaches 0.25, and the density on the hexagonal plaquettes approaches 1.

each hexagonal plaquette, and a flux of $\frac{\pi}{2}$ in each of the triangular plaquettes. We will refer to this as the $\left(2\pi, \frac{\pi}{2}, \frac{\pi}{2}\right)$ flux phase. The values of the energy gap and the expectation values of the chirality operator are also shown for the different values of h in Table 5.1. (The energy gaps essentially measure the gaps between the Dirac points.)

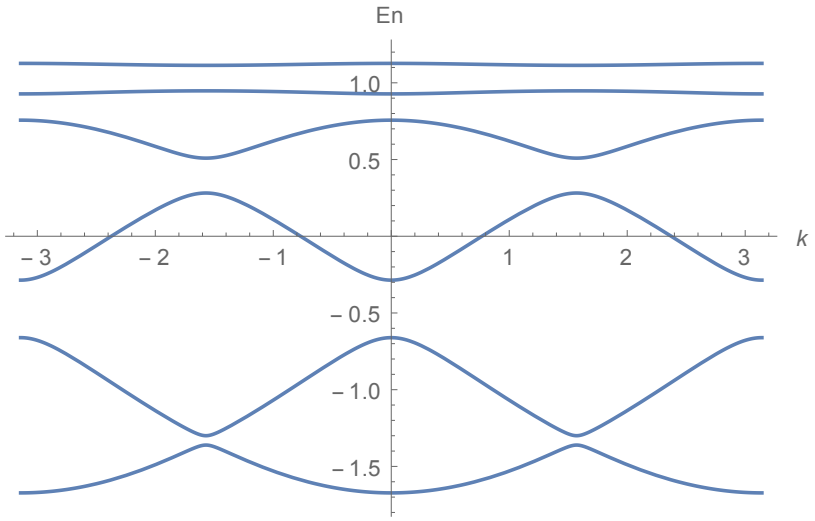

Figure 5.4: (Color online) The chirality term opens up a gap in the spectrum (see Fig 5.2. The above plot is for $h = 0.05J$. The plot is made along the $k_y = -\frac{k_x}{\sqrt{3}}$ line in the Brillouin zone.

The Chern numbers of the six bands with the chirality breaking field h turned on are

$$\begin{aligned} C_1 &= +1 \qquad C_2 = -1 \qquad C_3 = +1 \\ C_4 &= +1 \qquad C_5 = -1 \qquad C_6 = -1 \end{aligned} \tag{5.25}$$

As we are still at half-filling, the bottom three bands must be filled, leading to a total Chern number of the occupied bands of $C_1 + C_2 + C_3 = +1$. This along with the original Chern-Simons term from the

flux attachment transformation is expected to give rise to an effective Chern-Simons term with an effective parameter

$$\theta_{\text{eff}} = \theta_F + \theta_{CS} = \frac{1}{2\pi} + \frac{1}{2\pi} \tag{5.26}$$

A more detailed and rigorous computation of the above statement will be presented in a later section, Sec. 5.3, where we will include the effects of fluctuations and show that the resultant continuum action is indeed a Chern-Simons theory with the above effective parameter. This result shows that in the presence of the chirality term, we do obtain a chiral spin liquid. Such a state is equivalent to a Laughlin fractional quantum Hall state for bosons with a spin Hall conductivity $\sigma^s_{xy} = \frac{1}{2}$. The state obtained here has the same topological properties as the state that we found[43] in the magnetization plateau at $m = \frac{1}{3}$.

In the limit that we only have the chirality term, we have that $J = 0$. Now $\phi_{(a)} = \pm\frac{\pi}{2}$ in Eq.(5.5). We can now look for solutions such that

$$\phi_a = -\frac{\pi}{2} \qquad \phi_b = \phi_c = \frac{\pi}{2} \tag{5.27}$$

Here, we again recover the $(2\pi, \frac{\pi}{2}, \frac{\pi}{2})$ flux state as expected. The resulting chiral state is the same found by Bauer and coworkers in Ref.[[6]].

Ising regime

In the Ising regime, $\frac{\lambda}{J} > 1$, the Heisenberg model gave rise to a state that was gapped and a vanishing Chern number, as shown in Sec. 5.2.1. Here a small chirality term would not affect the mean-field state as long as it is weak enough. In order to see the chiral spin liquid state obtained in the XY regime in Sec. 5.2.2, one would need a strong enough chirality term to close the Ising anisotropy gaps and to open a chiral gap so as to give rises to states with non-trivial Chern numbers. Hence, the state here would be determined based on the competition between the anisotropy parameter λ and the strength of the chirality parameter h.

5.2.3 Combined effects of a chirality symmetry breaking term and an external magnetic field

So far, we have primarily focused on the case of half-filling and hence in the absence of an external magnetic field, $h_{\text{ext}} = 0$. Now we will briefly consider the scenario when the external magnetic field is present, $h_{\text{ext}} \neq 0$, in Eq. (5.1) or, equivalently, that we are at fermionic fillings other than $\frac{1}{2}$ in the XY limit. This will allow us to connect our recent results on a chiral spin liquid phase in a magnetization plateau with the chiral state arising in the presence of a chirality symmetry breaking field.

In the previous section we noted that the main effect of adding the chirality symmetry breaking term to the mean-field state was to shift the fluxes on each of the sub-lattices. We began with a (π, π, π) flux phase for the Heisenberg model and it was modified to a $(2\pi, \frac{\pi}{2}, \frac{\pi}{2})$ flux phase in the presence of a strong chirality term. Essentially the chirality term shifted the fluxes from the triangles to the hexagons. Using this analogy, we will now look for similar flux phases at other fillings. In the presence of a strong chirality term, we will consider flux phases where the flux in maximized in the hexagons and minimized in the triangles at different fillings.

In the absence of the chirality term, we have a uniform flux phase with $\langle B_a \rangle = \langle B_b \rangle = \langle B_c \rangle = \phi = 2\pi \frac{p}{q}$ with $p, q \in \mathbb{Z}$. When, we turn on the chirality term, we expect the fluxes from the triangles to shift to the hexagons. Hence, we have

$$\begin{aligned} \langle B_a \rangle =& \phi + 2\delta \\ \langle B_b \rangle =& \phi - \delta \\ \langle B_c \rangle =& \phi - \delta \end{aligned} \tag{5.28}$$

so that the total flux in each unit-cell is still the same. Such a flux state can be realized by the below choice of gauge fields

$$\begin{aligned} \bar{A}_1(\vec{x}) &= 0, & \bar{A}_2(\vec{x}) &= \phi - \delta, \\ \bar{A}_3(\vec{x}) &= 0, & \bar{A}_4(\vec{x}) &= 0, \\ \bar{A}_5(\vec{x}) &= -\phi + \delta + 3\phi x_1, & \bar{A}_6(\vec{x}) &= 3\phi x_1 \end{aligned} \tag{5.29}$$

with $\vec{x} = (x_1, x_2)$. x_1 and x_2 are the coordinates along the e_1 and e_2 directions in Fig. 5.1 respectively. The fluxes on each plaquette range between 0 and 2π, which translates to having a site filling between 0 and 1. Hence, we set $\delta = \min(\phi, \pi - \frac{\phi}{2})$. Using this choice, one can plot the Hofstadter spectrum in the limit of a strong chirality term. In Fig. 5.5 we plot the Hofstadter spectrum for the case with $\frac{h}{J} = 5$. The bottom solid line indicates the Fermi level (all the occupied states) and the top solid line indicates the next excited state available.

At most fillings the total Chern numbers of all the occupied bands is -1. This would lead to a Chern-Simons term with pre-factor $-\frac{1}{2\pi}$ and such a term would be expected to cancel when combined with the original Chern-Simons term from the flux attachment transformation, which also has a pre-factor $\frac{1}{2\pi}$. The exceptions are at the fillings $\langle n \rangle = \frac{1}{6}, \frac{1}{3}, \frac{4}{9}, \frac{1}{2}$, represented by vertical jumps in the solid lines in Fig. 5.5. At these fillings, the total Chern number of all the filled bands is different from -1 and lead to an effective Chern-Simons term. The resulting magnetization plateaus and their corresponding Chern-numbers are summarized in Table 5.2.

$\langle n \rangle$	Chern No.	m
$\frac{1}{6}$	$+1$	$\frac{2}{3}$
$\frac{1}{3}$	$+1$	$\frac{1}{3}$
$\frac{4}{9}$	$+2$	$\frac{1}{9}$
$\frac{1}{2}$	$+1$	0

Table 5.2: Magnetization plateaus obtained in Fig. 5.5 and their Chern numbers. At these fillings the Chern-Simons terms do not cancel out and the system is in a chiral spin liquid.

The magnetization plateaus at filling fractions $\frac{1}{3}$ and $\frac{1}{6}$ have also been previously obtained in the absence of the chirality symmetry breaking term, $h = 0$ and $h_{\text{ext}} \neq 0$ in Ref. [[43]]. It is apparent that these plateaus survive in the presence of the chirality symmetry breaking term. Additionally we observe two other plateaus at fillings $\frac{4}{9}$ and $\frac{1}{2}$. The plateau at $\frac{1}{2}$ filling is the same one that was observed in the previous sections for the case with no magnetic field (see Sec. 5.2.2).

The plateau at $\frac{4}{9}$ filling has a magnetic unit cell with three basic unit cells. This gives rise to a total of nine bands of which four are filled. The Chern numbers of each of the nine bands in the mean-field state are

$$\begin{aligned} C_1 = -1 \quad C_2 = +2 \quad C_3 = +2 \\ C_4 = -1 \quad C_5 = -1 \quad C_6 = +2 \\ C_7 = -1 \quad C_8 = -1 \quad C_9 = -1 \end{aligned} \tag{5.30}$$

The Chern numbers of the four filled bands (C_1, C_2, C_3, and C_4) add up to $+2$. Again this result will combine with the Chern-Simons term from the flux attachment transformation leading to an effective Chern-Simons with an effective spin Hall conductance of $\sigma^s_{xy} = \frac{2}{3}$. This result is also summarized in Table 5.2. In Ref.[[43]] we identified this state as having the same topological properties as the first state in the Jain sequence of fractional quantum Hall states of bosons.

5.2.4 Chiral Spin Liquids with Dzyaloshinskii-Moriya Interactions

In this Section, we consider the effects of a Dzyaloshinskii-Moriya term (instead of the chirality term) on the nearest neighbor XXZ Heisenberg Hamiltonian in Eq. (2.1). The Dzyaloshinskii-Moriya term is written as

$$H_{DM} = J_{DM} \sum_{i,j} \hat{z} \cdot (\boldsymbol{S}_i \times \boldsymbol{S}_j) \tag{5.31}$$

where the sum runs over nearest neighbors in each triangle in a clockwise manner. As an example the Dzyaloshinskii-Moriya term in a triangle associated with site b_1 in Fig. 5.1 can be written as

$$\begin{aligned} H_{DM,b_1} = \frac{i}{2} J_{DM} \sum_{\vec{x}} \Big(& S^+_{a_2}(\vec{x}) S^-_{b_1}(\vec{x}) - S^+_{b_1}(\vec{x}) S^-_{a_2}(\vec{x}) \\ & + S^+_{c_2}(\vec{x}) S^-_{a_2}(\vec{x}) - S^+_{a_2}(\vec{x}) S^-_{c_2}(\vec{x}) \\ & + S^+_{b_1}(\vec{x}) S^-_{c_2}(\vec{x}) - S^+_{b_1}(\vec{x}) S^-_{c_2}(\vec{x}) \Big) \end{aligned} \tag{5.32}$$

Clearly this term breaks time reversal so we expect that we may be able to find chiral phases.

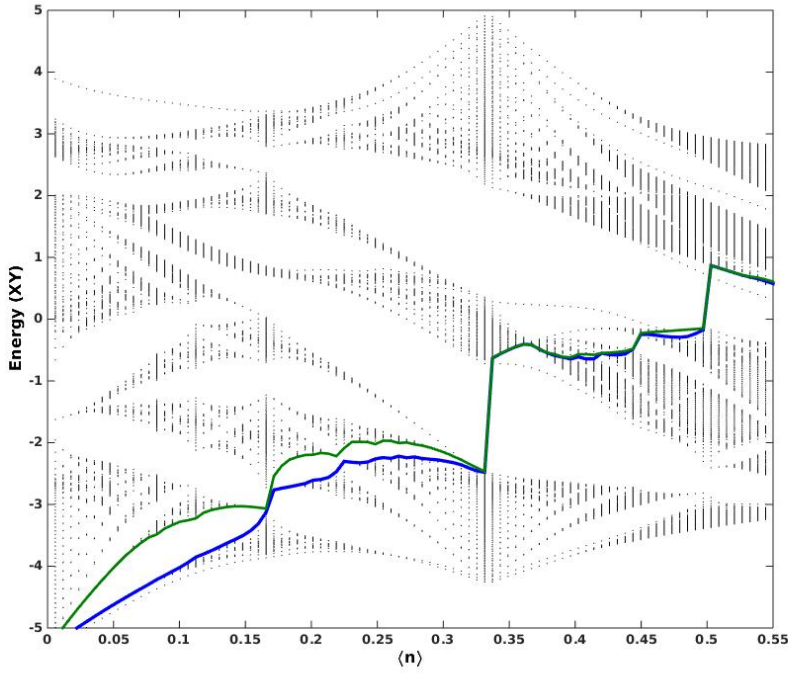

Figure 5.5: (color online) Hofstadter spectrum for $h = 5J$. The x-axis plots the mean-field fermion density $\langle n \rangle$ and the y-axis plots the XY energies. The bottom solid line indicates the fermi level and the top solid line corresponds to the next excited state available. The vertical jumps in the figure correspond to possible magnetization plateaus.

From the form of Eq.(5.32), we can now readily apply the flux attachment transformation just like we had for the case of the chirality term. As a result the parameters in Eq.(5.5) now get modified as

$$\begin{aligned} \overline{J}_{(a)}(x) =& \frac{1}{2} \sqrt{J^2 + \left[h \left(\frac{1}{2} - n_{(a)}(x) \right) + J_{DM} \right]^2} \\ \phi_{(a)}(x) =& \tan^{-1} \left(\frac{h}{J} \left(\frac{1}{2} - n_{(a)}(x) \right) + \frac{J_{DM}}{J} \right) \end{aligned} \tag{5.33}$$

In this section, we will set the chirality symmetry breaking term to zero, $h = 0$.

Two separate regimes have to be considered.

$J_{DM} \lesssim 1.7J$

Recall that in the XY regime the Heisenberg model gave rise to the (π, π, π) flux state which is gapless and has Dirac points (Fig. 5.2). Treating the Dzyaloshinskii-Moriya term as a perturbation, we find that this term also opens up a gap in the (π, π, π) flux state as can be seen in Fig. 5.6. But a the resultant state obtained still has a flux of π in each of the plaquettes. For the situation shown in Fig 5.6, the energy gap is 0.1366J. This is an important difference between the effects of adding the chiral term and the Dzayloshinkii-Moriya terms, since the chirality term shifted the fluxes on each plaquette away from π whereas the Dzyaloshinskii-Moriya term does not.

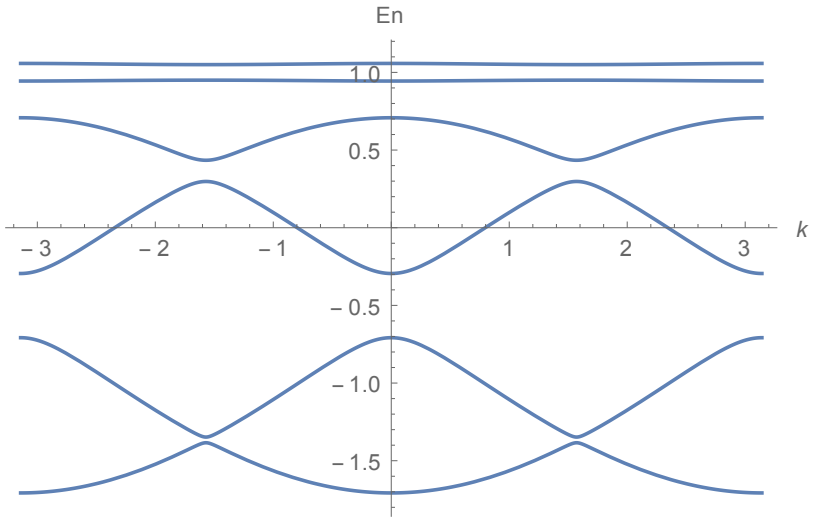

Figure 5.6: (color online) Spectrum with $J_{DM} = 0.05J$. The Dzyaloshinskii-Moriya term opens up a gap in the spectrum of the Heisenberg Hamiltonian (see Fig. 5.2).

The Chern numbers of the six bands in the presence of a small J_{DM} term are

$$\begin{aligned} C_1 = +1 \qquad C_2 = -1 \quad C_3 = +1 \\ C_4 = +1 \qquad C_5 = -1 \quad C_6 = -1 \end{aligned} \tag{5.34}$$

Once again, we find that the total Chern number of all the filled bands is $C_1 + C_2 + C_3 = +1$. This would again lead to a fractional quantum Hall type phase with $\sigma^s_{xy} = \frac{1}{2}$, just as we had observed in the case with the chirality term.

$J_{DM} \gtrsim 1.7J$

For larger values of the Dzyaloshinkii-Moriya parameter, namely for $\frac{J_{DM}}{J} \gtrsim 1.7$, the Chern numbers of the bands again get rearranged and the chiral phase no longer survives, as shown below

$$\begin{aligned} C_1 = -1 \qquad C_2 = +1 \quad C_3 = -1 \\ C_4 = -1 \qquad C_5 = +1 \quad C_6 = +1 \end{aligned} \tag{5.35}$$

In the limit that we only have the Dzyaloshinskii-Moriya term, i.e. $J = 0$, the values of all $\phi_{(a)} = \frac{\pi}{2}$ in Eq.(5.33). In this case the values of the mean-field parameters that satisfy the consistency equations, Eq.(5.10) and Eq. (5.14), are $\Delta_1 = \Delta_2 = -\frac{1}{4}$. Hence, in the presence of only the Dzayloshinkii-Moriya term, we again end up in the (π, π, π) flux state that was observed in the XY regime of the Heisenberg model in Sec 5.2.1.

5.2.5 Dzyaloshinskii-Moriya term with an uniform magnetic field, $h_{\text{ext}} \neq 0$

Finally, we will also consider the effects of the Dzyaloshinskii-Moriya term in the presence of an uniform external magnetic field $h_{\text{ext}} \neq 0$, just as we had done for the chirality terms in Sec. 5.2.3. We will once again focus on the XY limit where the mean-field equations are simpler due to the absence of the interaction term, i.e. $\lambda = 0$. We will look for states that are uniform, time-independent and don't have any currents.

This scenario is very similar to the case of the integer quantum Hall effect with non-interacting fermions in the presence of a (statistical) gauge field. This approach was also used by Misguich et. al. in their studies on the triangular lattice.[53] More recently, we carried out a similar analysis on the kagome lattice with an XY nearest neighbor Heisenberg model.[43] Here, we will perform the same analysis, but with the Dzyaloshinskii-Moriya term added to the XY nearest neighbor Heisenberg model.

Once again, we find a few different plateaus as can be seen in the Hofstadter spectrum in Fig 5.7 for $J_{DM} = 0.3J$. The vertical lines in the figure correspond to the magnetization plateaus. The range of J_{DM} values for which we observe the above plateaus is shown in Table 5.3. The table also lists the total Chern numbers of all the filled bands at each of the plateaus as well as the corresponding magnetization.

This concludes our mean-field analysis into the various possible magnetization plateaus. We will now proceed to consider the effects of fluctuations on the mean-field state when a small chirality term was added to the Heisenberg model in the XY limit. This was the situation discussed in Sec 5.2.2. For the rest of the paper, we will not consider the Dzyaloshinskii-Moriya term or the external magnetic field term again.

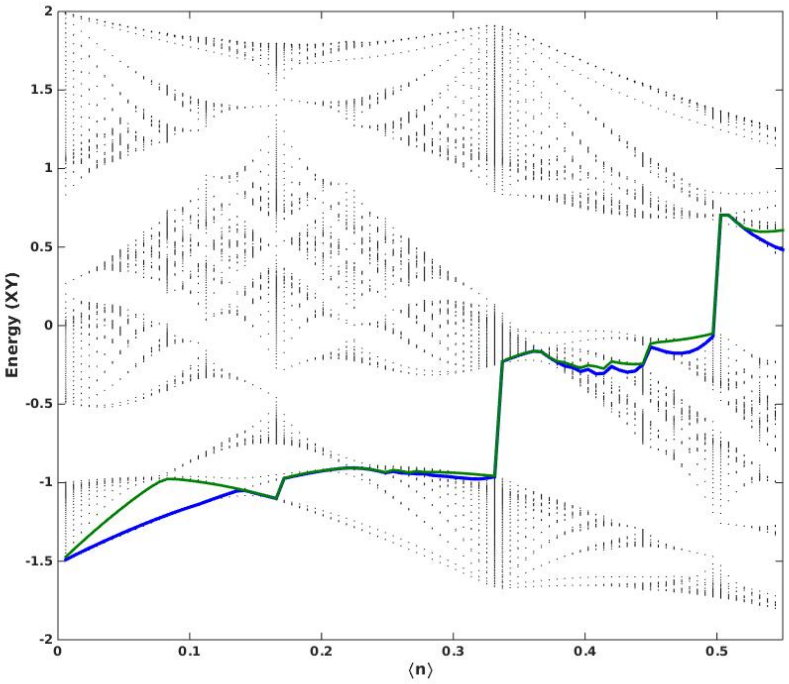

Figure 5.7: (Color online) Hosftadter spectrum in the XY limit for the case $J_{DM} = 0.3J$. (The x-axis plots the mean-field fermion density $\langle n \rangle$ and the y-axis plots the energies of the XY model.) The bottom solid line represents the Fermi level (all the filled bands) and the top solid line represents the next excited energy state available. The plateaus correspond to jumps in the solid line. We see two additional plateaus at densities $\langle n \rangle = \frac{4}{9}, \frac{1}{2}$ for certain values of J_{DM}.

$\langle n \rangle$	Range of values (in J)	Chern No.	m
$\frac{1}{6}$	$0 \leq J_{DM} \lesssim 0.35$	$+1$	$\frac{2}{3}$
$\frac{2}{9}$	$0 \leq J_{DM} \lesssim 0.3$	$+2$	$\frac{5}{9}$
$\frac{1}{3}$	$0 \leq J_{DM} \lesssim 0.8$	$+1$	$\frac{1}{3}$
$\frac{4}{9}$	$0.05 \lesssim J_{DM} \lesssim 0.6$	$+2$	$\frac{1}{9}$
$\frac{1}{2}$	$0 < J_{DM} \lesssim 1.7$	$+1$	0

Table 5.3: Approximate values of J_{DM} for which we observe the plateaus at the mean-field level. This table also lists the corresponding Chern numbers and their magnetizations, m.

5.3 Effective Field Theory

In this section we return to the case of the nearest neighbor Heisenberg model in the presence of a small chirality term. In Sec. 5.2.2, it was shown that the addition of the chirality term opened up a gap in the mean-field spectrum and lead to a state with non-trivial Chern number. We will now expand the fermionic action around this mean-field state and consider its continuum limit. This process will allow us to go beyond the mean-field level and consider the fluctuation effects of the statistical gauge fields. The analysis presented here is analogous to the one presented in our earlier work.[43] As a result we will only write down the relevant expressions for the current scenario.

In Sec. 5.2.2, we found that in the absence of the chirality term the spectrum was gapless with two Dirac points and that the addition of the chirality term opened up a gap at the Dirac points. These two Dirac points in the mean-field phase were located at the momenta $\mathbf{K} = \pm\left(\frac{\pi}{2}, -\frac{\pi}{2\sqrt{3}}\right)$. The fermionic degrees of freedom on each site can be expanded around each of the two Dirac points using the following expansions on each sub-lattice

$$\begin{pmatrix} \psi_{a1} \\ \psi_{b1} \\ \psi_{c1} \\ \psi_{a2} \\ \psi_{b2} \\ \psi_{c2} \end{pmatrix} \sim \frac{a_0}{\sqrt{6}} \begin{pmatrix} -e^{i\frac{5\pi}{12}} & i \\ \sqrt{2} & 0 \\ -e^{i\frac{5\pi}{12}} & -e^{-i\frac{\pi}{6}} \\ -e^{i\frac{5\pi}{12}} & i \\ 0 & -\sqrt{2}e^{-i\frac{\pi}{12}} \\ -e^{-i\frac{\pi}{12}} & e^{-i\frac{\pi}{3}} \end{pmatrix} \begin{pmatrix} \Psi_1^1 \\ \Psi_1^2 \end{pmatrix} \tag{5.36}$$

$$\begin{pmatrix} \psi_{a1} \\ \psi_{b1} \\ \psi_{c1} \\ \psi_{a2} \\ \psi_{b2} \\ \psi_{c2} \end{pmatrix} \sim \frac{a_0}{\sqrt{6}} \begin{pmatrix} -e^{i\frac{5\pi}{12}} & -i \\ 0 & -\sqrt{2}e^{-i\frac{\pi}{12}} \\ e^{i\frac{\pi}{12}} & -e^{i\frac{\pi}{3}} \\ e^{i\frac{5\pi}{12}} & -i \\ -\sqrt{2} & 0 \\ -e^{-i\frac{5\pi}{12}} & -e^{-i\frac{\pi}{6}} \end{pmatrix} \begin{pmatrix} \Psi_2^1 \\ \Psi_2^2 \end{pmatrix} \tag{5.37}$$

where in Ψ_r^α, r refers to the Dirac species index and the label α refers to the spinor index within each species. $\psi_{a1}, \psi_{b1}, \psi_{c1}, \psi_{a2}, \psi_{b2}, \psi_{c2}$ refer to the original fermionic fields on the different sub-lattices sites in the mean-field state at half-filling as shown in Fig 5.1.

Now we will include the fluctuating components i.e. we will expand the statistical gauge fields as follows $A_\mu = \langle A_\mu \rangle + \delta A_\mu$. The mean-field values of $\langle A_\mu \rangle$ are the same as those given in Sec. 5.2.2. From now on, we will primarily focus on the fluctuating components. In order to simplify the notation, we will drop the

δ label in the fluctuating components i.e. all the gauge fields presented beyond this point are purely the fluctuating components.

5.3.1 Spatial fluctuating components

First, we will begin by looking at just the spatial fluctuating components. Further, we will also expand all the spatial fluctuating components in the magnetic unit cell in Fig. 5.1 in terms of slow and fast components. This will allow us to treat the slow components as the more relevant fields.

The fields along the e_1 direction (in Fig. 5.1) can be expanded as

$$\begin{aligned} A_1^1 =& \frac{a_0}{2}\left(A_x + A_1^{f1} + A_1^{f2} - A_1^{f3}\right) \\ A_4^1 =& \frac{a_0}{2}\left(A_x + A_1^{f1} - A_1^{f2} + A_1^{f3}\right) \\ A_1^2 =& \frac{a_0}{2}\left(A_x - A_1^{f1} + A_1^{f2} - A_1^{f3}\right) \\ A_4^2 =& \frac{a_0}{2}\left(A_x - A_1^{f1} - A_1^{f2} + A_1^{f3}\right) \end{aligned} \tag{5.38}$$

Similarly, the fields along the e_2 direction can be written as

$$\begin{aligned} A_2^1 =& \frac{a_0}{2}\left(-\frac{1}{2}A_x + \frac{\sqrt{3}}{2}A_y - A_2^{f1} - A_2^{f2} + A_2^{f3}\right) \\ A_5^1 =& \frac{a_0}{2}\left(-\frac{1}{2}A_x + \frac{\sqrt{3}}{2}A_y + A_2^{f1} + A_2^{f2} - A_2^{f3}\right) \\ A_2^2 =& \frac{a_0}{2}\left(-\frac{1}{2}A_x + \frac{\sqrt{3}}{2}A_y + A_2^{f1} - A_2^{f2} + A_2^{f3}\right) \\ A_5^2 =& \frac{a_0}{2}\left(-\frac{1}{2}A_x + \frac{\sqrt{3}}{2}A_y - A_2^{f1} + A_2^{f2} - A_2^{f3}\right) \end{aligned} \tag{5.39}$$

Finally, the fields along $e_1 + e_2$ directions can be expressed as

$$\begin{aligned} A_3^1 =& \frac{a_0}{2}\left(\frac{1}{2}A_x + \frac{\sqrt{3}}{2}A_y + \frac{3}{2}A^f - A_3^{f1} - A_3^{f2} + A_3^{f3}\right) \\ A_6^1 =& \frac{a_0}{2}\left(\frac{1}{2}A_x + \frac{\sqrt{3}}{2}A_y + \frac{3}{2}A^f + A_3^{f1} + A_3^{f2} - A_3^{f3}\right) \\ A_3^2 =& \frac{a_0}{2}\left(\frac{1}{2}A_x + \frac{\sqrt{3}}{2}A_y + \frac{3}{2}A^f - A_3^{f1} - A_3^{f2} + A_3^{f3}\right) \\ A_6^2 =& \frac{a_0}{2}\left(\frac{1}{2}A_x + \frac{\sqrt{3}}{2}A_y + \frac{3}{2}A^f - A_3^{f1} + A_3^{f2} - A_3^{f3}\right) \end{aligned} \tag{5.40}$$

In the above expressions $A_i^{(A)}$ refer to the fluctuating components along the different links of the unit cell in the mean-field state (1 and 2 refer to the two unit cells in the magnetic unit cel shown in Fig. 5.1). The slow components are represented by A_x and A_y and A^f, A_i^{f1}, A_i^{f2} and A_i^{f3} are the fast fields along the

different spatial directions.

5.3.2 Temporal fluctuating components

Similarly, the fluctuating time components can also be expanded in terms of slow and fast fields as follows

$$\begin{aligned}
A_{0,a1} =& a_0 \left(A_0 + A_0^{f01} + A_0^{f01} + 3\sqrt{2}(A_0^{f1} - A_0^{f2}) \right) \\
A_{0,b1} =& a_0 \left(A_0 - A_0^{f10} - 3A_0^{f3} \right) \\
A_{0,c1} =& a_0 \left(A_0 - A_0^{f01} + 3\sqrt{2-\sqrt{3}} A_0^{f1} - 3\sqrt{2+\sqrt{3}} A_0^{f2} \right) \\
A_{0,a2} =& a_0 \left(A_0 + A_0^{f01} + A_0^{f01} - 3\sqrt{2}(A_0^{f1} - A_0^{f2}) \right) \\
A_{0,b2} =& a_0 \left(A_0 - A_0^{f10} + 3A_0^{f3} \right) \\
A_{0,c1} =& a_0 \left(A_0 - A_0^{f01} - 3\sqrt{2-\sqrt{3}} A_0^{f1} + 3\sqrt{2+\sqrt{3}} A_0^{f2} \right)
\end{aligned} \tag{5.41}$$

where $a1$, $b1$, $c1$, $a2$, $b2$ and $c2$ again refer to the different sub-lattice indices in the mean-field state in Fig 5.1. The only temporal slow component is A_0. All the other fields with super-script f refer to the fast fields. The pre-factors and constants in Eq.(5.41) are chosen to make the notation and computation below easier.

Using Eq.(5.37), the mean-field action with the choice of the mean-field gauge fields in Sec 5.2.2 in the continuum limit becomes

$$S_{F,MF} = \int d^3x \overline{\Psi}_r (i\not{\partial} - m)\Psi_r \tag{5.42}$$

where $\overline{\Psi} = \Psi^* \gamma_0$ with $\Psi = \begin{pmatrix} \Psi_1^1, & \Psi_1^2, & \Psi_1^2, & \Psi_2^2 \end{pmatrix}^T$. We are using the slash notation $\not{\partial} = \gamma^\mu \partial_\mu = \gamma_0 \partial_0 - \gamma_i \partial_i$ with the Minkowski metric $g_{\mu\nu}$. The gamma matrices act on the upper or spinor index (α) in Ψ_r^α and are given by

$$\gamma_0 = \sigma_3 \qquad \gamma_1 = i\sigma_2 \qquad \gamma_2 = i\sigma_1 \tag{5.43}$$

Importantly the mass terms m are the same for both the Dirac points and are given as

$$m = \lim_{a_0 \to 0} \left[-\frac{\pi\Delta}{9a_0}(3+\sqrt{3}) \right] = -\frac{0.5258}{a_0}\Delta > 0 \tag{5.44}$$

Hence, the masses m are positive for *both* Dirac points as the value of $\Delta < 0$ from the mean-field analysis (as shown in Table 5.1).

The resulting action for the spatial fluctuating components becomes

$$\begin{aligned}\delta S_i^{\text{slow}} &= \int d^3x \left\{ A_x \overline{\Psi}\gamma_1\Psi + A_y \overline{\Psi}\gamma_2\Psi \right\} \\ \delta S_i^{\text{fast}} &= \int d^3x \left\{ \frac{1}{2} A^f \overline{\Psi}\gamma_1\Psi + \frac{\sqrt{3}}{2} A^f \overline{\Psi}\gamma_2\Psi - (A_1^{f2} - A_1^{f3} + A_2^{f2} - A_2^{f3} - A_3^{f2} + A_3^{f3})\overline{\Psi}\Psi \right\}\end{aligned} \tag{5.45}$$

where we have absorbed some of the constant factors into the definitions of the fast fields to make the notation more convenient and the definitions of the gamma matrices are the same as in Eq. (5.43).

The resulting continuum action for the slow and fast fields become

$$\begin{aligned}\delta S_0^{\text{slow}} &= -\int d^3x A_0 \left(\overline{\Psi}\gamma_0\Psi \right) \\ \delta S_0^{\text{fast}} &= \int d^3x \left\{ A_0^{f1} \left(\overline{\Psi}\gamma_1 T^3 \Psi \right) + A_0^{f2} \left(\overline{\Psi}\gamma_2 T^3 \Psi \right) + A_0^{f3} \left(\overline{\Psi}\gamma_0 T^3 \Psi \right) \right\}\end{aligned} \tag{5.46}$$

where T^3 is the regular σ_3 Pauli matrix but acting on the species index r in Ψ_r.

Combining equations Eq.(5.42), Eq.(5.45) and Eq. (5.46), the total continuum fermionic action for the slow components becomes

$$S_{F,\text{slow}} = \int d^3x \overline{\Psi} \left[i\gamma^\mu D_\mu - m \right] \Psi \tag{5.47}$$

where $D_\mu = \partial_\mu + iA_\mu$ is the covariant derivative.

The fast components can be expressed as

$$S_{F,\text{fast}} = \int d^3x \left\{ \frac{1}{2} A^f \overline{\Psi}\gamma_1\Psi + A^f \frac{\sqrt{3}}{2} \overline{\Psi}\gamma_2\Psi + A_0^{f1} \overline{\Psi}\gamma_1 T^3 \Psi + A_0^{f2} \overline{\Psi}\gamma_2 T^3 \Psi + A_0^{f3} \overline{\Psi}\gamma_0 T^3 \Psi - \phi_i \overline{\Psi}\Psi \right\} \tag{5.48}$$

where

$$\phi_i = \frac{\sqrt{2+\sqrt{3}}}{3} \left(A_1^{f2} - A_1^{f3} + A_2^{f2} - A_2^{f3} - A_3^{f2} + A_3^{f3} \right) \tag{5.49}$$

Eq.(5.47) and Eq. (5.48) can also be expressed in momentum space as

$$S_F = \int \frac{d^3p}{(2\pi)^3} \overline{\Psi} M \Psi \tag{5.50}$$

with $M = \overline{M} + \delta M$. The mean-field part $\overline{M}$ is given as

$$\overline{M} = \begin{pmatrix} \not{p} - m & 0 \\ 0 & \not{p} - m \end{pmatrix} \tag{5.51}$$

and the fluctuation part δM is given as

$$\delta M = \begin{pmatrix} \delta M_{11} & 0 \\ 0 & \delta M_{22} \end{pmatrix} \tag{5.52}$$

where

$$\begin{aligned} \delta M_{11} &= -\not{A} - \phi_i + \left(\frac{1}{2}A^f + A_0^{f1}\right)\gamma_1 + \left(\frac{\sqrt{3}}{2}A^f + A_0^{f2}\right)\gamma_2 + A_0^{f3}\gamma_0 \\ \delta M_{22} &= -\not{A} - \phi_i + \left(\frac{1}{2}A^f - A_0^{f1}\right)\gamma_1 + \left(\frac{\sqrt{3}}{2}A^f - A_0^{f2}\right)\gamma_2 - A_0^{f3}\gamma_0 \end{aligned} \tag{5.53}$$

and ϕ_i is given in Eq.(5.49).

The action in Eq.(5.50) is quadratic in fermionic fields and fermions can be integrated out to give an effective action in terms of just the fluctuating gauge fields. The resulting effective action becomes

$$S_{\text{eff}} = -i\text{Tr}\ln M \tag{5.54}$$

where M is defined in Eq.(5.52). Now we can expand M in terms of the mean-field part and the fluctuating parts as shown in Eq.(5.51) and Eq.(5.52).

$$\begin{aligned} S_{\text{eff}} &= -i\text{Tr}\left\{\ln\left(\overline{M} + \delta M\right)\right\} \\ &= -i\text{Tr}\left\{\ln \overline{M}\right\} - i\text{Tr}\left\{\ln\left(1 + \overline{M}^{-1}\delta M\right)\right\} \end{aligned} \tag{5.55}$$

Expanding this action up to second order in the fluctuating components gives

$$\begin{aligned} S_{\text{eff}} =& \frac{i}{2}\text{Tr}\left(\overline{M}^{-1}\delta M \overline{M}^{-1}\delta M\right) \\ =& \frac{i}{2}\int_{p,q} \text{tr}\left(\overline{S}(p)\delta M(q)\overline{S}(p+q)\delta M(-q)\right) \end{aligned} \tag{5.56}$$

where the lower-cased 'tr' is a matrix trace, and $\overline{S}(p) = \overline{M}(p)^{-1}$ is the continuum mean-field propagator presented in Eq. (5.51), and it is given by

$$\overline{S}(p) = \frac{1}{p^2 - m^2}\begin{pmatrix} \not{p} + m & 0 \\ 0 & \not{p} + m \end{pmatrix} \tag{5.57}$$

In the expansion of Eq.(5.55) we will only keep the most relevant (mass) terms (without derivatives) for the fast components.

Similarly, one can also express the lattice version of the Chen-Simons term and the interaction terms

using the slow and fast fluctuating components. Combining all of the above terms, one can obtain the final continuum action. All the massive fields can safely be integrated out. This leaves us with just the Chern-Simons and Maxwell terms. The computation of this Feynam diagram is standard and it is done in many places in the literature.[65, 26]

To lowest order, after integrating out all the massive fields, the most relevant term is the effective Chern-Simons term S_{eff}^{CS}, since it has the smallest number of derivatives, and is given by

$$S_{\text{eff}}^{CS} = \left(\frac{\theta}{2} + \frac{\theta_F}{2}\right) \int d^3x \epsilon^{\mu\nu\lambda} A_\mu \partial_\nu A_\lambda \tag{5.58}$$

where $\theta = \frac{1}{2\pi}$ from the original flux attachment transformation and θ_F is the obtained from integrating out the fermions and is given as

$$\theta_F = \frac{1}{4\pi}(\text{sgn}(m) + \text{sgn}(m)) = \frac{1}{2\pi} \tag{5.59}$$

as $\text{sgn}(m) = +1$ ($m > 0$ as shown in Eq.(5.44)).

Hence, the Chern-Simons terms add up, and we get a state with spin Hall conductivity $\sigma_{xy}^s = \frac{1}{2}$. This state is equivalent to a bosonic Laughlin fractional quantum Hall state. This agrees and verifies our expected result obtained in Sec. 5.2.2.

The Maxwell terms can be conveniently expressed in terms of the electric $\mathbf{E}$ and magnetic B fields as follows

$$S_{EM} = \int d^3x \left(\frac{1}{2}\epsilon \mathbf{E}^2 - \frac{1}{2}\chi B^2\right) \tag{5.60}$$

where $\epsilon = \frac{1}{16\pi\sqrt{m^2}}$ and $\chi = \left(24\sqrt{3}a_0 - \frac{1}{16\pi\sqrt{m^2}}\right)$.

The computation in this section confirms our expectation and analysis used to determine the nature of the chiral spin liquid states using the mean-field theory approaches in Sec. 5.2.

5.4 Spontaneous breaking of time reversal invariance

In the cases discussed so far in this paper, we began with a (π, π, π) flux state which , at the level of the mean field theory, has massless Dirac fermions, and showed that breaking the time-reversal symmetry explicitly, by adding either a chirality term (Sec. 5.2.2) or a Dzyaloshinskii-Moriya term (Sec. 5.2.4), led to a gapped state. We the showed, that quantum corrections led directly to a chiral spin liquid with broken time-reversal symmetry for arbitrarily small values of the chiral field h or the Dzyaloshinskii-Moriya interaction J_{DM}. The existence of an explicit gap in the spectrum of the fermions was essential to this analysis. Furthermore, after the leading quantum corrections are taken into account, we found that the naive Dirac fermions of the

mean-field theory became anyons (semions in the cases that were discussed in detail). This line of reasoning parallels the theory of the fractional quantum Hall effect where, at the mean field level, one begins with composite fermions fulling up effective Landau levels,[36] which turn into anyons by virtue of the quantum corrections.[48, 26]

We now turn to the question of whether it is possible to obtain a chiral spin liquid by spontaneous time-reversal symmetry breaking. This concept was formulated originally by Wen, Wilczek and Zee[79] in the context of the $J_1 - J_2$ Heisenberg model on the square lattice, where a chirally-invariant $\mathbb{Z}_2$ spin liquid appears to be favored instead.[38, 39] In this section we will show that ring-exchange processes on the bow ties (i.e. two triangles sharing the same spin) of the kagome lattice may favor the spontaneous formation of the chiral spin liquid if the associated coupling constant is large enough. Unfortunately, the critical value of this coupling constant that we obtain is much too large for the mean field theory to be reliable and, hence, we cannot exclude the possibility that other states may arise at weaker coupling. Nevertheless, it is an instructive excercise that shows that ring-exchange processes, if large enough, may trigger a chiral spin liquid on their own.

In this section we explore of the possibility of breaking this symmetry spontaneously. Numerical works have studied examples where such scenarios arise in the Heisenberg model on the kagome lattice in the presence of second and third next nearest neighbor Heisenberg terms or Ising terms,[32, 29] where they find suggestive evidence of a chiral spin liquid in certain regimes. Unfortunately, the flux attachment transformation cannot be applied to next nearest neighbor Heisenberg terms. However, we have examined the case in the presence of just the next nearest neighbor Ising terms, using flux attachment methods and we do not find the chiral spin liquid observed in the numerical work.[32]

As a result we consider the effect of adding a chiral term on a bowtie in the kagome lattice which is written explicitly as follows

$$H_{\bowtie} = g \sum_{\{\bowtie\}} \left[\boldsymbol{S}_i \cdot (\boldsymbol{S}_j \times \boldsymbol{S}_k)\right] \left[\boldsymbol{S}_i \cdot (\boldsymbol{S}_l \times \boldsymbol{S}_m)\right] \tag{5.61}$$

where the sum runs over all the bowties of the kagome lattice, i, j, and k refer to the indices of the up triangle and i, l and m refer to the indices of the down triangle, with i being the common site in the bowtie.

The total Hamiltonian used in this section, can then be written as

$$\begin{aligned} H_{tot} =& H_{XXZ} + H_{\bowtie} \\ =& H_{XXZ} + \sum_{\langle \triangle, \triangledown \rangle} g \chi_{\triangle} \chi_{\triangledown} \end{aligned} \tag{5.62}$$

where the H_{XXZ} is the Hamiltonian of the Heisenberg antiferromagnet on the kagome lattice, with anisotropy

coupling λ and where $\chi_{\triangle}$ and $\chi_{\triangledown}$ are the chiralities over the up and down triangles (i.e. the sites of the two sublattices of the honeycomb lattice) and the sum runs over nearest-neighbor triangles of the kagome lattice (which correspond to the bowties). In what follows we will assume that we are either at the isotropic point or in the regime of XY anisotropy (easy plane), i.e. $\lambda \leq 1$.

We now note that the bowtie terms of the Hamiltonian in Eq.(5.61), when expanded, can be expressed in terms of a ring-exchange term on the bowtie as follows

$$\begin{aligned} H_{\bowtie} = \frac{g}{2} \sum_{\{\bowtie\}} \Big\{ & \boldsymbol{S}_i \cdot \boldsymbol{S}_i \left[(\boldsymbol{S}_j \cdot \boldsymbol{S}_l)(\boldsymbol{S}_k \cdot \boldsymbol{S}_m) - (\boldsymbol{S}_j \cdot \boldsymbol{S}_m)(\boldsymbol{S}_k \cdot \boldsymbol{S}_l) \right] \\ & + \boldsymbol{S}_i \cdot \boldsymbol{S}_l \left[(\boldsymbol{S}_j \cdot \boldsymbol{S}_m)(\boldsymbol{S}_i \cdot \boldsymbol{S}_k) - (\boldsymbol{S}_i \cdot \boldsymbol{S}_j)(\boldsymbol{S}_k \cdot \boldsymbol{S}_m) \right] \\ & + \boldsymbol{S}_i \cdot \boldsymbol{S}_m \left[(\boldsymbol{S}_i \cdot \boldsymbol{S}_j)(\boldsymbol{S}_k \cdot \boldsymbol{S}_l) - (\boldsymbol{S}_j \cdot \boldsymbol{S}_l)(\boldsymbol{S}_i \cdot \boldsymbol{S}_k) \right] \Big\} \end{aligned} \tag{5.63}$$

Ring exchange terms have been known to give rise to exotic dimer states in Heisenberg antiferromagnets.[68] Here, we will explore the possibility of such a term giving rise to a chiral spin liquid state.

Since the triangles of the kagome can be labelled by the sites of a honeycomb lattice on the centers of the triangles, we can regard the Hamiltonian of Eq.(5.61) as a coupling between the chiralities on a honeycomb lattice. Although Eq. (5.63) has a very complicated form, it can be simplified by using a Hubbard-Stratonovich (HS) transformation in terms of a scalar field $h(\boldsymbol{r}, t)$ on the sites $\{\boldsymbol{r}\}$ to the honeycomb sublattice of the triangles of the kagome lattice. Upon this transformation, the action of the full system, XXZ and chirality couplings, becomes

$$S = S_{XXZ} + \int dt \frac{1}{2g} \sum_{\boldsymbol{r},\boldsymbol{r}'} h(\boldsymbol{r}, t) K^{-1}(\boldsymbol{r}, \boldsymbol{r}') h(\boldsymbol{r}', t) - \int dt \sum_{\boldsymbol{r}} h(\boldsymbol{r}, t) \chi(\boldsymbol{r}, t) \tag{5.64}$$

where $K(\boldsymbol{r}, \boldsymbol{r}')$ is the coordination (or connectivity) matrix of the honeycomb lattice and $K^{-1}(\boldsymbol{r}, \boldsymbol{r}')$ is its inverse. The HS field $h(\boldsymbol{r}, t)$ plays the role of the chirality field introduced in Sec.5.2.2, except that here it is a function of time and space.

We can now apply the flux-attachment transformation to a system whose action is given by Eq.(5.64), and, as we did in the preceding sections, map this problem to a system of fermions on the kagome lattice coupled to a lattice Chern-Simons gauge field. However now they are also coupled to the HS fields $h(\boldsymbol{r}, t)$ in the same fashion as we coupled the fermions to the chiral operator in Sec. 5.2.2.

We can now integrate out the fermions, we obtain the following effective action

$$S = S_{XXZ} + \int dt \frac{1}{2g} \sum_{\boldsymbol{r},\boldsymbol{r}'} h(\boldsymbol{r}, t) K^{-1}(\boldsymbol{r}, \boldsymbol{r}') h(\boldsymbol{r}', t) + S_{\text{eff}}[h(\boldsymbol{r}, t), A_\mu(\boldsymbol{r}, t)] \tag{5.65}$$

where $S_{\rm eff}[h(\boldsymbol{r},t), A_\mu(\boldsymbol{r},t)]$ is the effective action of the fermions in a background chirality field $h(\boldsymbol{r},t)$ (and which includes the lattice Chern-Simons term, as before).

We can now carry out a mean-field approximation by extremizing the action of Eq.(5.65) with respect to the chirality field $h(\boldsymbol{r},t)$, and to the gauge field A_μ. Since we are working at zero external magnetic field, the mean field state for the gauge field is just the (π,π,π) flux state and, hence, in the absence of any other interactions, we will naively have two species of massless Dirac fermions (as discussed in Sec.5.3). We will take the extremal HS field to have a time-independent value on each sublattice, $\bar{h}_\triangle$ and $\bar{h}_\triangledown$, which obey the equations

$$\bar{h}_\triangle = 3g\langle\chi_\triangledown\rangle, \qquad \bar{h}_\triangledown = 3g\langle\chi_\triangle\rangle \tag{5.66}$$

where $\langle\chi(\boldsymbol{r},t)\rangle$ is the expectation value of the chirality operator on each sublattice. If we further seek solutions that do not break the sublattice symmetry, we obtain the simple mean field equation for the chirality

$$\bar{h} = 3g\ \langle\chi\rangle \tag{5.67}$$

and the critical value of the chirality coupling g_c is given by the usual mean-field-theory relation

$$1 = 3g_c \frac{d\langle\chi\rangle}{dh}\Big|_{h=0} \tag{5.68}$$

where $\frac{d\langle\chi\rangle}{dh}\Big|_{h=0}$ is the chirality susceptibility of the XXZ model.

For $\lambda/J = 0$, we find that for values of $g \gtrsim 13.3J$, there exist non-vanishing solutions of the chirality parameter i.e. $h > 0$ as can be seen in Fig. 5.8. In these cases, we end up with a non-zero chiral term similar to that of Eq. (5.1) and the resultant phase would again be gapped and correspond to the chiral spin liquid discussed in the previous section. The critical value of g reduces as one approaches the isotropic point. For $\lambda/J = 1$, the critical value is much smaller, $g_c \approx 3.4J$. Below this critical value of g_c, the value of h that satisfy the mean-field consistency equations are $h = 0$. In this situation, we are back to the situation with just the XXZ Heisenberg model and the resultant phase at half-filling would be gapless. The expectation values displaced in Fig 5.8 are quite small. The main reason for this is that each chirality operator has a term proportional to S_z. When all the sites are exactly at half-filling this terms is equal to zero and the chiral expectation vanishes. In order to open up a gap, the densities have to be slightly shifted away from zero giving rise to a small non-zero chiral expectation value.

This leaves us with the question of what is the ground state of the XXZ Heisenberg antiferromagnet on the kagome lattice for small $\lambda < 1$ and $g < g_c$. Naively, we would seem to predict that it is equivalent to a

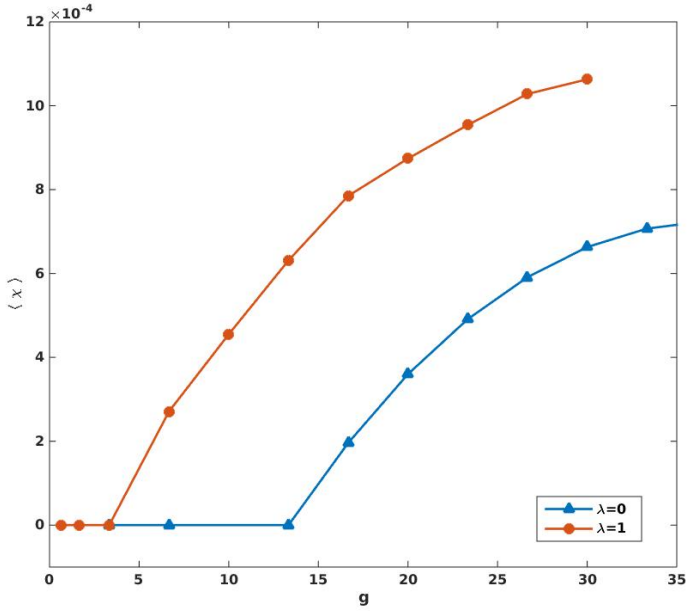

Figure 5.8: (Color online) Expectation value of the chirality operator $\langle\chi\rangle$ plotted as a function of g for $\lambda = 0$, the XY limit (full circles) and $\lambda/J = 1$, the isotropic Heisenberg point (triangles). The mean-field theory critical values are $g_c \approx 13.3J$ in the XY limit, $\lambda = 0$, and $g_c \approx 3.4J$ at the isotropic Heisenberg point, $\lambda/J = 1$.

theory of two massless Dirac fermions which, on many grounds, cannot be the correct answer. In fact, López, Rojo and one of us[49] found the same result in the XY regime of the quantum Heisenberg antiferromagnet *on the square lattice* (which is not frustrated). These authors showed that the naive expectation is actually wrong and the fermions became massive by a process that can be represented as the exchange of Chern-Simons gauge bosons. Due to the stronger infrared behavior of the Chern-Simons gauge fields (compared with , e.g., Maxwell), this exchange term leads to an induced mass term for the Dirac fermions which is infrared finite (but linearly divergent in the ultraviolet). Most significantly the sign of the induced mass term leads to an extra Chern-Simons term which exactly cancelled the term introduced by flux attachment, leaving a parity-invariant Maxwell-type term as the leading contribution to the effective action. Furthermore, in 2+1 dimensions, a Maxwell term is known to be dual to a Goldstone boson. López *et al.* concluded that the ground state of the antiferromagnet on the square lattice in the XY regime has long range order and that the Goldstone mode is just the Goldstone mode of the broken U(1) symmetry of this anisotropic regime. It should be apparent that in our case we can repeat the same line of argument almost verbatim which would suggest that in the XY regime the ground state of the antiferromagnet on the kagome lattice should also have long range order with a broken U(1) symmetry. However, this conclusion is at variance with the best

available numerical evidence which suggests, instead, that the ground state is $\mathbb{Z}_2$ spin liquid (of the Toric Code variety). The resolution of this issue is an open question.

In summary, this mean field theory predicts that beyond some critical value of the ring-exchange coupling constant g, which in this mean-field-theory is typically large, the system is in a chiral spin liquid state with a spontaneously broken time reversal invariance. However, below this critical value the mean field theory seemingly predicts that the Heisenberg antiferromagnet on the kagome lattice is in a phase with two species of gapless Dirac fermions. However this is not (and cannot be) the end of the story. Indeed, the fermions are strongly coupled to the Chern-Simons gauge field which can (and should) change the story. In fact, in Ref. [[49]] a similar result was found even in the case of a square lattice. A more careful analysis revealed that, in that case which is an unfrustrated system, the fermions acquired a mass in such a way that the total effective Chern-Simons gauge action vanished, resulting in a more conventional phase with a Goldstone mode. At present it is unclear what is the fate of the Dirac fermions in the case of the kagome lattice. In fact, most numerical data on the kagome antiferromagnet suggests that it is a $\mathbb{Z}_2$ spin liquid. Whether a $\mathbb{Z}_2$ spin liquid can be reproduced using our methods is an open problem.

Chapter 6

Exact diagonalization study of $m = \frac{2}{3}$ magnetization plateau

In this chapter we study the $m = \frac{2}{3}$ magnetization plateaus in the XXZ Heisenberg antiferromagnet on the kagome lattice using exact diagonalization. The analytic work presented in Ch 4 and 5 indicate the presence of a chiral spin liquid with a spin Hall conductance of $\sigma^s_{xy} = \frac{1}{2}$ in the XY regime of the $\frac{2}{3}$ plateau. The exact diagonalization studies performed in this chapter provide strong evidence of such a chiral spin liquid with the expected characteristics. We will present the results obtained from various clusters of different sizes. Specifically, we analyse the degeneracy structure in the low energy spectrum, use the minimally entangled states to obtain the modular matrices and compute the Chern numbers for the candidate topological states. The modular matrices encode information about the mutual and self-statistics of the effective quasi-particles and the Chern number can be directly related to the spin Hall conductance of the chiral spin liquid. Our results show that modular matrix predicts the existence of semions and we obtain a Chern number of $\frac{1}{2}$ in certain clusters, both of which are consistent with our theoretical predictions for the chiral spin liquid in Ch 4.

6.1 Introduction

6.1.1 Previous work

Several types of spin liquid states have been proposed to exist in quantum antiferromagnets on frustrated lattices[87] (of which the kagome lattice is an example), notably topological states such as the time-reversal invariant $\mathbb{Z}_2$ spin liquid[67, 23, 56] (also known as the Toric Code state[41]) and the (also time reversal-invariant) double-semion model,[27] Dirac spin-liquid states,[64] as well as chiral spin liquid states.[80] In the absence of an external (Zeeman) magnetic field there is good evidence for a time-reversal invariant $\mathbb{Z}_2$ spin liquid being the ground state in extensions of this model on the kagome and other lattices in which further-neighbor antiferromagnetic interactions are also included.[85, 15, 34] On the other hand a chiral spin liquid has been found in the kagome case if a term that breaks the chiral symmetry is added explicitly to the Hamiltonian.[7, 45] There is also evidence of a chiral spin liquid on the kagome lattice in a Heisenberg

antiferromagnet with further neighbor Ising interactions.[32, 30]

In this chapter we will focus on the magnetization plateaus of the spin-$\frac{1}{2}$ quantum Heisenberg antiferromagnet on the kagome lattice. This problem has been studied by several authors with different techniques both analytic and numerical. In the regime of strong Ising anisotropy a strong coupling expansion and exact diagonalization studies have found evidence for ordered phases with various patterns and valence-bond type orders.[9] Exact diagonalization studies of large clusters by Capponi and workers[10] have also been done in a broad range of parameters and have found strong evidence for magnetization plateaus at $\frac{1}{3}$, $\frac{5}{9}$ and $\frac{7}{9}$ of the saturation value, and iPEPs studies of Heisenberg antiferromagnets with spin $S = \frac{1}{2}, 1, \frac{3}{2}$, and 2 also find magnetization plateaus. However both studies interpret the magnetization plateaus they find as evidence for valence bond crystal states or a magnon condensates (the latter being natural in the large S limit).

The analytic studies presented in the previous chapters on the XXZ Heisenberg antiferromagnet (in the regime of XY anisotropy) using flux attachment methods predict that the magnetization plateaus at $\frac{1}{3}$ and $\frac{2}{3}$ are chiral spin liquids. These chiral spin liquids belong in the universality class of the Laughlin state for bosons with spin Hall conductance $\sigma_{xy} = \frac{1}{2}$ for the $\frac{1}{3}$ and $\frac{2}{3}$ plateaus, and $\sigma_{xy} = \frac{2}{3}$ for a plateau at $\frac{5}{9}$ of the saturation value.[43] This state was postulated originally by Kalmeyer and Laughlin[40] as the ground state for the quantum antiferromagnetic spin-$\frac{1}{2}$ Heisenberg model on a triangular lattice.

A very recent exact diagonalization study of the same model (with further neighbor Ising interactions) by Zhu, Gong and Sheng,[89] reports evidence for a chiral spin liquid in the $\frac{1}{3}$ magnetization plateau, consistent with the results of Ref.[[43]], for a range of Ising interactions. Similar Laughlin-type states in magnetization plateaus in other frustrated lattices had been proposed earlier on.[86, 53] An also very recent work on the Hubbard-Haldane honeycomb lattice model in the Mott regime also finds a Laughlin-type state (in close similarity to the results of Bauer and coworkers[7] and to Kumar and coworkers [45] (Ch 5) for the antiferromagnet on the kagome lattice with an explicit time-reversal symmetry breaking term).

6.1.2 Overview of chapter

In this paper, we analyze in detail the properties of the $\frac{2}{3}$-magnetization plateau on the XXZ quantum Heisenberg antiferromagnet in an external magnetic field on the kagome lattice using exact diagonalization. Our main goal is to establish or verify some of the results from Ch 4 where we argued that in the regime of XY anisotropy the $\frac{2}{3}$ magnetization plateau is described by a chiral spin liquid with spin Hall conductance $\sigma_{xy} = \frac{1}{2}$. Notice that the filling fraction of the corresponding FQH state is not equal to the filling fraction of the hard-core bosons (i.e. the magnetization fraction). This topological state of matter state is described by an effective field theory which has the form of a Chern-Simons gauge theory with gauge group $U(1)_k$

with level $k = 2$, the effective field theory of a fractional quantum Hall effect for bosons at filling fraction $\nu = \frac{1}{2}$. For a detailed review see Refs.[[75, 78, 26]]. This is topological state has the following properties: a) it does not break any symmetries aside time reversal and parity, b) it has a two-fold degenerate ground state on a torus (i.e. a system with periodic boundary conditions), c) its elementary excitations are anyons with fractional statistics $\theta = \frac{\pi}{2}$ (hence, they are semions) and fractional "charge" $\frac{1}{2}$, and d) on a system with an open boundary it has a chiral edge state described by a chiral boson conformal field theory (CFT), also at level 2.

The topological properties of the chiral state on a torus are encoded in the modular $\mathcal{S}$ and $\mathcal{U}$ matrices which represent the response of the topological state to modular transformations of the torus.[75] In a general topological state the matrix elements of the modular $\mathcal{S}$-matrix contain the quantum dimensions of the quasiparticles as well as their braiding properties, whereas the modular $\mathcal{U}$ matrix carries the information on the fractional spin, given in terms of the central charge of the associated chiral CFT and the conformal weight of the quasiparticles.[84, 17] In the case of the chiral spin liquid (or the Laughlin state for bosons) there are two linearly independent states on the torus, represented by the identity state 1 and the Laughlin quasiparticle ψ_{qp}. The modular $\mathcal{S}$ and $\mathcal{U}$ matrices are thus given by the 2×2 matrices

$$\mathcal{S} = \frac{1}{\sqrt{2}} \begin{pmatrix} 1 & 1 \\ 1 & -1 \end{pmatrix}, \qquad \mathcal{U} = e^{i\frac{2\pi}{24}1} \begin{pmatrix} 1 & 0 \\ 0 & i \end{pmatrix} \tag{6.1}$$

The factor of $\frac{1}{\sqrt{2}}$ in the $\mathcal{S}$ matrix can be related to the quantum dimension $D = \sqrt{2}$. This also gives an indication of the ground state degeneracy of such a state which is two in this case. The phase of the $\mathcal{S}_{22}$ term can be related to the phase obtained by braiding two quasiparticles around one another. The value of -1 indicates that the effective quasiparticles are semions. The modular $\mathcal{U}$ matrix encodes the value of the central charge (which is $c = 1$ for a field theory expected to describe this phase) and the diagonal entries of the matrix give the phases that the various particles in such a system pick up under an exchange (for bosonic particles the phase would be 1, for fermionic particles it would be -1 and for the semionic quasiparticles it is i ($e^{i\frac{\pi}{2}}$)). Hence, the modular matrices characterise the type of theory and the properties of the effective excitations or quasiparticles in the state.

An efficient way to determine the $\mathcal{S}$ and $\mathcal{U}$ matrices is to construct the so-called minimally entangled states[88] (MES). On a torus the state of the topological system may be on an arbitrary linear combination of its (in this case) two linearly independent ground states. While the entanglement entropies (von Neumann and Rényi) of a cylindrical section of the torus depend on the particular linear combination of these states considered,[17] the MES have the important property that they transform simply under modular

transformations and hence the $\mathcal{S}$ and $\mathcal{U}$ matrices can be constructed using a simple and efficient algorithm of Ref.[[88]].

The $\frac{2}{3}$ plateau corresponds to a higher S_z sector making the ED analysis more feasible as the Hilbert space is more restricted. To this end we will diagonalize the Hamiltonian of the XXZ Heisenberg antiferromagnet on the kagome lattice (discussed in Section 6.2) in clusters with up to 48 spins, with periodic boundary conditions. From these results, presented in Section 6.4, we will try to identify the (nearly) degenerate ground states on the torus and use them to determine the minimally entangled states along two different non-trivial topological cuts. We computed the entanglement spectrum and the second Rényi entropy for different values of the Ising coupling J_z, and the overlap matrix of the MES on two orthogonal sections of the torus. This will allow us to obtain the modular matrices and compare them to the predictions from topological field theory. In Section 6.3 we present the results for the 30, 36 and 42 site clusters. The results in these clusters appear to be more promising and strongly indicate the existence of the chiral spin liquid. In Sec 6.4 we present some results obtained for the 48 site cluster. Here, our observations are a bit contradictory and inconclusive.

6.2 XXZ Heisenberg antiferromagnetic model

The Hamiltonian of the XXZ Heisenberg antiferromagnet in an external magnetic field on the kagome lattice is

$$H_{XXZ} = \sum_{\langle i,j \rangle} J_{xy} \left(S_i^x S_j^x + S_i^y S_j^y \right) + J_z S_i^z S_j^z - h_B \sum_i S_i^z \tag{6.2}$$

Once again, we use ED to analyze these states and focus mainly in the regime of XY anisotropy where we expect the chiral spin liquid to exist. The $m = \frac{2}{3}$ plateau turns out to be the easiest plateau to analyse using ED as it corresponds to a higher S_z sector allowing us to probe larger lattice sizes. Here we will follow the procedures established by other numerical works in analyzing these topological states by attempting to compute the modular $\mathcal{S}$ and $\mathcal{U}$ matrices on the kagome lattice.[30, 90, 13] The structure of these modular matrices can then be used to determine the characteristics of the topological states.

For a lattice with N sites, the total possible magnetization for a spin-$\frac{1}{2}$ system is $N/2$. This implies that

$$m = \frac{2S_z}{N} \tag{6.3}$$

Hence, on a 48-site cluster, the $m = \frac{2}{3}$ plateau corresponds to the $S_z = 16$ sector. The specific 48-site cluster that we will use is shown in Fig 6.10. This lattice has a $\frac{\pi}{3}$ rotational symmetry which will allow us

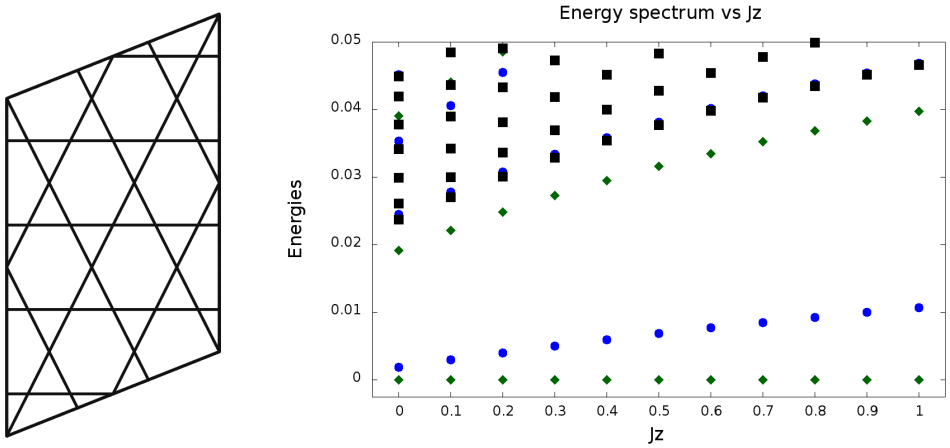

(a) 30 site cluster with periodic boundary conditions

(b) Low energy spectrum as a function of J_z.

Figure 6.1: 30 site cluster and its low energy spectrum as a function of anisotropy parameter J_z. In the energy spectrum plot, the blue circles correspond to the $(0, 0)$ momentum sector and the green diamonds correspond to the $(\pi, 0)$ momentum sector. The other black squares correspond to other momentum sectors with higher energies.

to compute both the modular matrices. [13, 88] In the absence of such a rotational symmetry, one can only compute the modular $\mathcal{S}$-matrix. In most other clusters like the ones presented in Sec 6.3, we will only be able to compute the modular $\mathcal{S}$-matrix as these clusters lack rotational symmetry.

6.3 30 site, 36 site and 42 site clusters

In this section we analyse the 30 site, 36 site and 42 site clusters. We will impose periodic boundary conditions on these clusters and as a result these clusters obey translational symmetry (and the corresponding states will be characterized by momentum quantum numbers). The results obtained for all these clusters are very similar and as a result will be presented together in this section. These clusters are shown in Fig 6.1(a), 6.2(a), 6.3(a) and 6.4. We will first discuss the energy spectrum of each of these clusters. Then, we will specifically focus on the 42 site cluster and continue the analysis by computing the minimally entangled states, modular matrix and Chern numbers only for the case of the 42 site cluster (The analysis for the 30 and 36a site clusters are very similar and will not be repeated.).

6.3.1 30 site cluster

The 30 site cluster is shown in Fig 6.1(a) and the corresponding energy spectrum as a function of J_z is shown in Fig 6.1(b). Note that there appears to be two nearly degenerate states that are well separated from the

higher energy manifold. These two nearly degenerate states belong to the $(0,0)$ and $(\pi,0)$ momentum sectors as show in Fig 6.1(b).

6.3.2 36 site clusters

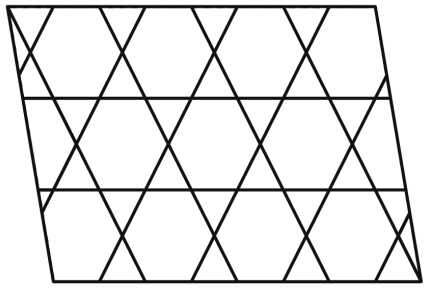

(a) 36a site cluster with periodic boundary conditions.

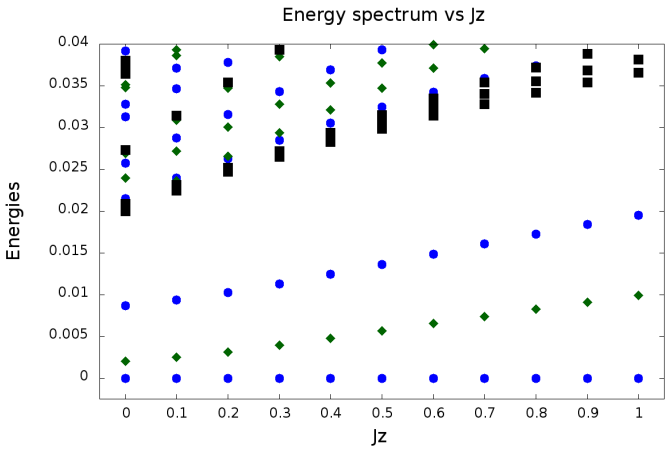

(b) Low energy spectrum as a function of J_z

Figure 6.2: 36a site cluster and its low energy spectrum as a function of anisotropy parameter J_z. Once again, the blue circles correspond to the $(0,0)$ momentum sector and the green diamonds correspond to the $(\pi,0)$ momentum sector. The other black squares correspond to other momentum sectors with higher energies.

Now we take a look at the low energy spectra of two 36 site clusters which we will refer to as 36a and 36d (as in literature [46]). These clusters and their corresponding energy spectra as a function of anisotropy parameter is shown in Fig 6.2 and in Fig 6.3.

Once again note that there appear to be two nearly degenerate states in the energy spectrum for the 36a cluster in Fig 6.2(b) that are well separated from the higher energy states. The case of the more symmetric 36d cluster shown in Fig 6.3(b) is a little harder to interpret. Here the low energy spectrum is dominated my the $(0,0)$ momentum sector and its not obvious whether there is a two or four-fold degeneracy present.

6.3.3 42 site cluster

Finally we present the 42 site cluster which again looks very similar to the 30 site and 36a site clusters. (The 42 site cluster presented here is referred to as the 42b cluster in literature [46].) The detailed analysis presented for the 42 site cluster will also apply to the 30 site and 36a site clusters but will not be reproduced here. The 42 site cluster is shown in Fig 6.4 and the energy spectrum is shown in Fig 6.5.

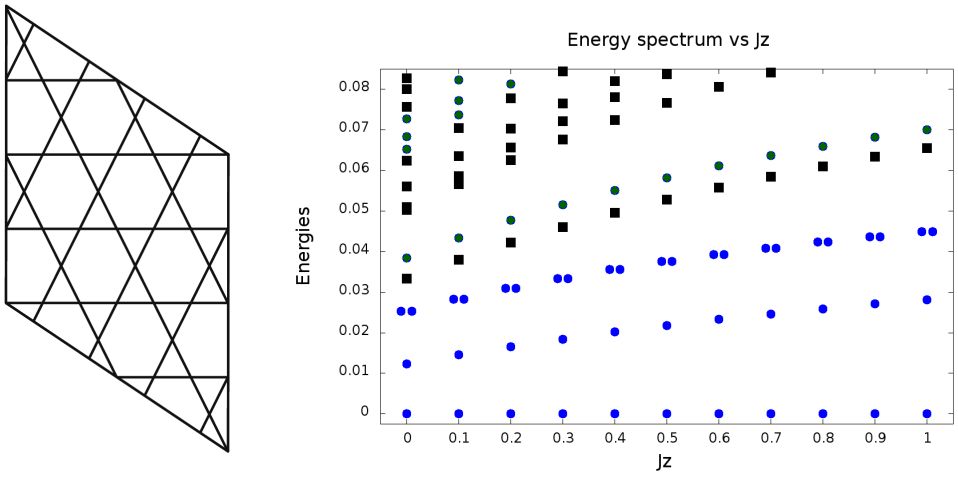

(a) 36d site cluster with periodic boundary conditions.

(b) Low energy spectrum as a function of J_z

Figure 6.3: 36d site cluster and low energy spectrum as a function of anisotropy parameter J_z. Once again, the blue circles correspond to the $(0, 0)$ momentum sector and dominate the low energy manifold. This is common for clusters with higher symmetry.

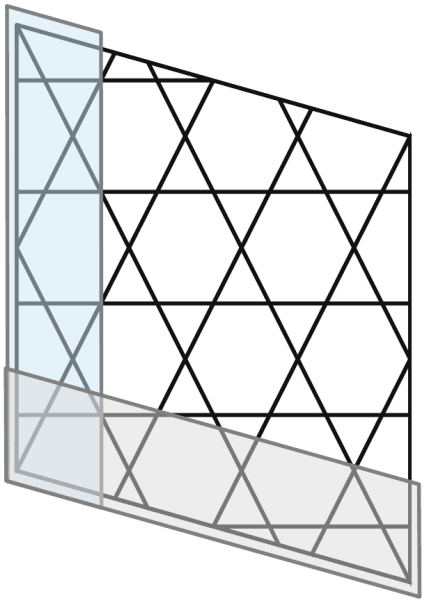

Figure 6.4: 42 site cluster with periodic boundary conditions. The two shaded regions correspond to the two cuts along two different topologically non-trivial directions. These cuts will be used to compute the modular matrices from the minimally entangled states.

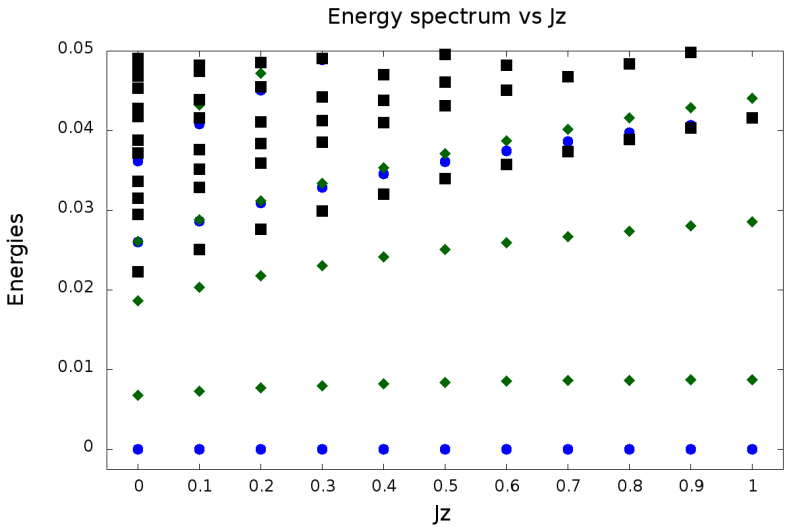

Figure 6.5: Energy spectrum as a function of J_z from 0.0 to 1.0 for the 42 site cluster shown in Fig 6.4. The blue circles and greed diamonds correspond to states in $(0,0)$ and $(\pi,0)$ momentum sector, respectively. The black squares correspond to other momentum sectors that do not contribute to the low energy physics.

The energy spectrum for the 42 site case is shown in Fig 6.5. We note that there is once again a low energy manifold consisting of two states that are separated from the higher energy states (similar to the 30 site and 36a site clusters). The two ground states are in the momentum sectors $(k_x, k_y) = (0,0)$ and $(k_x, k_y) = (\pi, 0)$. We will refer to these states as $|\psi_0\rangle$ and $|\psi_\pi\rangle$, respectively. Note that this ground state degeneracy persists for larger values of J_z and there doesn't appear to be any transition from the XY regime to the Heisenberg point (and beyond) as expected from the mean-field calculations in Ch 4.

6.3.4 Minimally entangled states and modular matrices

In this section we will compute minimally entangled states (MES) for the 42 site cluster (similar analysis on the 30 and 36a clusters yield very similar results). From the MES we will then extract one of the modular matrices using the procedure outlined in other works.[88, 90, 13]. To compute the MES states we will first form linear combinations of the two ground states in the two moementum sectors.

$$|\Psi(c,\phi)\rangle = c\,|\psi_\pi\rangle + \sqrt{(1-c^2)}e^{i\phi}\,|\psi_0\rangle \tag{6.4}$$

where $c \in [0,1]$ and $\phi \in (-\pi, \pi]$ are real parameters and $|\psi_0\rangle$ and $|\psi_\pi\rangle$ refer to the two ground states in the $(0,0)$ and $(\pi,0)$ sectors respectively (see figures 6.1(b), 6.2(b) and 6.5).

Next, we will consider two non-trivial partitions on the torus (as shown in 6.4) in order to compute the MES states. Using the states $|\Psi\rangle$ of Eq.(6.4) one can then construct the reduced density matrix along each

of the two cuts as a function of (c, ϕ). From the reduced density matrix one can then compute the second Rényi entanglement entropy S_2 as follows

$$\begin{aligned} \rho_I =& \mathrm{tr}_{I'} |\Psi\rangle \langle\Psi| \\ S_2 =& -\ln \mathrm{tr} \rho_I^2 \end{aligned} \tag{6.5}$$

where ρ_I is the reduced density matrix for one of the cuts which we label as region I and the trace $\mathrm{tr}_{I'}$ runs over all the sites in region I'. The MES states then correspond to minima in the Rényi entangle entropy in the (c, ϕ) parameter space.

Once again we will look for MES states in the parameter space (c, ϕ) as shown in Eq.(6.4). Due to the lack of rotational symmetry in this system, we will have to compute the MES states along two topologically non-trivial cuts separately. The cuts used for our analysis are shown in Fig 6.4. The MES states obtained for $J_z = 0.0$ are (the full plot for all values of parameters (c, ϕ) is shown in Fig 6.6)

$$\begin{aligned} |\Psi_I^1\rangle =& 0.70 |\psi_0\rangle + 0.71 e^{i3.71} |\psi_\pi\rangle \\ |\Psi_I^2\rangle =& 0.74 |\psi_0\rangle + 0.67 e^{i0.56} |\psi_\pi\rangle \end{aligned} \tag{6.6}$$

along one cut and

$$\begin{aligned} |\Psi_{II}^1\rangle =& |\psi_0\rangle \\ |\Psi_{II}^2\rangle =& |\psi_\pi\rangle \end{aligned} \tag{6.7}$$

along the other cut. Using these MES states one can compute the modular $\mathcal{S}$ matrix to be

$$\mathcal{S} = \begin{pmatrix} 0.71 & 0.70 \\ 0.67 & -0.74 \end{pmatrix} \tag{6.8}$$

Once again, we find that this is in good agreement with the theoretically expected modular matrix in Eq.(6.1). This is again consistent with the prediction that in the XY limit the $m = \frac{2}{3}$ plateau behaves like a chiral spin liquid with quasiparticles that behave like semions.

We would also like to point out that the 30, 36 and 42 site clusters do not exhibit any clear phase transition into an Ising regime. The structure of the modular matrix in Eq. (6.8) remain essentially the same as J_z is increased. This seems to suggest that the smaller (not rotationally symmetric) clusters favor the a chiral spin liquid for a larger parameter range.

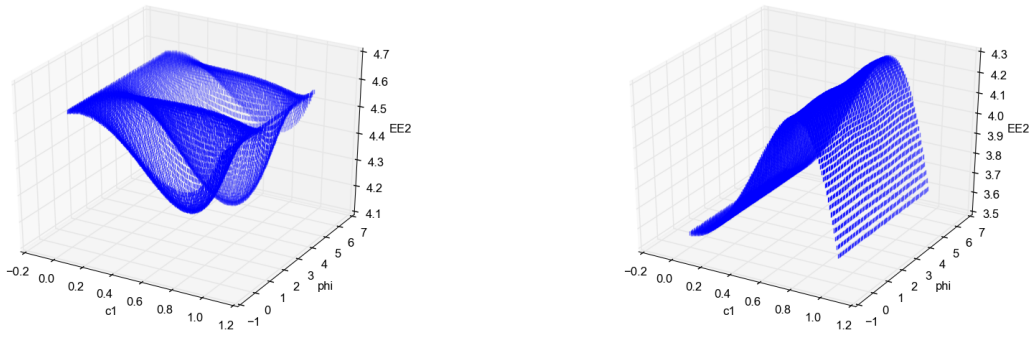

(a) We see two minima along cut I as shown in Eq 6.6

(b) We see two minima for $c = 0, 1$ along cut II as shown in Eq 6.7

Figure 6.6: Plot of entanglement entropy as a function of (c, ϕ) as computed using Eq 6.4 and 6.5

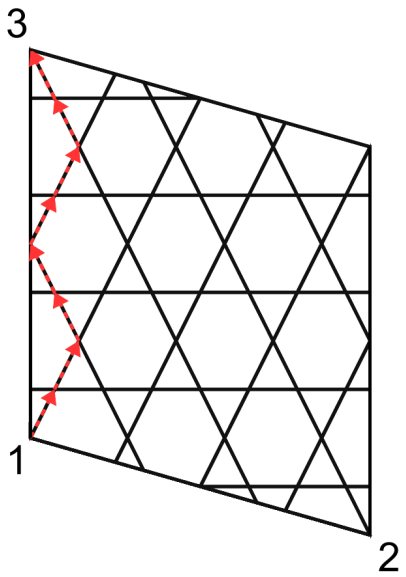

Figure 6.7: 42 site cluster with periodic boundary conditions. In Sec 6.3.5 we will pump flux through this cluster along two topologically non-trivial directions i.e. between points $1 \to 2$ and $1 \to 3$. The path indicated by the red arrows from $1 \to 3$ can be used to determine the fluxes on each of the bonds of the lattice. The sum of all the phases along the indicated path should add up to θ_2.

6.3.5 Flux pumping

In this section we consider the effects of pumping flux through each of the two topologically non-trivial directions on the 42-site cluster. The two non-trivial directions will be chosen to be along the points $1 \rightarrow 2$ and point $1 \rightarrow 3$ in Fig 6.7. As an example a sample path from $1 \rightarrow 3$ is shown using the red arrows in Fig 6.7. The phases on each of the bonds along this path (or any equivalent path) should add up to θ_2. We will choose to uniformly distribute the fluxes along each of the bonds in order to achieve this. A similar path can be chosen along the paths connecting $1 \rightarrow 2$ such that the phases again add up to θ_1. In order to perform the above flux pumping we will use the below modified Hamiltonian when performing the exact diagonalization and extract the corresponding wave functions for each value of θ_1 or θ_2.

$$H_{XXZ} = \sum_{\langle i,j \rangle} \frac{J_{xy}}{2} \left(S_i^+ e^{A_{ij}} S_j^- + h.c. \right) + J_z S_i^z S_j^z - h_B \sum_i S_i^z \tag{6.9}$$

where A_{ij} represents the phase in the bond connecting sites i and j. Recalling our definition of the fluxes in Ch 2 (see Fig 2.1. we can establish the below relationship for the path from $1 \rightarrow 3$ shown in Fig 6.7 to be

$$\begin{aligned} \theta_2 &= 4A_2 + 4A_3 \\ A_1 &= A_2 - A_3 \end{aligned} \tag{6.10}$$

Along points $1 \rightarrow 2$, we plot the ground state energy spectrum as a function of the flux (θ_1) from 0 to 2π as shown in Fig 6.8(a). A similar plot for pumping of flux along $1 \rightarrow 3$ is shown in Fig 6.8(b) as a function of θ_2 from 0 to 2π. The $(0,0)$ state and $(7,0)$ state labels in Fig 6.8 refer to the momentum sectors of the two ground states i.e. they refer to the $|\psi_0\rangle$ and $|\psi_\pi\rangle$ state respectively (see Eq 6.4). Along the θ_2 direction we see that the two topological ground states flip under flux pumping. This is characteristic of topological ground states where pumping flux through one of the non-trivial loops on a torus allows you to go from one topological sector to the another as shown in 6.8(b).

6.3.6 Chern number

Finally, we also compute the chern numbers of the two topological ground states $|\psi_0\rangle$ and $|\psi_\pi\rangle$. We will compute the Chern number using the below expression

$$C = \frac{1}{2\pi} \int B(\theta_1, \theta_2) d\theta_1 d\theta_2 \tag{6.11}$$

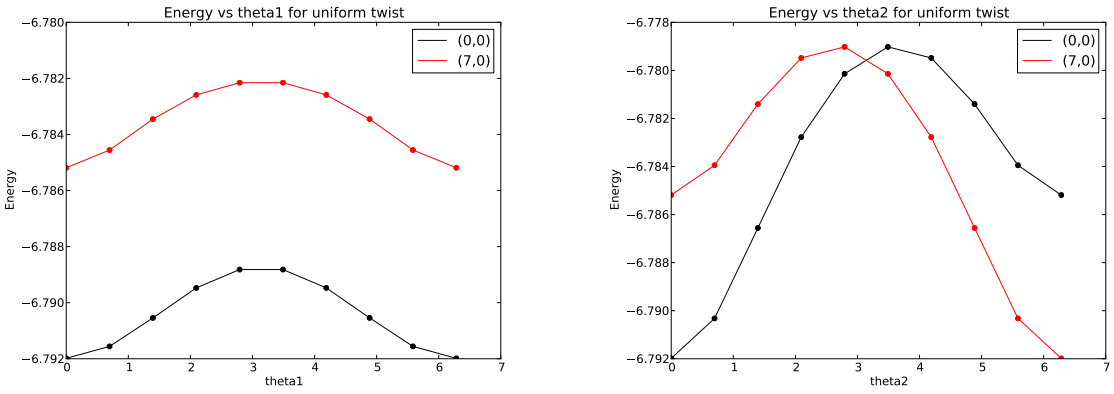

(a) Flux pumping along points $1 \to 2$ in Fig 6.7

(b) Flux pumping along points $1 \to 3$ in Fig 6.7

Figure 6.8: The above plots track the energies of the lowest two (topologically degenerate) ground states as a function of flux (θ_1 and θ_2) along two topologically non-trivial directions. The $(0,0)$ state and $(7,0)$ state refer to the $|\psi_0\rangle$ and $|\psi_\pi\rangle$ state respectively (see Eq 6.4). Along θ_2 direction we observe observe that the two ground states flip under flux pumping which is characteristic for topologically degenerate states.

where B corresponds to the berry curvature and θ_1 and θ_2 correspond to the flux that is being inserted along the two non-trivial topological directions as in Sec 6.3.5. A numerical way to compute this Chern number is to create a grid of points in the (θ_1, θ_2) space where $\theta_1 \in (0, 2\pi)$ and $\theta_2 \in (0, 2\pi)$. On each point of the grid one can then compute the eigenvector $|\psi(\theta_1, \theta_2)\rangle$. Then, the berry curvature at each point can be computed as follows

$$\begin{aligned} B_{(\theta_1,\theta_2)} = \text{Log}\{ &\langle\psi(\theta_1,\theta_2)|\psi(\theta_1+\delta_1,\theta_2)\rangle \langle\psi(\theta_1+\delta_1,\theta_2)|\psi(\theta_1+\delta_1,\theta_2+\delta_2)\rangle \\ &\times \langle\psi(\theta_1+\delta_1,\theta_2+\delta_2)|\psi(\theta_1,\theta_2+\delta_2)\rangle \langle\psi(\theta_1,\theta_2+\delta_2)|\psi(\theta_1,\theta_2)\rangle \} \end{aligned} \tag{6.12}$$

which is essentially computing the overlaps between wave functions along a closed loop in the (θ_1, θ_2) grid. The δ_1 and δ_2 in the above expression refer to the grid spacing along the θ_1 and θ_2. The result of such a computation is shown in Fig 6.9. The plot shows the contribution to the Chern number in Eq (6.11) as a function of θ_1 and θ_2. The main contribution comes from a single region in the grid and add amount to exactly a factor of 0.5. This holds true for both the nearly degenerate ground states $|\psi_0\rangle$ and $|\psi_\pi\rangle$.

Hence, we find that both the nearly degenerate ground states give rise to the same Chern number of a $\frac{1}{2}$ which is exactly what the spin Hall conductance of a chiral spin liquid with $\sigma_{xy} = \frac{1}{2}$ should be.

This concludes our analysis of the 42 site cluster. Next, we will present some results for the 48 site cluster which are not as conclusive.

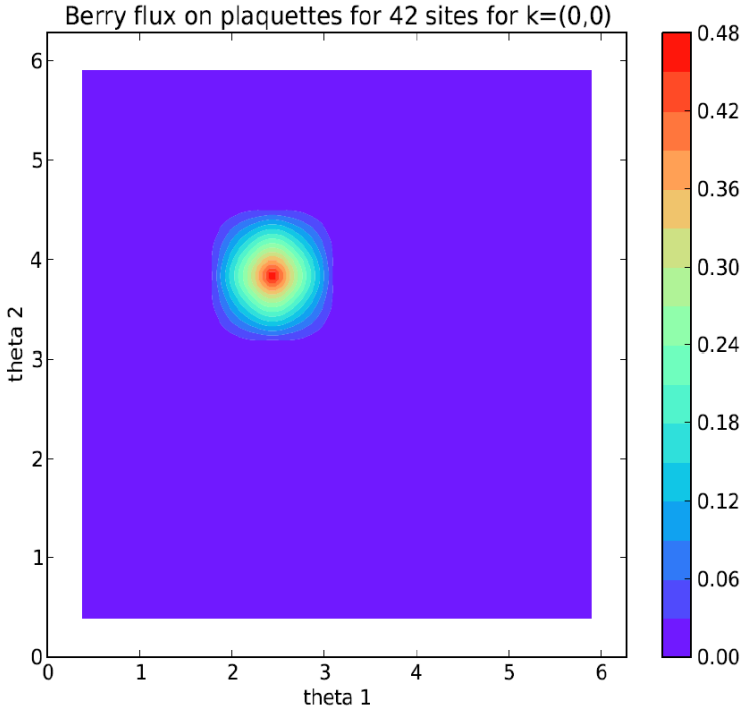

Figure 6.9: Berry flux as a function of θ_1 and θ_2 for the ground state $|\psi_0\rangle$. We observe that there is essentially one point on the entire grid that contributes to total Chern number. This region is marked by the bright red spot and its berry flux essentially equal to 0.5.

6.4 48-site cluster

In this section, we present the results that were obtained on the more symmetric 48-site cluster with periodic boundary conditions (torus geometry). The cluster is shown in Fig 6.10. The degeneracy structure and other nice features present in the smaller clusters changes a bit on the 48-site cluster. Some of the evidence here is a bit contradictory and inconclusive. As a result I will just present our analysis without drawing any major conclusions. Our main motivation for considering this cluster was that the additional rotational symmetry that exists in this cluster can be used to determine both modular matrices.

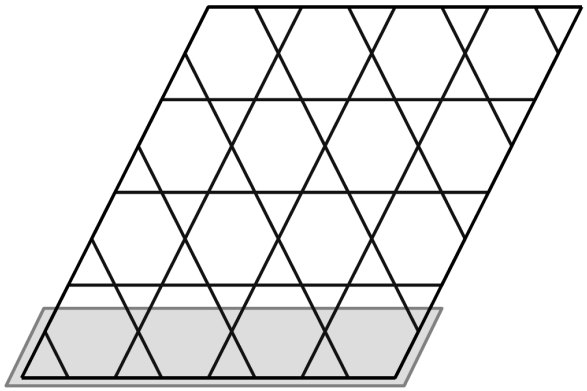

Figure 6.10: 48 site cluster (with periodic boundary conditions) used for ED. The two dotted lines indicate the two cuts that were used to compute the minimally entangled states.

The energy spectrum for the 48-site case is shown in Fig 6.11 for J_z from 0.0 to 1.0. The first thing to note is that there are three near degenerate ground states that are well separated from the higher excited states. Secondly, two of these ground states are exactly degenerate and there appears to be a phase transition around $J_z \approx 0.2$ where the two levels switch. These three low energy states all lie in the $(k_x, k_y) = (0, 0)$ momentum sector. We will label these three states as $|\psi^{(1a)}\rangle$, $|\psi^{(1b)}\rangle$ and $|\psi^{(2)}\rangle$ where $|\psi^{(1a)}\rangle$ and $|\psi^{(1b)}\rangle$ refer to the two exactly degenerate ground states.

As the 48-site cluster has sixty degree rotational symmetry we will choose linear combinations of $|\psi^{(1a)}\rangle$ and $|\psi^{(1b)}\rangle$ that are eigenstates of the $\frac{\pi}{3}$ rotation operator, $R_{\frac{\pi}{3}}$, on the 48-site cluster. The two exactly degenerate ground states can now be labelled as $|\psi_\pm\rangle$ and $|\psi^{(2)}\rangle$ is equivalent to a $|\psi_0\rangle$ state. In this new rotation basis, the action of the rotation operator is given as

$$\begin{aligned} R_{\frac{\pi}{3}} |\psi_\pm\rangle &= \lambda_\pm |\psi_\pm\rangle \\ R_{\frac{\pi}{3}} |\psi_0\rangle &= \lambda_0 |\psi_0\rangle \end{aligned} \tag{6.13}$$

where $\lambda_{\pm} = e^{\pm i\frac{2\pi}{3}}$ and $\lambda_0 = 1$.

Further, the two exactly degenerate states are now complex conjugates of one another i.e. $|\psi_+\rangle = |\psi_-\rangle^*$. Recall here that the goal was to search for a chiral spin liquid with $\sigma_{xy} = \frac{1}{2}$ in the XY regime as suggested by the analytic work on the same model. [43] Such a state should exhibit a two fold ground state degeneracy on a torus. However, the two exactly degenerate states ($|\psi_{\pm}\rangle$) are complex conjugates of one another and are unlikely to form the two topological states predicted in theory.

Further, we believe that in such a system the true degeneracy in a numerical simulation should actually be four i.e. two copies of left and right chiral states as this symmetry is not explicitly broken on this cluster. This implies that the true ground state topological manifold should actually consist of the two lowest $|\psi_+\rangle$ and two lowest $|\psi_-\rangle$ states in the $(0,0)$ momentum sector. These states are represented using the green down triangles and the red up triangles in the energy spectrum shown as a function of anisotropy along the J_z direction in Fig 6.11. We would like to point out that the energy spectra of the 48 site (nor the 30, 36a or 42 smaller clusters) does not appear to reflect this fact. But due to the strong evidence for a chiral spin liquid presented in the previous section, we will try to proceed with the analysis for now.

We have performed various analysis by trying to construct the modular matrices using the two left chiral and right chiral states in this manifold. The calculation here is a bit difficult when computing the minimally entangled states as we only find one minima in the (c, ϕ) manifold and cannot reliably compute the modular matrices in this case. Further, there is also the spurious $|\psi_0\rangle$ state lurking close to the two exactly degenerate states which is represented by the blue circle in the energy spectrum shown in Fig 6.11. Once again we believe that this state does not play a role in the topological manifold. (On a related note H.Changlani et. al. have discovered an exactly solvable point at $J_z = -\frac{1}{2}$ which has a large ground state degeneracy. They have some preliminary work that might be able to explain the existence of such a spurious state at the XY point.) I will not proceed any further at this point and note that more work will have to be done to completely understand and interpret the observations on the 48 site cluster.

The other distinct characteristic to the 48 site cluster is that there appears to be a level crossing between the states represented by the triangles (the possible topological states) and the blue circle (expected to be non-topological) around $J_z = 0.2$ which is indicative of a possible phase transition between the XY and Ising regimes. Note that in the cases of the smaller clusters no such transition was detected which once again indicates that these topological phases are very sensitive to the geometry for small cluster sizes and there are significant differences depending on which clusters one chooses to analyse.

In summary, we believe that we have performed a systematic analysis of the $m = \frac{2}{3}$ plateau on the Kagome lattice for various cluster sizes. We have shown that there exists some strong evidence for the chiral

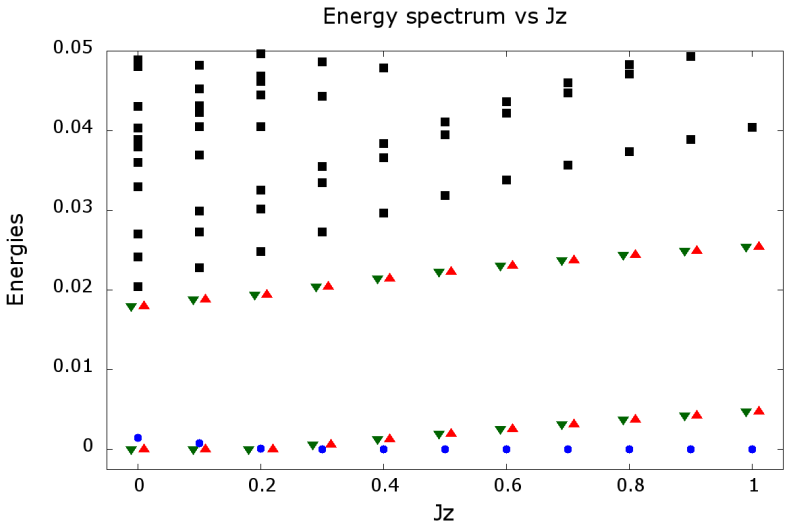

Figure 6.11: Energy spectrum as a function of J_z from 0.0 to 1.0. The lower energy manifold consists of three states that are well separated from the higher states which are all in the $(k_x, k_y) = (0, 0)$ momentum sector. All the energies indicated are in units of J_{xy} which has been set to 1 for convenience. The red up triangle, green down triangle and blue circle refer to states with eigenvalues λ_+, λ_- and λ_0 under the rotation operator, respectively. The black squares correspond to states in other momentum sectors and do not contribute to the low energy physics.

spin liquid predicted by the analytic predictions based on the ground state degeneracy structure, modular matrices and chern number calculations. However, we also observe that these results are sensitive to the type and geometry of the cluster being analysed leading to some inconclusive observations for the 48 site cluster.

Chapter 7

Conclusions

In this paper, we have analyzed the nearest-neighbor spin-1/2 XXZ Heisenberg antiferromagnet on the Kagome lattice using a two dimensional flux attachment transformation that maps spins (hard-core bosons) to fermions coupled to a Chern-Simons gauge field. This transformation relied on being able to write down a lattice version of the Chern-Simons term on the Kagome lattice. Previously such a mapping had only been done on the square lattice. [24], [19] Here, we explicitly showed that a similar mapping can also be performed on the Kagome lattice in Ch 2 and that there are in fact a large class of planar 2D lattices where such a mapping is valid provided they satisfy certain key constraints in Ch 3.

We used this model to study the various magnetization plateaus that can arise at the mean-field level in Ch 4. At the mean-field level these states had integer Chern numbers and hence corresponded to integer quantum Hall type states. More specifically, in the case of the $\frac{1}{3}$ magnetization plateau at the mean-field level we obtained a state with Chern number one in the XY regime. However, the inclusion of fluctuations gives rise to an effective Chern-Simons theory that predicts a fractional quantum Hall state of bosons with a spin Hall conductivity of $\sigma^s_{xy} = \frac{1}{2}\frac{1}{2\pi}$, thus altering the mean-field physics drastically. The excitations of this plateau are anyons with fractional spin and statistical angle $\frac{\pi}{2}$ (i.e. the effective quasiparticles are now semions). This plateau state is a topological state with two-fold degeneracy on a torus. On a disk geometry it supports a chiral edge state (with compactification radius $\sqrt{2}$). In the Ising regime, the effective Chern-Simons theory just transmutes the fermions back to the original bosons and reduces to earlier results. In such a situation our theory doesn't select a specific state besides the fact the spins just behave like the original hard-core bosons. We also searched for other possible magnetization plateau states. The other two prominent ones we found are in the cases of the $\frac{2}{3}$ and $\frac{5}{9}$ magnetization plateaus. The $\frac{2}{3}$ plateau is essentially equivalent to the $\frac{1}{3}$ plateau in terms of its topological characteristics even though there are some differences in the band structure at the mean-field level. The $\frac{5}{9}$ plateau turns out to be equivalent to the first Jain state for bosons with (spin) Hall conductance of $\sigma^s_{xy} = \frac{2}{3}\frac{1}{2\pi}$. Its excitations are anyons with statistical angle $\frac{\pi}{3}$. Such a state has a three-fold ground state degeneracy on a torus and supports two chiral chiral gapless edge states on a disk geometry. The gapless edge state of both the $\frac{1}{3}$ and in the $\frac{5}{9}$ plateaus there should give a

linear temperature-dependent contribution to the heat capacity.

In the absence of an external magnetic field, the flux attachment transformation that we use here, at the level of mean field theory, naively maps the kagome antiferromagnet onto a system of two species of massless Dirac fermions. Since this state is not gapped, the spectrum (and even the quantum numbers of the states) is not protected by the effects of fluctuations. Of all the fluctuations that are present, only the long range fluctuations of the Chern-Simons gauge field are (perturbatively) relevant. Indeed, this problem arises even in the simpler problem of the Heisenberg antiferromagnet on the square lattice, and López *et al.*[49] showed, using a non-trivial mapping, that already at the one-loop level the spectrum changes from "free" massless Dirac fermions to the conventional Néel antiferromagnet with XY anisotropy (easy plane). In Sec. 5.3 we derived an effective field theory for the kagome antiferromagnet at zero field and, not surprisingly, found a state which naively has two species of massless Dirac fermions. A simple minded application of the same line of argument would also predict an easy-plane antiferromagnet which has a Goldstone mode (in the XY regime). This however is not consistent with the best numerical data which shows no long range order but a topological $\mathbb{Z}_2$ state. How to reconcile these two scenarios is an open question.

On the other hand, we should note that, contrary to the case of non-relativistic fermions, a theory of massless Dirac fermions coupled to a Chern-Simons gauge theory is non-trivial. While in a massive phase this coupling should also amount to change in statistics, the massless case is much less understood. In fact, the only case which a related problem is understood[28, 1, 50] is the case in which the gauge fields have a gauge group $U(N)$ and the Chern-Simons action has level k. In the limit in which $N \to \infty$ and $k \to \infty$ (with $\frac{N}{k}$ fixed), this problem maps onto a Wilson-Fisher fixed point of a scalar coupled to a Chern-Simons gauge theory with gauge group $U(k)$ at level N (with the same ratio $\frac{N}{k}$). Away from this regime not much is known. In this large N and large k limit, the system remains conformally invariant (and hence critical). Our present understanding of the kagome antiferromagnets suggests that for small enough N the system should become gapped and conformal symmetry should be spoiled.

Along with presenting the process of developing the flux attachment transformation for the case of the Kagome lattice, we also present the rules for when such a flux attachment transformation can be performed on a generic lattice in Ch 3. Essentially, we prove that the Chern-Simons gauge theory can be discretized for generic planar lattice on an arbitrary 2D closed orientable manifold as long as a local vertex-face correspondence can be defined on the graph. This condition is also necessary, if we want the theory to be nonsingular and to preserve some key properties of the Chern-Simons gauge theory. In particular, we showed that the gauge invariance of the discretized theory requires that the local vertex-face correspondence to be strictly enforced. In such cases we also show that the resulting discretized version of the Chern-Simons gauge theory

mimics many of the topological characteristics of the continuum version. The square, Kagome and dice lattices all satisfy the local face-vertex correspondence condition. However, other lattices such as the triangular and honeycomb lattices do not and the method described here cannot be applied directly to these situations.

Next in Ch 5 we also investigated the occurrence of chiral spin liquid phases in the nearest neighbor XXZ Heisenberg Hamiltonian (with and without an external magnetic field) on the kagome lattice and in the presence of various perturbations: a) a chirality symmetry breaking term, b) Dzyaloshinkii-Moriya interaction (only in the XY limit), and c) ring-exchange interactions. At the mean-field level, we found that in the first two cases these interactions open up a gap in the spectrum and lead to phases with non-trivial Chern numbers (analogous to an integer quantum Hall state) in the XY limit, $\frac{\lambda}{J} \lesssim 1$. When the effects of fluctuations are included, we again find that these states actually correspond to fractional quantum Hall states for bosons with a spin Hall conductivity of $\sigma^s_{xy} = \frac{1}{2}$ (similar to the cases of the $\frac{1}{3}$ and $\frac{2}{3}$ magnetization plateaus observed earlier in Ch 4). This chiral spin liquid state survives for larger values of the chirality term but for larger values of the Dzyaloshinskii-Moriya term, the chiral spin liquid state vanishes. Our results qualitatively agree with those obtained in a recent numerical study using the same model.[6]

We also considered the effects of adding ring-exchange term on the bowties of the kagome lattice and found that, provided the coupling constant is larger than a critical value (which depends on parameters, e.g. the value of the Ising interaction), time-reversal symmetry is spontaneously broken and results in a topological state similar chiral spin liquid state. However since the critical couplings that we find are rather large, ranging from $\frac{g}{J} \simeq 13.3$ in the XY limit to $\frac{g}{J} \simeq 3.4$ at the isotropic point, we cannot exclude that other phases may also play a role. In particular, we have not explored the possible existence of topological phases with nematic order.[14]

In the earlier work, we showed that in the presence of a magnetic field, the nearest neighbor Heisenberg Hamiltonian gives rise to magnetization plateaus at $m = \frac{1}{3}$, $\frac{2}{3}$ and $\frac{5}{9}$ in the XY limit.[43] We also found that some of these same plateaus survive with the inclusion of the chirality and Dzyaloshinkii-Moriya terms. In addition we also find another plateau at magnetization $m = \frac{1}{9}$ with a spin Hall conductivity $\sigma^s_{xy} = \frac{2}{3}$ for certain ranges of parameters.

In the very last chapter Ch 6, we also present some numerical evidence for the existence of the $\frac{2}{3}$ being a chiral spin liquid state with $\sigma^s_{xy} = \frac{1}{2}$. Our results are based on exact diagonalization calculations of the nearest neighbour Heisenberg model in the presence of an external magnetic field in the XY limit. We consider relatively large systems from an exact diagonalization perspective which is possible because of the higher magnetization value. We present results for various clusters detailing the behavior of the low energy spectrum and by computing the modular matrices when possible to provide evidence of a chiral spin liquid

with semionic quasiparticles as predicted from the flux attachment transformation calculations in Ch 4. We also compute the Chern numbers of the possible topological states and show that they match the expected spin Hall conductance of a $\frac{1}{2}$ for the chiral spin liquid on some clusters. We would also like to point out that the behaviour of the spectrum and the minimally entangled states are very sensitive to the type of cluster and the number of sites in the cluster. Though we find the above strong evidence for a chiral spin liquid in some clusters, there are some other clusters were the interpretation is not so straightforward and the results are inconclusive. This leads us to conclude that finite size effects play a significant role here and that more work would have to be done to conclusively establish the presence of such a chiral spin liquid in such a system.

Other works focusing on the $\frac{1}{3}$ plateau have found a similar chiral spin liquid but with the inclusion of additional next and next-next nearest neighbor interactions. [89] We would like to remark that such interactions possibly stabilize the chiral spin liquid state that we observe. At least at the mean-field level it can be shown that such type of interactions help to widen the gap resulting in a stronger chiral spin liquid phase. However, the full model (with next and next-next neighbour interactions) with fluctuations cannot be treated under our flux attachment transformations as such a system would violate the one-to-one correspondence between sites and plaquettes on the lattice.

Chapter 8

References

[1] O. Aharony, G. Gur-Ari, and R. Yacoby. Correlation Functions of Large N Chern-Simons-Matter Theories and Bosonization in Three Dimensions. *JHEP-J. High Energy Phys.*, 1212:028, 2012.

[2] Daniel P. Arovas and Assa Auerbach. *Phys. Rev. B*, 38:316, 1988.

[3] L. Balents, M. P. A. Fisher, and S. M. Girvin. Fractionalization in an easy-axis kagome antiferromagnet. *Phys. Rev. B*, 65:224412, May 2002.

[4] Leon Balents. Spin liquids in frustrated magnets. *Nature*, 464:199, 2010.

[5] G. Baskaran, Z. Zou, and P.W. Anderson. *Solid State Comm.*, 63:973, 1987.

[6] B. Bauer, L. Cincio, B. P. Keller, M. Dolfi, G. Vidal, S. Trebst, and A. W. W. Ludwig. Chiral spin liquid and emergent anyons in a Kagome lattice Mott insulator. *Nat. Commun.*, 5:5137, 2014.

[7] B. Bauer, L. Cincio, B.P. Keller, M. Dolfi, G. Vidal, S. Trebst, and A.W.W. Ludwig. Chiral spin liquid and emergent anyons in a kagome lattice mott insulator. *Nat. Commun.*, 5:5137, 2014.

[8] Norman Biggs. *Algebraic Graph Theory*. Cambridge University Press, Cambridge, UK, 1974.

[9] D. C. Cabra, M. D. Grynberg, P. C. W. Holdsworth, A. Honecker, P. Pujol, J. Richter, D. Schmalfuß, and J. Schulenburg. Quantum kagome antiferromagnet in a magnetic field: Low-lying non-magnetic excitations versus valence-bond crystal order. *Phys. Rev. B*, 71:144420, 2005.

[10] Sylvain Capponi, Oleg Derzhko, Andreas Honecker, Andreas M. Läuchli, and Johannes Richter. Numerical study of magnetization plateaux in the spin-1/2 kagome Heisenberg antiferromagnet . *Phys. Rev. B*, 88:144416, 2013.

[11] Gia-Wei Chern and R. Moessner. *Phys. Rev. Lett.*, 110:077201, Feb 2013.

[12] Andrey Chubukov. *Phys. Rev. Lett.*, 69:832–835, Aug 1992.

[13] L. Cincio and G. Vidal. Characterizing topological order by studying the ground states on an infinite cylinder. *Phys. Rev. Lett.*, 110:067208, Feb 2013.

[14] Bryan K. Clark, Jesse M. Kinder, Eric Neuscamman, Garnet Kin-Lic Chan, and Michael J. Lawler. Striped spin liquid crystal ground state instability of kagome antiferromagnets . *Phys. Rev. Lett.*, 111:187205, 2013.

[15] Stefan Depenbrock, Ian P. McCulloch, and Ulrich Schollwöck. Nature of the spin-liquid ground state of the $s = 1/2$ heisenberg model on the kagome lattice. *Phys. Rev. Lett.*, 109:067201, Aug 2012.

[16] P. A. M. Dirac. *Lectures in Quantum Field Theory*. Academic Press, New York, NY, 1966.

[17] S. Dong, E. Fradkin, R. G. Leigh, and S. Nowling. Topological Entanglement Entropy in Chern-Simons Theories and Quantum Hall Fluids. *JHEP-J. High Energy Phys.*, 05:016, 2008.

[18] M. Elhajal, B. Canals, and C. Lacroix. Symmetry breaking due to dzyaloshinsky-moriya interactions in the kagomé lattice. *Phys. Rev. B*, 66:014422, Jul 2002.

[19] D. Eliezer and G. W. Semenoff. Anyonization of Lattice Chern-Simons theory. *Ann. Phys.*, 217:66, 1992.

[20] D. Eliezer and G. W. Semenoff. Anyonization of lattice chern-simons theory. *Annals of Physics*, 217(1):66–104, 1992.

[21] D. Eliezer and G.W. Semenoff. *Phys. Lett. B*, 286:118, 1992.

[22] G. Evenbly and G. Vidal. Frustrated antiferromagnets with entanglement renormalization: ground state of the spin-1/2 Heisenberg model on a kagome lattice. *Phys. Rev. Lett.*, 104:187203, 2010.

[23] E. Fradkin and S. H. Shenker. Phase diagrams of lattice gauge theories with Higgs fields. *Phys. Rev. D*, 19:3682, 1979.

[24] Eduardo Fradkin. Jordan-Wigner transformation for Quantum-Spin Systems in Two Dimansions and Fractional Statistics. *Phys. Rev. Lett.*, 63:322, 1989.

[25] Eduardo Fradkin. Superfluidity of the lattice anyon gas and topological invariance. *Phys. Rev. B*, 42:570, 1990.

[26] Eduardo Fradkin. *Field Theories of Condensed Matter Physics, Secoond Edition.* Cambridge University Press, Cambridge, UK, 2nd edition, 2013.

[27] M. Freedman, C. Nayak, K. Shtengel, and K. Walker. A Class of P,T-Invariant Topological Phases of Interacting Electrons. *Ann. Phys.*, 310:428, 2004.

[28] S. Giombi, S. Minwalla, S. Prakash, S. P. Trivedi, and S. R. Wadia. Chern-Simons Theory with Vector Fermion Matter. *Eur. Phys. J. C*, 72:2112, 2012.

[29] Shou-Shu Gong, Wei Zhu, and D. N. Sheng. Emergent Chiral Spin Liquid: Fractional Quantum Hall Effect in a Kagome Heisenberg Model. *Sci. Rep.*, 4:6317, 2014.

[30] Shou-Shu Gong, Wei Zhu, and D. N. Sheng. Emergent chiral spin liquid: Fractional quantum hall effect in a kagome heisenberg model. *Sci. Rep.*, 4:6317, 2014.

[31] Tian-Heng Han, Joel s. Helton, Shaoyan Chu, Daniel G. Nocera, José A. Rodriguez-Rivera, Collin Broholm, and Young S. Lee. Fractionalized excitations in the spin-liquid state of a kagome-lattice antiferromagnet . *Nature*, 492:406, 2012.

[32] Yin-Chen He, D. N. Sheng, and Yan Chen. Chiral Spin Liquid in a Frustrated Anisotropic Kagome Heisenberg Model. *Phys. Rev. Lett.*, 112:137202, 2014.

[33] C.L. Henley and E.P. Chan. *Journal of Magnetism and Magnetic Materials*, 140144, Part 3(0):1693 – 1694, 1995. International Conference on Magnetism.

[34] Yasir Iqbal, Federico Becca, and Didier Poilblanc. Projected wave function study of Z2 spin liquids on the kagome lattice for the spin-1/2 quantum Heisenberg antiferromagnet . *Phys. Rev. B*, 84:020407, 2011.

[35] S. V. Isakov, M. B. Hastings, and R. G. Melko. Topological entanglement entropy of a Bose-Hubbard spin liquid. *Nature Physics*, 7:772, 2011.

[36] J. K. Jain. Composite-fermion approach for the fractional quantum Hall effect. *Phys. Rev. Lett.*, 63:199, 1989.

[37] J. K. Jain. Microscopic Theory of the Fractional Quantum Hall Effect. *Adv. Phys.*, 41:105, 1992.

[38] H. C. Jiang, H. Yao, and L. Balents. Spin Liquid Ground State of the Spin-1/2 Square J_1-J_2 Heisenberg Model . *Phys. Rev. B*, 86:024424, 2012.

[39] Hong-Chen Jiang, Zhenghan Wang, and Leon Balents. Identifying topological order by entanglement entropy. *Nat Phys*, 8:902, 2012.

[40] V. Kalmeyer and R. B. Laughlin. *Phys. Rev. Lett.*, 59:2095, 1987.

[41] A. Yu. Kitaev. Fault-tolerant quantum computation by anyons. *Annals of Physics*, 303:2, 2003.

[42] J. Kogut and L. Susskind. Hamiltonian formulation of Wilson's lattice gauge theories. *Phys. Rev. D*, 11:395, 1975.

[43] K Kumar, K Sun, and E Fradkin. Chern-Simons theory of magnetization plateaus of the spin-$\frac{1}{2}$ quantum XXZ Heisenberg model on the kagome lattice. *Phys. Rev. B*, 90:174409, Nov 2014.

[44] Krishna Kumar, Kai Sun, and Eduardo Fradkin. Chern-Simons theory of magnetization plateaus of the spin-$\frac{1}{2}$ quantum XXZ Heisenberg model on the kagome lattice. *Phys. Rev. B*, 90:174409, 2014.

[45] Krishna Kumar, Kai Sun, and Eduardo Fradkin. Chiral spin liquids on the kagome lattice. *Phys. Rev. B*, 92:094433, 2015.

[46] Andreas M. Läuchli, Julien Sudan, and Erik S. Sørensen. Ground-state energy and spin gap of spin-$\frac{1}{2}$ kagomé-heisenberg antiferromagnetic clusters: Large-scale exact diagonalization results. *Phys. Rev. B*, 83:212401, Jun 2011.

[47] R. B. Lehoucq, D. C. Sorensen, and C. Yang. Arpack users guide: Solution of large scale eigenvalue problems by implicitly restarted arnoldi methods., 1997.

[48] Ana López and Eduardo Fradkin. *Phys. Rev. B*, 44:5246, 1991.

[49] Ana López, A. G. Rojo, and Eduardo Fradkin. Chern-Simons theory of the anisotropic quantum Heisenberg antiferromagnet on a squere lattice. *Phys. Rev. B*, 49:15139, 1994.

[50] J. Maldacena and A. Zhiboedov. Constraining Conformal Field Theories with a Higher Spin Symmetry. *J. Phys. A: Math. Theor.*, 46:214011, 2013.

[51] J. B. Marston and C. Zeng. Spinpeierls and spinliquid phases of kagom quantum antiferromagnets. *Journal of Applied Physics*, 69(8):5962–5964, 1991.

[52] Laura Messio, Bernard Bernu, and Claire Lhuillier. The kagome antiferromagnet: a chiral topological spin liquid ? . *Phys. Rev. Lett.*, 108:207204, 2012.

[53] G. Misguich, Th. Jolicoeur, and S. M. Girvin. Magnetization plateaus of $SrCu_2(BO_3)_2$ from a Chern-Simons theory. *Phys. Rev. Lett.*, 87:097203, 2001.

[54] G. Misguich, D. Serban, and V. Pasquier. Quantum Dimer Model on the Kagome Lattice: Solvable Dimer-Liquid and Ising Gauge Theory. *Phys. Rev. Lett.*, 89:137202, 2002.

[55] R. Moessner and S. L. Sondhi. Ising Models of Quantum Frustration. *Phys. Rev. B*, 63:224401, 2001.

[56] R. Moessner and S. L. Sondhi. Resonating Valence Bond Phase in the Triangular Lattice Quantum Dimer Model. *Phys. Rev. Lett.*, 86:1881, 2001.

[57] Tôru Moriya. Anisotropic superexchange interaction and weak ferromagnetism. *Phys. Rev.*, 120:91–98, Oct 1960.

[58] Y. Narumi, K. Katsumata, Z. Honda, J.-C. Domenge, P. Sindzingre, C. Lhuillier, Y. Shimaoka, T. C. Kobayashi, and K. Kindo. Observation of a Transient Magnetization Plateau in a Quantum Antiferromagnet on the Kagome Lattice . *Europhys. Lett.*, 65:705, 2004.

[59] Satoshi Nishimoto, Naokazu Shibata, and Chisa Hotta. Controlling frustrated liquids and solids with an applied field in a kagome Heisenberg antiferromagnet. *Nat Commun*, 4:2287, 2013.

[60] M.R Norman. Herbertsmithite and the search for the quantum spin liquid. *arXiv:1604.03048*, April 2016.

[61] Yoshihiko Okamoto, Masashi Tokunaga, Hiroyuki Yoshida, Akira Matsuo, Koichi Kindo, and Zenji Hiroi. Magnetization Plateaus in the Spin-1/2 Kagome Antiferromagnets: Volborthite and Vesignieite. *Phys. Rev. B*, 83:180407, 2011.

[62] A. M. Polyakov. Fermi-Bose Transmutations Induced by Gauge Fields. *Mod. Phys. Lett. A*, 3:325, 1988.

[63] Matthias Punk, Debanjan Chowdhury, and Subir Sachdev. Topological excitations and the dynamic structure factor of spin liquids on the kagome lattice. *Nat. Phys.*, 10:289, 2014.

[64] Ying Ran, Michael Hermele, Patrick A. Lee, and Xiao-Gang Wen. Projected wavefunction study of Spin-1/2 Heisenberg model on the Kagome lattice . *Phys. Rev. Lett.*, 98:117205, 2007.

[65] A. N. Redlich. Parity violation and gauge noninvariance of the effective gauge field action in three dimensions. *Phys. Rev. D*, 29:2366, 1984.

[66] Subir Sachdev. *Phys. Rev. B*, 45:12377, 1992.

[67] Subir Sachdev and N. Read. Large N Expansion for Frustrated and Doped Quantum Antiferromagnets. *Int. J. Mod. Phys. B*, 5:219, 1991.

[68] A. W. Sandvik. Evidence for Deconfined Quantum Criticality in a Two-Dimensional Heisenberg Model with Four-Spin Interactions. *Phys. Rev. Lett.*, 98:227202, 2007.

[69] Matthew P. Shores, Emily A. Nytko, Bart M. Bartlett, and Daniel G. Nocera. A structurally perfect s = 1/2 kagom antiferromagnet. *Journal of the American Chemical Society*, 127(39):13462–13463, 2005.

[70] Kai Sun, Krishna Kumar, and Eduardo Fradkin. A discretized Chern-Simons gauge theory on arbitrary graphs and the hydrodynamic theory of fractional Chern insulators, 2014. in preparation.

[71] D. J. Thouless, M. Kohmoto, M. P. Nightingale, and M. den Nijs. *Phys. Rev. Lett.*, 49:405, 1982.

[72] Chia-Hsiung Tze. Manifold-splitting regularization, self-linking, twisting, writhing numbers of space-time ribbons and Polyakov's proof of Fermi-Bose transmutations. *Int. J. Mod. Phys. A*, 3:1959–1979, 1988.

[73] Fa Wang and Ashvin Vishwanath. Spin-liquid states on the triangular and kagomé lattices: A projective-symmetry-group analysis of schwinger boson states. *Phys. Rev. B*, 74:174423, Nov 2006.

[74] Fa Wang and Ashvin Vishwanath. Spin-liquid states on the triangular and Kagomé lattices: A projective-symmetry-group analysis of Schwinger boson states. *Phys. Rev. B*, 74:174423, 2006.

[75] X.-G. Wen. Topological orders in rigid states. *Int. J. Mod. Phys. B*, 4:239, 1990.

[76] X. G. Wen. *Phys. Rev. B*, 44:2664, 1991.

[77] X. G. Wen. Topological Orders and Edge Excitations in Fractional Quantum Hall States. *Adv. Phys.*, 44:405, 1995.

[78] X. G. Wen. Topological Orders and Edge Excitations in Fractional Quantum Hall States. *Adv. Phys.*, 44:405, 1995.

[79] X. G. Wen, F. Wilczek, and A. Zee. Chiral spin states and superconductivity. *Phys. Rev. B*, 39:11413, 1989.

[80] X. G. Wen, F. Wilczek, and A. Zee. Chiral spin states and superconductivity. *Phys. Rev. B*, 39:11413, 1989.

[81] A. Wietek, A. Sterdyniak, and A. M. Läuchli. Nature of chiral spin liquids on the kagome lattice, 2015. unpublished.

[82] K. G. Wilson. Confinement of Quarks. *Phys. Rev. D*, 10:2445, 1974.

[83] Robin J. Wilson. *Introduction to Graph Theory*. Longman, 1998.

[84] Edward Witten. Quantum field theory and the jones polynomial. *Commun. Math. Phys.*, 121(3):351–399, 1989.

[85] Simeng Yan, David A. Huse, and Steven R. White. Spin Liquid Ground State of the S=1/2 Kagome Heisenberg Model. *Science*, 332:1173, 2011.

[86] Kun Yang, L. K. Warman, and S. M. Girvin. Possible Spin-Liquid States on the Triangular and Kagome Lattices. *Phys. Rev. Lett.*, 70:2641, 1993.

[87] Michael P. Zaletel and Ashvin Vishwanath. Constraints on topological order in mott insulators. *Phys. Rev. Lett.*, 114:077201, 2015.

[88] Yi Zhang, Tarun Grover, Ari Turner, Masaki Oshikawa, and Ashvin Vishwanath. Quasiparticle statistics and braiding from ground-state entanglement. *Phys. Rev. B*, 85:235151, Jun 2012.

[89] W. Zhu, S. S. Gong, and D. N. Sheng. Interaction-driven fractional quantum Hall state of hard-core bosons on kagome lattice at one-third filling, 2015.

[90] W. Zhu, D. N. Sheng, and F. D. M. Haldane. Minimal entangled states and modular matrix for fractional quantum hall effect in topological flat bands. *Phys. Rev. B*, 88:035122, Jul 2013.

Appendix A

Gauge symmetry

Here, we prove that Eq. (3.18) is the sufficient and necessary condition to maintain the gauge symmetry in our theory [Eq. (3.9)]

First, we substitute the magnetic flux in Eq. (3.9) by Eq. (3.10),

$$S = \frac{k}{2\pi}\int dt(A_v M_{v,f}\xi_{f,e}A_e - \frac{1}{2}A_{e_i}K_{e,e'}\dot{A}_{e'}) \tag{A.1}$$

Under the gauge transformation

$$A_v \rightarrow A_v - \partial_0\phi_v \tag{A.2}$$

$$A_e \rightarrow A_e - D_{v,e}\phi_v \tag{A.3}$$

the action Eq (A.1) is transfered to

$$\begin{aligned} S \rightarrow S + \frac{k}{2\pi}\int dt \left(-\dot{\phi}_v M_{v,f}\xi_{f,e}A_e + \frac{1}{2}D_{v,e}\phi_v K_{e,e}\dot{A}_{e'} + \frac{1}{2}A_e K_{e,e'}D_{v,e'}\dot{\phi}_v\right) \\ - \frac{k}{4\pi}\int dt \left(D_{v,e}\phi_v K_{e,e'}D_{v',e'}\dot{\phi}_{v'}\right) \end{aligned} \tag{A.4}$$

Here, the second term on the r.h.s. is linear in ϕ, while the last term is $O(\phi^2)$. In order to preserve the gauge symmetry, we need both these two terms to vanish, i.e.

$$\int dt \left(\dot{\phi}_v M_{v,f}\xi_{f,e}A_e - A_e K_{e,e'}D_{v,e'}\dot{\phi}_v\right) = 0 \tag{A.5}$$

$$\int dt \left(D_{v,e}\phi_v K_{e,e'}D_{v',e'}\dot{\phi}_{v'}\right) = 0 \tag{A.6}$$

In Eq. (A.5), we used the fact that

$$\int dt D_{v,e}\phi_v K_{e,e'}\dot{A}_{e'} = \int dt A_e K_{e,e'}D_{v,e'}\dot{\phi}_v \tag{A.7}$$

which can be proved via integrating by part and realizing that the K matrix is antisymmetric.

Equations (A.5) and (A.6) imply that

$$M_{v,f}\xi_{f,e} = K_{e,e'}D_{v,e'} \tag{A.8}$$

$$D_{v,e}K_{e,e'}D_{v',e'} = 0 \tag{A.9}$$

These two conditions are not independent to each other. In fact, Eq. (A.8) automatically implies Eq. (A.9). This can be realized by noticing that according to Eq. (A.8), we have

$$D_{v,e}K_{e,e'}D_{v',e'} = D_{v,e}M_{v',f}\xi_{f,e}. \tag{A.10}$$

The r.h.s. of this equation is zero because $D_{v,e}\xi_{f,e} = 0$, and thus Eq. (A.9) arises automatically.

Here, we explain why $D_{v,e}\xi_{f,e} = 0$. For any fixed f, $\xi_{f,e}$ represent an loop in the graph. If v is not a vertex on this loop, $D_{v,e}\xi_{f,e}$ must vanish, because $D_{v,e} = 0$. If the loop paths through v, there must be two edges along these loop that are connected to v, which we will call e_1 and e_2. It is easy to realize that according to the definition of ξ and D, $D_{v,e_1}\xi_{f,e_1} = -D_{v,e_2}\xi_{f,e_2}$ (here, we don't sum over repeated indices e_1 and e_2). Therefore, the contributions to $D_{v,e}\xi_{f,e}$ cancels out, i.e. $D_{v,e}\xi_{f,e} = 0$.

Appendix B

Edge space, circuit-subspace and the cut-subspace

In this section, we prove that the edge space is the direct sum of the circuit-subspace and the cut-subspace. Although this conclusion applies generically to planar and non-planar graphs, we will only discuss planar graphs here for simplicity, since the manuscript only consider planar ones.

We first prove that the circuit-subspace and the cut-subspace are orthogonal to each other. This can be verified easily by noticing that vectors from these two spaces (ξ_C and ξ_H) are orthogonal to each other (i.e. their dot product is zero)

$$\xi_{C,e}, \xi_{H,e} = 0. \tag{B.1}$$

In addition, we can prove that the dimension of the circuit-subspace plus the dimension of the cut-subspace coincides with the dimension of the edge space. Combined with the orthogonality proved above, this conclusion implies that the direct sum of the circuit-subspace and the cut-subspace is the edge space.

As mentioned in the main text, the basis of the circuit-subspace can be formed by all independent (contractible and non-contractible) cycles of a graph. For a planar graph with N_f faces defined on a manifold with genus g, there are $N_f - 1$ independent contractible cycles and $2g$ independent non-contractible cycles, i.e. $N_f - 1 + 2g$ independent loops in total. Therefore, the dimensionality of the of circuit-subspace is $N_f - 1 + 2g$.

For a planar graph G, cutsets corresponds to contractible cycles in the dual graph G^*. Because the dual graph has N_v faces, same as the number of vertices in the original graph, the number of independent cutsets (i.e. the number of independent contractible cycles in the dual graph) is $N_v - 1$.

If we add the dimensions of the cut subspace and the circuit subspace together, we get $N_f + N_v - 2 + 2g$, which coincides with the number of edges N_e, i.e. the dimension of the edge space. Here we utilized the fact that a closed orientable surface with genus g, the Euler characteristic is $2 - 2g$

$$N_v - N_e + N_f = 2 - 2g. \tag{B.2}$$

Because the circuit-subspace and the cut-subspace are two orthogonal subspaces of the edge space, and the total dimensions of these two subspaces match the dimensions of the edge space, we proved that the direct sum of these two subspace is the edge space.

Appendix C

The determinant of a block matrix

Here, we consider a $(N+M)\times(N+M)$ matrix

$$\mathcal{M} = \begin{pmatrix} 0 & C \\ D & B \end{pmatrix} \tag{C.1}$$

where each letter in the matrix represents a block matrix and the 0 (B) matrix has dimensions $N \times N$ ($M \times M$). We will prove below that the determinant of this matrix is zero when the size of the 0 block is larger than the B block (i.e. $N > M$).

First, we define a set of $N+M$ vectors $e_i = (0, 0, \ldots, 1, \ldots, 0)$, such that only the ith component of the vector e_i is nonzero, while $i = 1, 2, \ldots, N+M$. Here, these vectors span a $N+M$-dimensional linear space. This linear space is the direct sum of two subspace $V_1 \oplus V_2$, where V_1 is spanned by the vectors e_i with $1 \le i \le N$ and V_2 by those with $N+1 \le i \le N+M$, and it is easy to check that V_1 and V_2 are orthogonal to each other.

Because the upper-left block of the matrix only contains zeros, $e_i \mathcal{M} e_j = 0$ for $i \le N$ and $j \le N$. It implies that for any vector e_j with $j \le N$, the vector $\mathcal{M}e_j$ is orthogonal to any vectors in the subspace V_1. In other words, $\mathcal{M}e_j$ is a vector in the subspace V_2. For $j = 1, 2, \ldots, N$, $\mathcal{M}e_j$ generates N vectors in the space of V_2. If $N > M$, some of these N vectors must be linearly dependent, because the space V_2 can only have M independent vectors. Therefore, we can construct (at least) one zero vector using these N vectors $\mathcal{M}e_j$:

$$\sum_{j=1}^{N} a_j \mathcal{M} e_j = 0 \tag{C.2}$$

where a^j are N numbers. This implies immediately that the $\mathcal{M}$ matrix has (at least) one null vector

$v = \sum_{j=1}^{N} a_j e_j$

$$\mathcal{M}v = \sum_{j=1}^{N} \mathcal{M} a_j e_j = 0 \tag{C.3}$$

Having a zero eigenvalue implies that the determinant of $\mathcal{M}$ must be zero.

Appendix D

Polarization Tensor

D.1 Continuum Action

This appendix presents details on the computation of the polarization tensor and the continuum action. The polarization tensor is most easily computed in momentum space using the below expression

$$\Pi_{\mu\nu}(P_0,\vec{P}) = \int_{\omega,\vec{q}} iTr\left[S\left(P_0+\omega,\vec{P}+\vec{q}\right)j_\mu(\vec{P}+\vec{q})S(\omega,\vec{q})j_\nu(\vec{q})\right] \tag{D.1}$$

where $S(\omega,\vec{q})$ is the mean-field fermion propagator as shown in Eq.(4.20) and j_μ are the currents of the corresponding fluctuating components. The currents j_μ can be computed by taking derivatives of the action with respect to the corresponding fluctuating components i.e. $j_\mu = -\frac{\delta S}{\delta A_\mu}$. It is in general challenging to evaluate the integral shown in Eq.(D.1) due to the complicated form of the propagator in Eq.(4.20). To simplify the calculation, here we focus on the long wavelength limit by expanding Eq.(D.1) in powers of momenta P (up to quadratic order). This will allow us to compute the above integrals numerically for each of the fluctuating components in Eq.(4.24) and Eq.(4.25). As the slow components are considered to be more relevant, we make the following simplifications. Firstly, for the slowly fluctuating components, we only keep terms to quadratic order in momenta. Secondly, for the fast fluctuating components, we only keep the leading order terms i.e. the non-derivative terms. The continuum limit of the polarization tensor will then have a bunch of non-derivative (or mass) terms to the leading order. The remaining derivative terms (only for the slow components) takes the following form

$$\begin{aligned}
A_0(P)\Pi^{00}A_0(-P) =& u_{0xx0}A_0(P)P_x^2A_0(-P) + u_{0yy0}A_0(P)P_y^2A_0(-P)\\
A_0(P)\Pi^{0j}A_j(-P) =& u_{0xj}A_0(P)iP_xA_j(-P) + u_{0yj}A_0(P)iP_yA_j(-P)\\
&+ u_{0oxj}A_0(P)\Omega P_xA_j(-P) + u_{0oyj}A_0(P)\Omega P_yA_j(-P)\\
A_i(P)\Pi^{ij}A_j(-P) =& u_{ioj}A_i(P)i\Omega A_j(-P) + u_{iooj}A_i(P)\Omega^2A_j(-P)\\
&+ u_{ixxj}A_i(P)P_x^2A_j(-P) + u_{iyyj}A_i(P)P_y^2A_j(-P) + u_{ixyj}A_i(P)P_xP_yA_j(-P)
\end{aligned} \tag{D.2}$$

Also note that all the fields above correspond to the fluctuating components (we have dropped the δ label to make the notation less cumbersome). All the u coefficients here can be computed numerically using the integral formula shown above. This calculation can be further simplified by realizing that the transversality condition puts some constraints on these u coefficients. The action can then be written as

$$S_{\text{final}} = S_{00} + S_{0j} + S_{ij} + S^1_{CS} + S^2_{CS} + S_{int,0} + S_{int,2} \tag{D.3}$$

where the corresponding Lagrangian densities are given by

$$\mathscr{L}_{00} = \frac{1}{2}\, u_{00}^{fifi} \left[\left(A_0^{f1}\right)^2 + \left(A_0^{f2}\right)^2 \right] - \frac{1}{2} u_{00}^{f1f2} A_0^{f1} A_0^{f2} - \frac{1}{2} u_{0xx0} A_0 \partial_x^2 A_0 - \frac{1}{2} u_{0yy0} A_0 \partial_y^2 A_0 \tag{D.4}$$

$$\begin{aligned}
\mathscr{L}_{0j} =& \frac{1}{2} u_{0j}^{fif} \left\{ - \left[A_0^{f1} + A_0^{f2}\right] A_1^f - \left[A_0^{f1} + A_0^{f2}\right] A_2^f + \left[A_0^{f1} + A_0^{f2}\right] A_3^f \right\} \\
& - A_0 \partial_x \left[u_{0x1} A_1 + u_{0x2} A_2 + u_{0x3} A_3 \right] - A_0 \partial_y \left[u_{0y1} A_1 + u_{0y2} A_2 + u_{0y3} A_3 \right] \\
& + A_0 \partial_0 \partial_x \left\{ u_{0ox1} A_1 + u_{0ox2} A_2 + u_{0ox3} A_3 \right\} + A_0 \partial_0 \partial_y \left\{ u_{0oy1} A_1 + u_{0oy2} A_2 + u_{0oy3} A_3 \right\}
\end{aligned} \tag{D.5}$$

$$\begin{aligned}
\mathscr{L}_{ij} =& \frac{1}{2} u_{jk}^{ff} \left(A_1^f + A_2^f - A_3^f \right)^2 + \frac{1}{2} u_{jk} \left(A_1 + A_2 - A_3 \right)^2 \\
& + \left\{ u_{1o2} A_1 \partial_0 A_2 + u_{1o3} A_1 \partial_0 A_3 + u_{2o3} A_2 \partial_0 A_3 \right\} \\
& - \frac{1}{2} \left\{ u_{1oo1} A_1 \partial_0^2 A_1 + u_{2oo2} A_2 \partial_0^2 A_2 + u_{3oo3} A_3 \partial_0^2 A_3 + 2u_{1oo2} A_1 \partial_0^2 A_2 + 2u_{1oo3} A_1 \partial_0^2 A_3 + 2u_{2oo3} A_2 \partial_0^2 A_3 \right\} \\
& - \frac{1}{2} \left\{ u_{1xx1} A_1 \partial_x^2 A_1 + u_{2xx2} A_2 \partial_x^2 A_2 + u_{3xx3} A_3 \partial_x^2 A_3 + 2u_{1xx2} A_1 \partial_x^2 A_2 + 2u_{1xx3} A_1 \partial_x^2 A_3 + 2u_{2xx3} A_2 \partial_x^2 A_3 \right\} \\
& - \frac{1}{2} \left\{ u_{1yy1} A_1 \partial_y^2 A_1 + u_{2yy2} A_2 \partial_y^2 A_2 + u_{3yy3} A_3 \partial_y^2 A_3 + 2u_{1yy2} A_1 \partial_y^2 A_2 + 2u_{1yy3} A_1 \partial_y^2 A_3 + 2u_{2yy3} A_2 \partial_y^2 A_3 \right\} \\
& - \frac{1}{2} \big\{ u_{1xy1} A_1 \partial_x \partial_y A_1 + u_{2xy2} A_2 \partial_x \partial_y A_2 + u_{3xy3} A_3 \partial_x \partial_y A_3 \\
& \quad + 2u_{1xy2} A_1 \partial_x \partial_y A_2 + 2u_{1xy3} A_1 \partial_x \partial_y A_3 + 2u_{2xy3} A_2 \partial_x \partial_y A_3 \big\}
\end{aligned} \tag{D.6}$$

$$\begin{aligned}
\mathscr{L}^1_{CS} =& \frac{4}{\sqrt{3} a_0} \theta \left\{ \left(A_0^{f1} + A_0^{f2} \right) \left[A_1^f + A_2^f - A_3^f \right] + \left(-A_0^{f1} + A_0^{f2} \right) \left[A_1 + A_2 - A_3 \right] \right\} \\
& + \frac{1}{2\sqrt{3}} \theta A_0 \partial_x \left(A_1 + 5A_2 + 3A_3 \right) + \frac{1}{2} \theta A_0 \partial_y \left(-3A_1 + A_2 - A_3 \right) \\
\mathscr{L}^2_{CS} =& \frac{2}{\sqrt{3}} \theta \left\{ A_2 \left(2\partial_0 A_1 + \partial_0 A_3 \right) - A_1 \partial_0 A_3 \right\}
\end{aligned} \tag{D.7}$$

$$
\begin{aligned}
\mathscr{L}_{int,0} =& \frac{4}{\sqrt{3}a_0} J\theta^2\lambda \left\{ 3\left(A_1^f + A_2^f - A_3^f\right)^2 + (A_1 + A_2 - A_3)^2 \right\} \\
\mathscr{L}_{int,2} =& -J\lambda\theta^2 \frac{2}{\sqrt{3}} a_0 \big\{ \left(-\partial_1 A_1 - 2\partial_2 A_1 + 2\partial_1 A_2 + \partial_2 A_2 + \partial_1 A_3 - \partial_2 A_3\right)\left[-2\partial_2 A_1 + 2\partial_1 A_2\right] \\
& - \left(A_1 + A_2 - A_3\right)\partial_3^2 \left(A_1 + A_2 - A_3\right) \big\}
\end{aligned}
\tag{D.8}
$$

where a_0 is the lattice spacing and the continuum limit amounts to taking the limit $a_0 \to 0$. $\mathscr{L}_{00}$, $\mathscr{L}_{0j}$ and $\mathscr{L}_{ij}$ are obtained from the polarization tensor in Eq.(D.1) using the procedure outlined above. The $\mathscr{L}_{CS}$ and $\mathscr{L}_{\rm int}$ terms are obtained by expressing the Chern-Simons term in Eq.(2.5) and interaction term Eq.(4.1) in terms of the fluctuation components and taking the continuum limits respectively. The leading order mass terms are all proportional to $\frac{1}{a_0}$.

As noted in sections 4.3.1 and 4.3.2, the above action has excessive gauge fields. However, many of these fields are quadratic and massive and can be integrated out. More precisely, the above action has massive fields corresponding to A_0^{f1}, A_0^{f2}, $\widetilde{A}_3 \equiv A_1 + A_2 - A_3$ and $\widetilde{A}_3^f \equiv A_1^f + A_2^f - A_3^f$. Re-writing the quadratic part of the action that will be integrated out gives

$$
\begin{aligned}
\mathscr{L}_{quad} =& \frac{1}{2} A^T \cdot M \cdot A + A \cdot N \\
=& \frac{1}{2} A^T \cdot M \cdot A + \eta^T \cdot M \cdot A + \frac{1}{2}\eta^T \cdot M \cdot \eta + \eta^T \cdot N + A^T \cdot N
\end{aligned}
\tag{D.9}
$$

with

$$
A = \begin{pmatrix} A_0^{f1} \\ A_0^{f2} \\ \tilde{A}_3^f \\ \tilde{A}_3 \end{pmatrix}, N = \begin{pmatrix} 0 & 0 & 0 \\ 0 & 0 & 0 \\ 0 & 0 & 0 \\ \Delta_{30} & \Delta_{31} & \Delta_{32} \end{pmatrix} \begin{pmatrix} A_0 \\ A_1 \\ A_2 \end{pmatrix}
\tag{D.10}
$$

$$
M = \begin{pmatrix}
u_{00}^{fifi} & -\frac{1}{2}u_{00}^{f1f2} & \frac{1}{2}u_{0j}^{fif} - \frac{4}{\sqrt{3}a_0}\theta & \frac{4}{\sqrt{3}a_0}\theta \\
-\frac{1}{2}u_{00}^{f1f2} & u_{00}^{fifi} & \frac{1}{2}u_{0j}^{fif} - \frac{4}{\sqrt{3}a_0}\theta & -\frac{4}{\sqrt{3}a_0}\theta \\
\frac{1}{2}u_{0j}^{fif} - \frac{4}{\sqrt{3}a_0}\theta & \frac{1}{2}u_{0j}^{fif} - \frac{4}{\sqrt{3}a_0}\theta & u_{jk}^{ff} + \frac{24}{\sqrt{3}a_0}\theta^2\lambda & 0 \\
\frac{4}{\sqrt{3}a_0}\theta & -\frac{4}{\sqrt{3}a_0}\theta & 0 & u_{jk} + \frac{8}{\sqrt{3}a_0}\theta^2\lambda + 2\Delta^2
\end{pmatrix}
\tag{D.11}
$$

The Δ's correspond to derivative terms and are shown below.

$$\begin{aligned}
\Delta^2 =&\lambda\theta^2\frac{2}{\sqrt{3}}a_0\partial_3^2 - \frac{1}{2}\left\{u_{3oo3}\partial_0^2 + u_{3xx3}\partial_x^2 + u_{3yy3}\partial_y^2 + u_{3xy3}\partial_x\partial_y\right\}\\
\Delta_{30} =&-\frac{3}{2\sqrt{3}}\theta\partial_x + \frac{1}{2}\theta\partial_y + u_{0x3}\partial_x + u_{0y3}\partial_y + u_{0ox3}\partial_0\partial_x + u_{0oy3}\partial_0\partial_y\\
\Delta_{31} =&-u_{1o3}\partial_0 + \frac{2}{\sqrt{3}}\theta\partial_0 - \lambda\theta^2\frac{4}{\sqrt{3}}a_0\partial_1\partial_2 A_1 + \lambda\theta^2\frac{4}{\sqrt{3}}a_0\partial_2^2\\
&-\left\{u_{3oo3}\partial_0^2 + u_{1oo3}\partial_0^2 + u_{3xx3}\partial_x^2 + u_{1xx3}\partial_x^2 + u_{3yy3}\partial_y^2 + u_{1yy3}\partial_y^2 + u_{3xy3}\partial_x\partial_y + u_{1xy3}\partial_x\partial_y\right\}\\
\Delta_{32} =&-u_{2o3}\partial_0 - \frac{2}{\sqrt{3}}\theta\partial_0 + \lambda\theta^2\frac{4}{\sqrt{3}}a_0\partial_1^2 - \lambda\theta^2\frac{4}{\sqrt{3}}a_0\partial_1\partial_2\\
&-\left\{u_{3oo3}\partial_0^2 + u_{2oo3}\partial_0^2 + u_{3xx3}\partial_x^2 + u_{2xx3}\partial_x^2 + u_{3yy3}\partial_y^2 + u_{2yy3}\partial_y^2 + u_{3xy3}\partial_x\partial_y + u_{2xy3}\partial_x\partial_y\right\}
\end{aligned} \tag{D.12}$$

The sign of the masses have been verified numerically for different values of λ and we have ensured that they have the correct sign in order to safely integrate them out. After integrating out these fields the remaining terms are given by

$$\mathscr{L}_{\text{eff}} = -\frac{1}{2}N^T\cdot M^{-1}\cdot N \tag{D.13}$$

To quadratic order, we find that

$$\begin{aligned}
\mathscr{L}_{CS,eff} =&\frac{1}{2}\left(\theta+\theta_F\right)\epsilon_{\mu\nu\lambda}A_\mu\partial_\nu A_\lambda\\
\mathscr{L}_{EM} =&\frac{1}{2}\pi_{xx}\left[-A_0\partial_x^2A_0 + 2A_0\partial_0\partial_x A_x - A_x\partial_0^2A_x\right] + \frac{1}{2}\pi_{yy}\left[-A_0\partial_y^2A_0 + 2A_0\partial_0\partial_y A_y - A_y\partial_0^2A_y\right]\\
&+\frac{1}{2}\pi_{xy}\left[-A_y\partial_x^2A_y + 2A_x\partial_x\partial_y A_y - A_x\partial_y^2A_x\right] - \lambda\theta^2\frac{3\sqrt{3}}{16}a_0\left(\partial_x A_y - \partial_y A_x\right)^2
\end{aligned} \tag{D.14}$$

with

$$\begin{aligned}
\theta_F =&-\frac{\sqrt{3}}{8}\left(u_{1o2} + u_{1o3} - u_{2o3}\right)\\
\pi_{xx} =&\frac{1}{4}u_{1oo1} + \frac{1}{2}u_{1oo3} - \frac{1}{16}u_{2oo2} - \frac{1}{8}u_{2oo3} + \frac{3}{16}u_{3oo3}\\
\pi_{yy} =&\frac{3}{16}\left(u_{3oo3} + 2u_{2oo3} + u_{2oo2}\right)\\
\pi_{xy} =&\frac{3}{16}\left(u_{2xx2} + 2u_{2xx3} + u_{3xx3}\right)
\end{aligned} \tag{D.15}$$

We have also re-expressed the A_1 and A_2 fields along the x and y directions to give A_x and A_y. Once again, all the u coefficients are computed using the equation for the polarization tensor in Eq.(D.1). The final form is written in terms of E and B fields as

$$\begin{aligned}
\mathscr{L}_{CS,eff} =&\frac{1}{2}\left(\theta+\theta_F\right)\epsilon_{\mu\nu\lambda}A_\mu\partial_\nu A_\lambda\\
\mathscr{L}_{EM} =&\frac{1}{2}\epsilon\boldsymbol{E}^2 - \frac{1}{2}\chi B^2
\end{aligned} \tag{D.16}$$

where $\epsilon = \pi_{xx} = \pi_{yy}$, $\chi = g - \pi_{xy}$ and $g = \lambda\theta^2 \frac{3\sqrt{3}}{8} a_0$ corresponding the interaction strength. Eq.(D.16) is the same result that was expressed in Section4.3.2.

The numerically computed values are listed in the below table for a few different values of λ.

λ	$\theta_F + \theta$	$\epsilon = \pi_{xx} = \pi_{yy}$	$\chi = g - \pi_{xy}$	π_{xy}
0	$\frac{1}{2\pi}(2)$	$\frac{a_0}{2\pi}1.33312$	$\frac{a_0}{2\pi}0.242483$	$-\frac{a_0}{2\pi}0.242466$
0.25	$\frac{1}{2\pi}(2)$	$\frac{a_0}{2\pi}1.11182$	$\frac{a_0}{2\pi}0.220687$	$-\frac{a_0}{2\pi}0.216574$
0.5	$\frac{1}{2\pi}(2)$	$\frac{a_0}{2\pi}1.82261$	$\frac{a_0}{2\pi}0.285403$	$-\frac{a_0}{2\pi}0.277177$
0.6	$\frac{1}{2\pi}(2)$	$\frac{a_0}{2\pi}43.0296$	$\frac{a_0}{2\pi}4.28244$	$-\frac{a_0}{2\pi}4.27257$
0.75	$\frac{1}{2\pi}(1)$	$\frac{a_0}{2\pi}0.821131$	$\frac{a_0}{2\pi}0.0550438$	$-\frac{a_0}{2\pi}0.0427044$
1	$\frac{1}{2\pi}(1)$	$\frac{a_0}{2\pi}0.192793$	$\frac{a_0}{2\pi}0.0254114$	$-\frac{a_0}{2\pi}0.00895888$

(D.17)

Appendix E

Spin-spin correlations

E.1 S^zS^z correlations

The fluctuating components of the $< S^zS^z >$ correlation can be expressed in terms of the magnetic field from the Jordan-Wigner transformation as shown below. This expectation can then be computed by introducing the usual source term j_μ coupled to a Chern-Simons term as follows

$$\begin{aligned} < S^z(x)S^z(y) > &\approx < B(x)B(y) > \\ &\approx -\theta^2 \frac{1}{Z}\frac{\delta}{\delta j_0(x)}\frac{\delta}{\delta_0 j(y)}\int DA_\mu e^{i\frac{1}{2}\int d^3xd^3yA_\mu(x)G^{-1,\mu\nu}(x,y)A_\lambda(y)+i\int d^3xj_\mu(x)\epsilon^{\mu\nu\lambda}\partial_\nu A_\lambda(x)} \end{aligned} \tag{E.1}$$

where $G^{\mu\nu}$ is the continuum Green's function of the Lagrangian in Eq.(D.16) and Z is the partition function.

The A_μ fields can now be integrated out using the standard procedure of shifting the fields $A_\mu \to a_\mu + \eta_\mu$ and then requiring that the terms linear in η_μ cancel. This gives the condition

$$a_\delta(x) = -\int_{x'} G_{\delta\mu}(x,x')\epsilon^{\mu\nu\lambda}\partial'_\nu j_\lambda(x') \tag{E.2}$$

Substituting the above expression back into Eq.(E.1) gives

$$\begin{aligned} < S^z(x)S^z(y) > &\approx -\theta^2 \frac{\delta}{\delta j_0(x)}\frac{\delta}{\delta_0 j(y)} e^{i\int_{x,x'}\left\{-\frac{1}{2}j_\mu(x)\left[\epsilon^{\mu\nu\lambda}\epsilon^{\delta\rho\epsilon}\partial_\nu\partial'_\rho G_{\lambda\epsilon}(x,x')\right]j_\delta(x')\right\}} \\ &= i\theta^2\epsilon^{0\nu\lambda}\epsilon^{0\rho\epsilon}\partial_\nu\partial^y_\rho G_{\lambda\epsilon}(x,y) \end{aligned} \tag{E.3}$$

The Green's function can be computed in the momentum space. Hence, the Fourier transform of the S^zS^z spin correlation $f^{zz}(p)$ can now be expressed as

$$f^{zz}(p) = \theta^2\left(p_1^2G_{22}(p) - p_1p_2G_{12}(p) - p_1p_2G_{21}(p) + p_2^2G_{11}(p)\right) \tag{E.4}$$

The propagator can be computed by introducing a gauge fixing term $\frac{\alpha}{2}(\partial^\mu A_\mu)^2$

$$G^{-1}_{\mu\nu}(p) = \begin{pmatrix} \alpha\omega^2 + p_1^2\epsilon + p_2^2\epsilon & p_1\omega(\epsilon-\alpha) + i\bar{\theta}p_2 & p_2\omega(\epsilon-\alpha) - i\bar{\theta}p_1 \\ p_1\omega(\epsilon-\alpha) - i\bar{\theta}p_2 & \alpha p_1^2 - p_2^2\chi + \omega^2\epsilon & +p_1p_2(\chi+\alpha) - i\bar{\theta}\omega \\ p_2\omega(\epsilon-\alpha) + i\bar{\theta}p_1 & +p_1p_2(\chi+\alpha) + i\bar{\theta}\omega & \alpha p_2^2 - p_1^2\chi + \omega^2\epsilon \end{pmatrix} \tag{E.5}$$

where $\bar{\theta} = \theta + \theta_F$. The limit $\alpha \to \infty$ corresponds to the Lorentz gauge ($\partial^\mu A_\mu = 0$). In this gauge the above correlation yields

$$f^{zz}(p) \approx \theta^2 \frac{\epsilon\vec{p}^2}{\epsilon^2\omega^2 - \epsilon\chi\vec{p}^2 - (\theta+\theta_F)^2} \tag{E.6}$$

where $\vec{p}^2 = p_1^2 + p_2^2$.

Note that in the XY regime $\theta + \theta_F = \frac{1}{\pi}$ for the case of $\frac{1}{3}$ filling on the Kagome lattice making the collective modes massive.

$$f^{zz}(p) \approx \theta^2 \frac{\epsilon\vec{p}^2}{\epsilon^2\omega^2 - \epsilon\chi\vec{p}^2 - (\frac{1}{\pi})^2} \tag{E.7}$$

If the same calculation were performed on the square lattice (which is unfrustrated), the two terms would cancel ($\theta + \theta_F = 0$) as observed in the main text and the collective modes are massless corresponding to Goldstone modes in the XY regime.

E.2 XY correlations

Using the Jordan-Wigner transformation, the spin-spin correlation function $< S^+(x)S^-(y) >$ can be written as

$$\begin{aligned} S^{XY}_\Gamma(x,y) &= < S^+(x)S^-(y) > \\ &\approx \left\langle \psi^\dagger(x) e^{i\int_{\Gamma(x,y)} A_\mu dx^\mu} \psi(y) \right\rangle \\ &= \left\langle G_F(x,y;A_\mu) e^{i\int_{\Gamma(x,y)} A_\mu dx^\mu} \right\rangle_{A_\mu} \end{aligned} \tag{E.8}$$

where $G_F(x,y;A_\mu)$ is the fermion Green function in the presence of the statistical gauge field A_μ and is obtained by integrating out the fermionic degrees of freedom. The average in the last step is over the statistical gauge fields A_μ. Computing this expectation is involving due to the presence of the non-local string along the path $\Gamma(x,y)$ that starts from x and ends at y. To simplify the above expression, the fermionic propagator can be expressed in terms of a Feynman path integral as a sum over histories of the particles as follows

$$G_F(x,y;A_\mu) = -i\int_0^\infty dT \int D\vec{z}(t) e^{iS[\vec{z}(t)]} \tag{E.9}$$

where the action S is the action for non-relativistic particles coupled to the statistical gauge field

$$S = \int_0^T dt \left\{ \frac{1}{2} \left(\frac{d\vec{z}}{dt} \right)^2 + \frac{dz^\mu}{dt} A_\mu(\vec{z}) \right\} \tag{E.10}$$

subject to the boundary conditions for a particle travelling from y to x

$$lim_{t\to 0}\vec{z}(t) = \vec{y} \qquad\qquad lim_{t\to T}\vec{z}(t) = \vec{x} \tag{E.11}$$

Note that the second term in the above action corresponds to another Wilson line but now travelling from point y to point x. This combined with the Wilson line in Eq.(E.8) now creates a closed loop which we will call γ. For a problem with an energy gap and in the long-distance limit, the dominant trajectories are close to the classical trajectories. In this approximation the average over the different trajectories $\vec{z}(t)$ can be pulled outside of the integral for averaging over the statistical gauge fields. Hence, Eq.(E.8) can now be written as

$$\begin{aligned} S_\Gamma^{XY}(x,y) &= \int_0^\infty dT \int D\vec{z}(t) e^{i\int_0^T dt \frac{1}{2}\left(\frac{d\vec{z}}{dt}\right)^2} \left\langle e^{i\int_\gamma A^\mu dz_\mu} \right\rangle_{A_\mu} \\ &\approx \sum_\gamma (Amp)_\gamma \left\langle e^{i\int_\gamma A^\mu dz_\mu} \right\rangle_{A_\mu} \end{aligned} \tag{E.12}$$

where $(Amp)_\gamma$ is the amplitude associated with a path γ and the set of closed curves $\{\gamma\}$ are the oriented sum of paths Γ and the histories of the particle.

Now, the computation of the Wilson loop expectation value can be performed by introducing a source term J_μ as follows

$$\left\langle e^{i\int_\gamma A^\mu dz_\mu} \right\rangle_{A_\mu} = \left\langle e^{i\int d^3z J_\mu(z) A^\mu(z)} \right\rangle_{A_\mu} \tag{E.13}$$

where

$$J_\mu(z) = \begin{cases} S_\mu(z) & \text{if } z\epsilon\gamma \\ 0 & \text{otherwise} \end{cases} \tag{E.14}$$

where $S_\mu(z)$ is a unit vector tangent to the path γ at z. In this form the above expectation can be written as

$$\left\langle e^{i\int_\gamma A^\mu dz_\mu} \right\rangle_{A_\mu} = e^{-\frac{i}{2}\int_{x,y} J_\mu(x) G^{\mu\nu}(x,y) J_\nu(y)} \tag{E.15}$$

where $G^{\mu\nu}$ is the Green's function in the continuum for the statistical gauge fields shown above in Eq.(E.5). The exponent in the above integral has two contributions, one from the Maxwell like terms (I_1) and the

other from the Chern-Simons like terms I_2. First, the I_1 term can be simplified to give

$$I_1 = -\frac{\epsilon}{2}\int_{x,y} J_\mu(x) G_0(x,y;\bar{\theta}^2) J^\mu(y) \tag{E.16}$$

where the propagator $G_0(x,y;\theta^2)$ can be approximated in the long-distance limit as follows

$$G_0(x,y;\bar{\theta}^2) = \langle x| \frac{1}{\epsilon^2\partial^2 + \epsilon(\chi-\epsilon)\partial_i^2 - \bar{\theta}^2} |y\rangle \approx -\frac{1}{\bar{\theta}^2}\delta(x-y) \tag{E.17}$$

Note here that we are assuming that the above propagator is massive (i.e $\bar{\theta} \neq 0$) as in the case of $\frac{1}{3}$ filling in the XY limit of the Kagome lattice. This argument would clearly fail at other fillings or for instance in the case of the square lattice when $\bar{\theta} = 0$ changing the physics all together.

Hence, the integral I_1 can be approximated as

$$I_1 \approx \frac{\epsilon}{2\bar{\theta}^2}\int_x J_\mu(x) J^\mu(x) = -\frac{\epsilon}{2(\theta+\theta_F)^2} L(\gamma) \tag{E.18}$$

where $L(\gamma)$ is the length of the path γ. The second integral due to the Chern-Simons term approximates to give (again in the long-distance limit)

$$\begin{aligned} I_2 =& \frac{i\bar{\theta}}{2}\int_{x,y} J_\mu(x) \langle x| \frac{1}{\partial^2\left(\epsilon^2\partial^2 + \epsilon(\chi-\epsilon)\partial_i^2 - \bar{\theta}^2\right)} \epsilon^{\mu\nu\lambda}\partial_\lambda |y\rangle J_\nu(y) \\ \approx& \frac{i}{2\bar{\theta}}\int_{x,y} J_\mu(x)\epsilon^{\mu\nu\lambda} \langle x| \frac{1}{\partial^2} |y\rangle \partial_\nu J_\lambda(y) \\ =& \frac{i}{2\bar{\theta}}\int_{x,y} J_\mu(x)\epsilon^{\mu\nu\lambda} G_0(x,y;0)\partial_\nu J_\lambda(y) \end{aligned} \tag{E.19}$$

The current $J_\mu(x)$ can be regarded as an electric current. With this interpretation the current can be related to a magnetic field $B_\mu(x)$ as follows

$$B_\mu(x) = \int_y G_0(x,y;0)\epsilon_{\mu\nu\lambda}\partial^\nu J^\lambda(y) \tag{E.20}$$

Now the second integral I_2 can be written in terms of a magnetic field as

$$I_2 \approx \frac{i}{2\bar{\theta}}\frac{\Phi_\gamma}{\phi_0} = \frac{i}{2}\Phi_\gamma \tag{E.21}$$

where again at the semi-classical level we have approximated the field by the average flux Φ_γ over the path γ. This makes the above integral take the form of an Aharonov-Bohm phase over the path γ. In the last

step we have used the fact that $\bar{\theta} = \theta + \theta_F = \frac{1}{\pi}$ and $\phi_0 = 2\pi$ (in units of $h = e = c = 1$). Hence, the correlation can be approximated as

$$S_{\Gamma}^{XY}(x, y) \approx \sum_{\gamma} (Amp)_{\gamma} e^{I_1 + I_2} \tag{E.22}$$

where I_1 decays exponentially as the length of the path $L(\gamma)$ increases and I_2 is an Aharonov-Bohm phase associated with the path γ. The Aharonov-Bohm term in the above expression would depend closely on the two points x and y and the area of the path traversed by path γ. In the main text we have considered two possible situations, one where the area of the path γ is zero and doesn't lead to any Aharonov-Bohm phase and the other where there are several different Aharonov-Bohm phases that can arise.

Appendix F

Technical details

In this appendix, I present some technical information regarding the exact diagonalization for the $m = \frac{2}{3}$ magnetization plateau. The details of dimensions for different sized clusters used in the ED are shown in Table F.1. Due to the higher value of magnetization (which corresponds to a higher S_z sector), the relative dimensions for larger clusters are quite manageable.

Spin models obey S_z symmetry and as all the cluster we consider have periodic boundary conditions in both directions, we can implement translational symmetry as well which reduced the size of the Hilbert space by a factor of $\frac{N}{3}$ where N is the number of total sites on the Kagome lattice. Note that in order to observe the $m = \frac{2}{3}$, we need to use clusters sizes that are a multiple of six i.e. $N = 6n$ where n is a positive integer. Hence, the eigenstates computed from ED will be characterized by both S_z and momentum (k_x, k_y) quantum numbers. In the special case of the 48 site cluster rotational symmetry will also play the role of an additional quantum number.

In order to perform the exact diagonalization, we utilized ARPACK software. [47]

Cluster	S_z	No. of states (S_z sector)	No. of States ($\vec{k}$ sector)
30	10	$\binom{30}{25} = 142,506$	$\approx$ 14,251
36	12	$\binom{36}{30} = 1,947,792$	$\approx$ 162,316
42	14	$\binom{42}{35} = 26,978,328$	$\approx$ 1,927,023
48	16	$\binom{48}{40} = 377,348,994$	$\approx$ 23,584,312

Table F.1: ED details for the $m = \frac{2}{3}$ plateau for different sized clusters. The No. of states (S_z sector) shows the dimension of the Hilbert space after S_z symmetry has been accounted for and No. of states ($\vec{k}$ sector) shows the further reduction in the Hilbert space once translations symmetry has been implemented.